

APPLIED SCIENCE ASSOCIATES, INC.

105 EAST CHATHAM STREET
POST OFFICE BOX 949
APEX, NORTH CAROLINA 27502
PHONE (919) 362-7256

NASA CR-137462

**Engineering Studies Related to the GEOS-C
Radar Altimeter**

by

L. S. Miller

G. S. Brown

Final Report for Task D

May, 1974

Prepared under
NASA Contract No. NAS6-2307

for

National Aeronautics and Space Administration
Wallops Flight Center
Wallops Island, Virginia 23337

(NASA-CR-137462) ENGINEERING STUDIES
RELATED TO THE GEOS-C RADAR ALTIMETER
Final Report (Applied Science Associates,
Inc., Apex, N.C.) 95 p HC \$7.75

CSC 14B 63/14

Unclas
46147

N74-30899

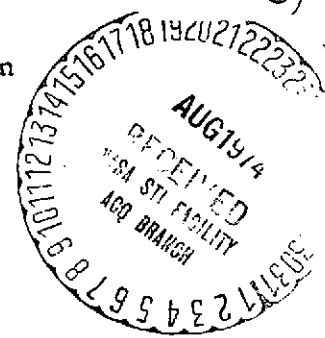


TABLE OF CONTENTS

	Page
1.0 INTRODUCTION	1
2.0 ANALYSIS OF GEOS-C WAVEHEIGHT RESOLUTION	2
2.1 Summary of Results and Recommendations	2
2.2 Analysis of Tracking Time-Jitter Effects and Waveheight Resolution	5
2.2.1 Computation of the Mean With Jitter Present	12
2.2.2 Computation of the Variance With Jitter Present	15
2.2.3 Comments	18
2.2.4 Sea State Resolution	19
References	24
3.0 SPATIAL FILTER EFFECT AND OPTIMAL FILTER FOR GEOID DATA PROCESSING	26
3.1 Geoidal Data Processing Results	26
3.2 Spatial Filter Effect	33
3.2.1 Background Discussion	33
3.2.2 Determination of the Mean Return Waveform	34
3.2.3 Determination of the Split-Gate Tracker Response	44
3.2.4 Results for the GEOS-C Intensive Mode of Operation	50
References	54
Appendix A	56
Appendix B	59
4.0 ALTITUDE-WAVEFORM BIAS EFFECTS AND POINTING ANGLE ESTIMATION ACCURACY	64
4.1 Waveform Bias Effects on the Altitude	64
4.1.1 Analysis	67
4.1.2 Results	74
4.1.3 Conclusions	77
4.2 Pointing Angle Estimation Using the Attitude/Specular Gate	88
References	92

1.0 INTRODUCTION

This is the final engineering report on Task D of NASA Contract No. NAS6-2307. This task comprised a study of experiment requirements, of technical characteristics, and of the GEOS-C radar altimeter related analyses. In addition to the work reported herein, a study of engineering test data requirements was also conducted; results of this activity were documented in a report distributed in December, 1973.

Chapter II of this report contains statistical analyses related to determination of wave height resolution achievable as a function of system characteristics and averaging period. An equally important topic of this chapter is the desirability of using computer procedures to compensate for altitude tracker time-jitter.

Chapter III examines data processing considerations for the GEOS-C system. An extensive analysis of the spatial filter effect is given and results of a computation of geoidal power spectral density, based on Skylab altimeter data, is displayed and interpreted in terms of projected GEOS-C random errors. This information is then used in deriving minimum-mean-square filter procedures for both geoid undulation and slope data.

Chapter IV examines the characteristics of mean received waveforms as a function of off-nadir angle. This information is then used to obtain tracker bias as a function of sea state and pointing angle. The angle estimation process proposed by the GEOS-C hardware contractor (General Electric) is also investigated from a standpoint of achievable angular resolution.

2.0 ANALYSIS OF GEOS-C WAVEHEIGHT RESOLUTION

2.1 Summary of Results and Recommendations

The main body of this section is devoted to an analysis of waveheight resolution, in significant waveheight units, achievable with the GEOS-C altimeter, and the effect of uncorrected altitude tracker time-jitter on resolution. The final results of this analysis are shown in graphic form in Figures 2.1 and 2.2. Results for pulse lengths of 10 and 12.5 ns are given because currently available GEOS-C test data shows the pre-detection pulse width to be ~ 13 ns at the 6 dB points. Since a square-law detector is used, this implies a post-detection pulse width of 13 ns at the 12 dB points and we estimate that the video filter would increase this pulse width to ~ 10 ns at the 3 dB level. Figure 2.1 shows that for the 10 ns pulse length with expected time jitter (~3 ns), 80 percent of the observations will be within ± 25 percent of the correct value for significant wave heights ($H_{1/3}$) of ≥ 3 meters. Below this $H_{1/3}$ value the resolution degrades rapidly. For a time-jitter of 6 ns, the corresponding $H_{1/3}$ value is ~ 3.5 meters. To allow a comparison with other results, this figure also shows a "one-sigma" confidence level result; here the 25% resolution value intersects the curve at $H_{1/3} = 2.4$ meters. We do not recommend use of this bound.

Figure 2.2 shows similar results for a 12.5 ns pulse width. Here the 6 ns jitter case ± 25 % resolution point is seen to occur at ~ 4.25 meters. For an rms tracking jitter of 12 ns (which is considered to be in the category of substandard data) the ± 25 % resolution point is ~ 5.15 meters. Note that if the 12 ns rms jitter is assumed to be correctable (at $H_{1/3} \approx 3.6$ meters), tracking jitter correction is equivalent to an extension of the averaging period by a factor of 2.5 (waveheight resolution is proportional to the square root of the averaging period).

Both Figures 2.1 and 2.2 are based on an averaging period of 20 seconds. This value was used since we feel it represents an approximate upper bound on averaging period, unless a priori information is available regarding ocean surface homogeneity. Since high seas are of quite low probability on a global scale, it would be highly desirable to be able to collect experimental waveheight data as it exists, in the planned GEOS-C calibration area. For an experiment that requires high seas (e.g., the North Atlantic in the winter months), the acquisition of aircraft sea-truth data is a formidable task.

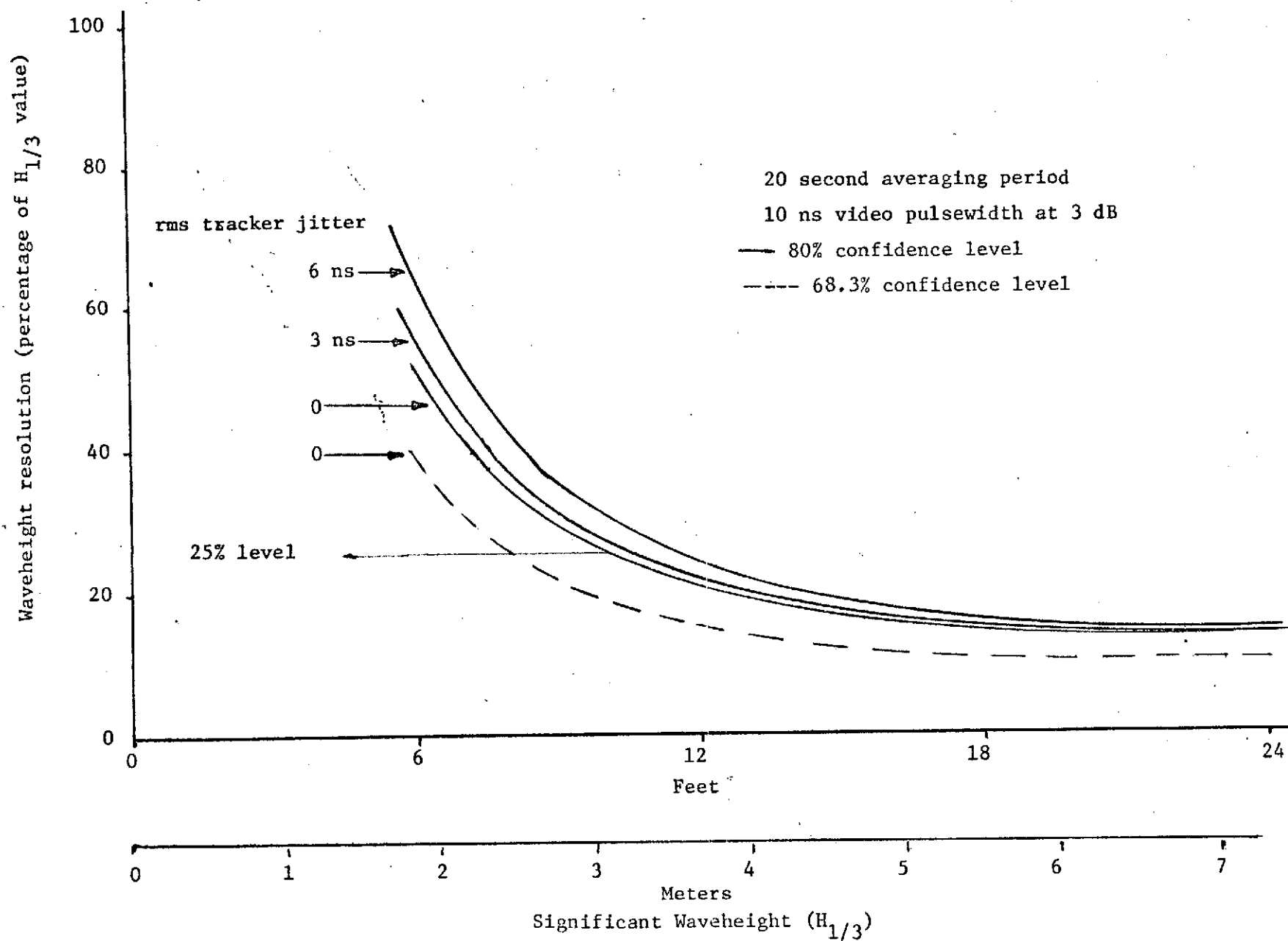


Fig. 2.1 Computed GEOS-C Waveheight Resolution

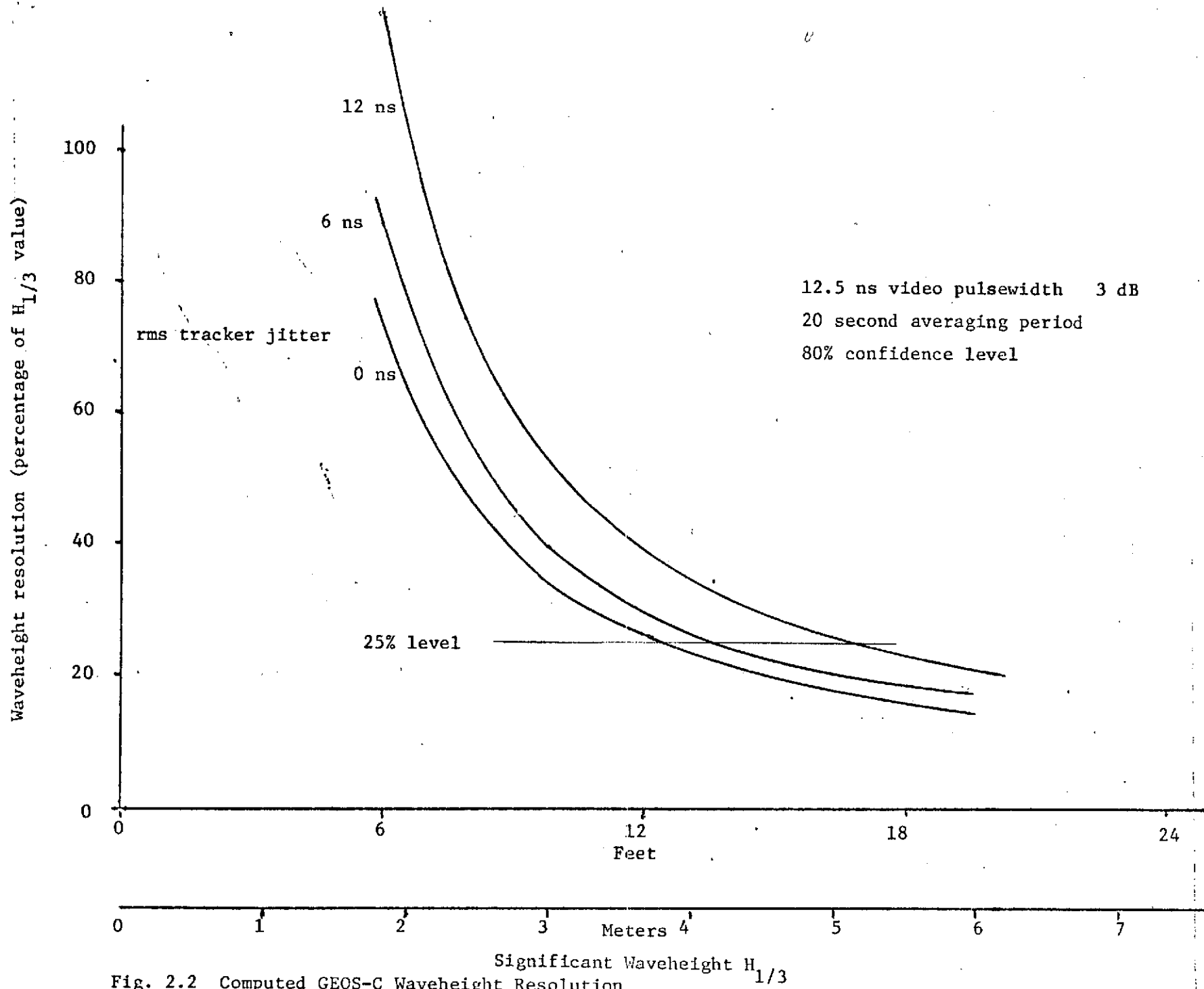


Fig. 2.2 Computed GEOS-C Waveheight Resolution

To provide some insight into the problem of extending the data averaging period, two randomly selected sea-truth charts are shown in Figures 2.3 and 2.4. These were supplied by NOAA during the Skylab program's SL-2 and SL-3 missions. Figure 2.3 shows a 3 meter $H_{1/3}$ isocontour crossing for pass 9 and 2 meter isocontour crossings for pass 8 - for the wind-driven (non-swell) data shown. The scaled time periods for the ground track to traverse these areas are 10 and 18.6 seconds. In Figure 2.4 the subsatellite path crosses two 1-meter contours in approximately 20 seconds.

Based on the above discussed results, the ~3 ns rms tracking jitter level anticipated for the GEOS-C altimeter is seen to produce a relatively small degradation in wave height resolution. Therefore, under assumed nominal altimeter performance we do not recommend corrections in the waveform averaging process to compensate for the altitude tracker time-history. If, after launch, for some reason the altitude data quality should seriously degrade (>12 ns rms noise) the question of time-jitter correction should be re-examined. The need for corrections in the waveform averaging process for deterministic orbital effects is an unexamined question. For an assumed altitude rate of change of 50 meters/second, due to orbital eccentricity, and a tracking loop correlation interval of ~50 milliseconds, the altitude change during the correlation period is 16 ns. Hardware test data should be available in the near future to permit an assessment of the effect of such altitude rates on tracker variance.

2.2 Analysis of Tracking Time-Jitter Effects and Waveheight Resolution*

Our main purpose in this section is to analyze the effect of altitude tracker-induced time-jitter in the sample-and-hold (S & H) data on waveform averaging and waveheight resolution. Because of the small tracker (and thus S & H gate position) standard deviation (~3 ns) relative to the "flat sea" rise time, we desire to examine the effect of neglecting tracker time-jitter in the reconstruction process. Figure 2.5 shows presently planned waveform data processing procedures and the overriding importance of this effect.

In the following analysis we examine the uncertainty in the estimate of the received waveform as a function of averaging period. Since a single received waveshape is an ensemble member of a random process, the greater the number of waveforms averaged the lower the uncertainty in mean value and thus

*A major part of this section was contributed by A. C. Nelson.

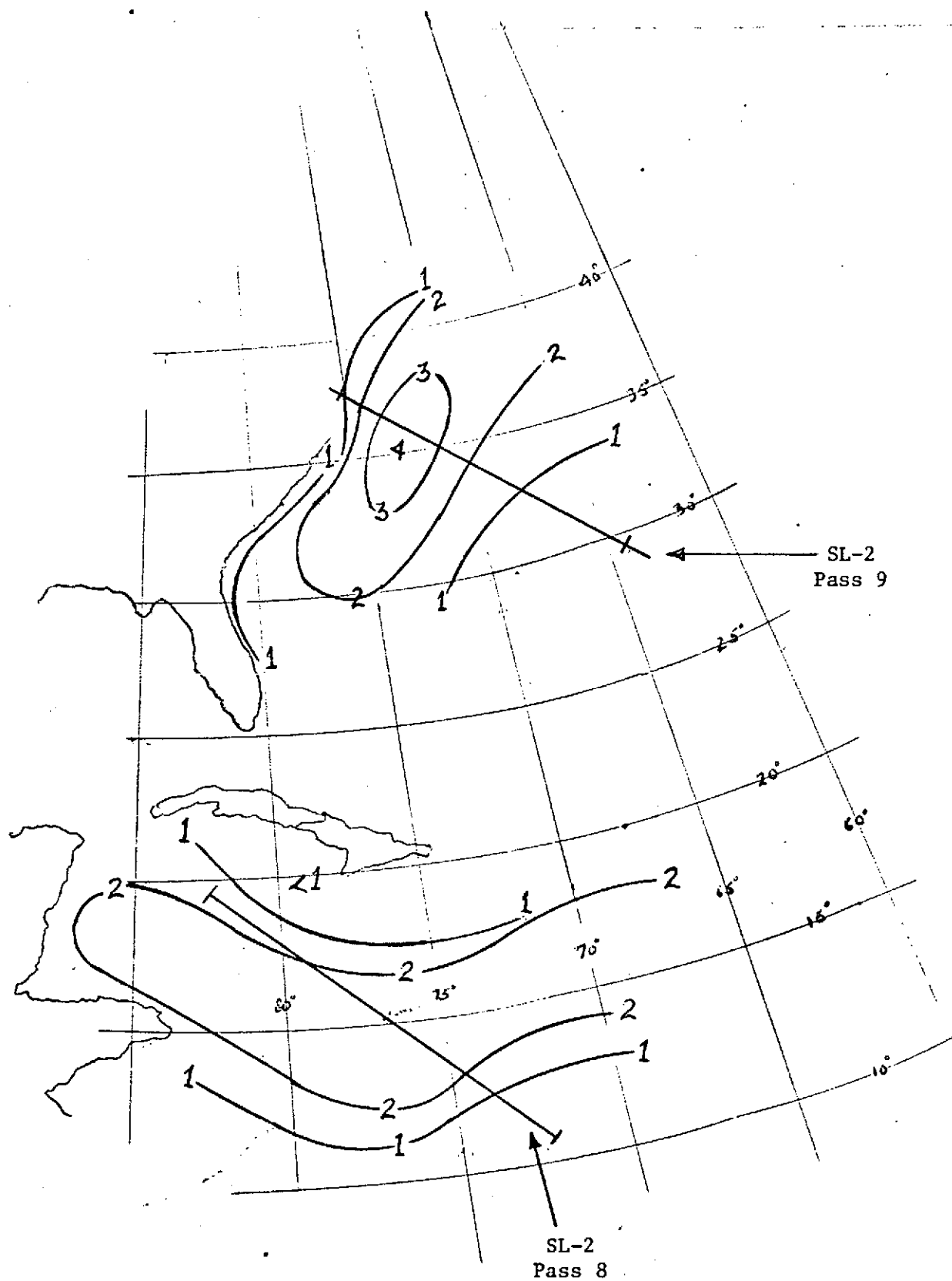


Fig. 2.3 Isolines of Significant Waveheight, June 12 and 13 1973.

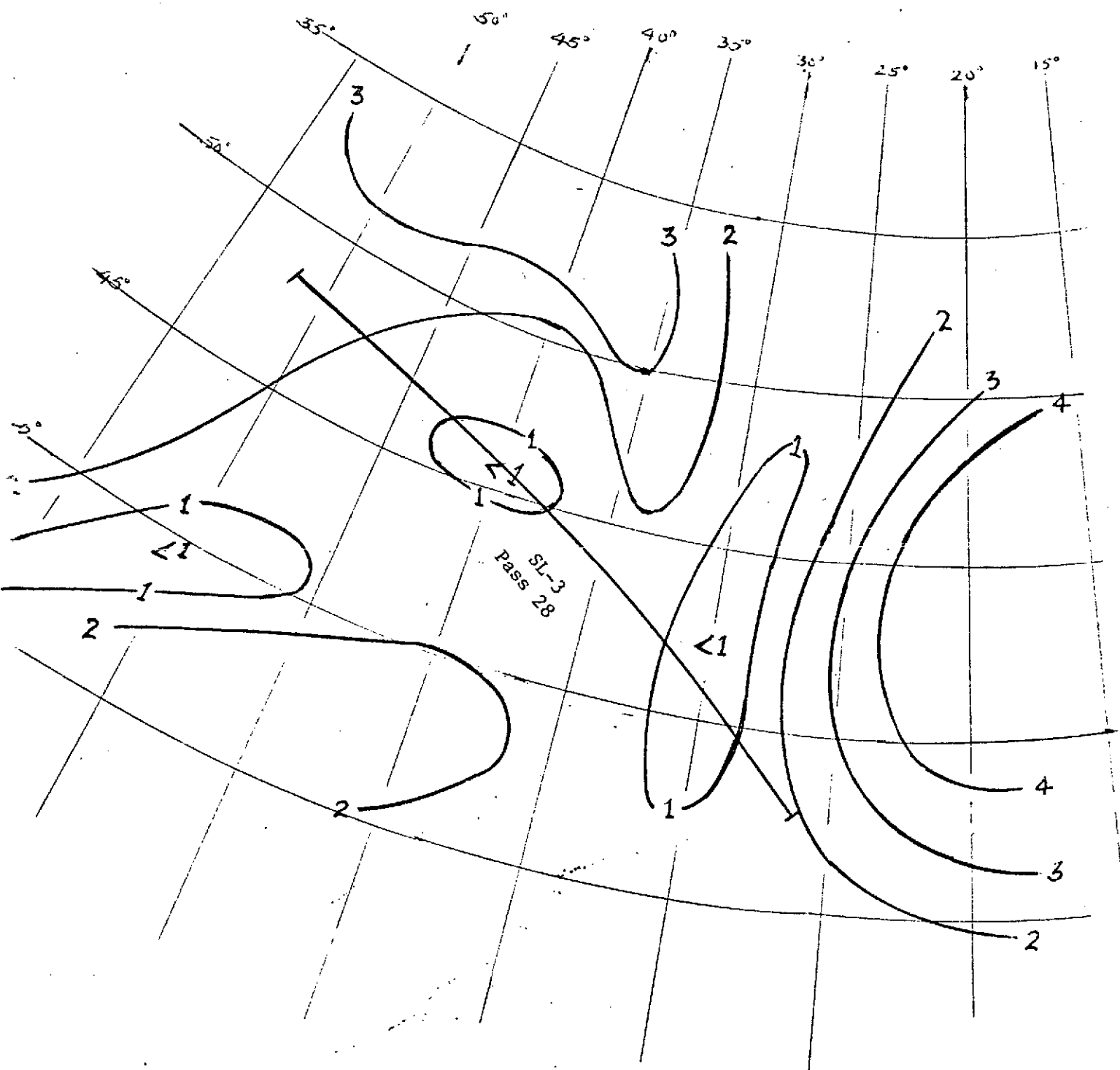


Fig. 2.4 Isolines of Significant Waveheight, September 13, 1973.

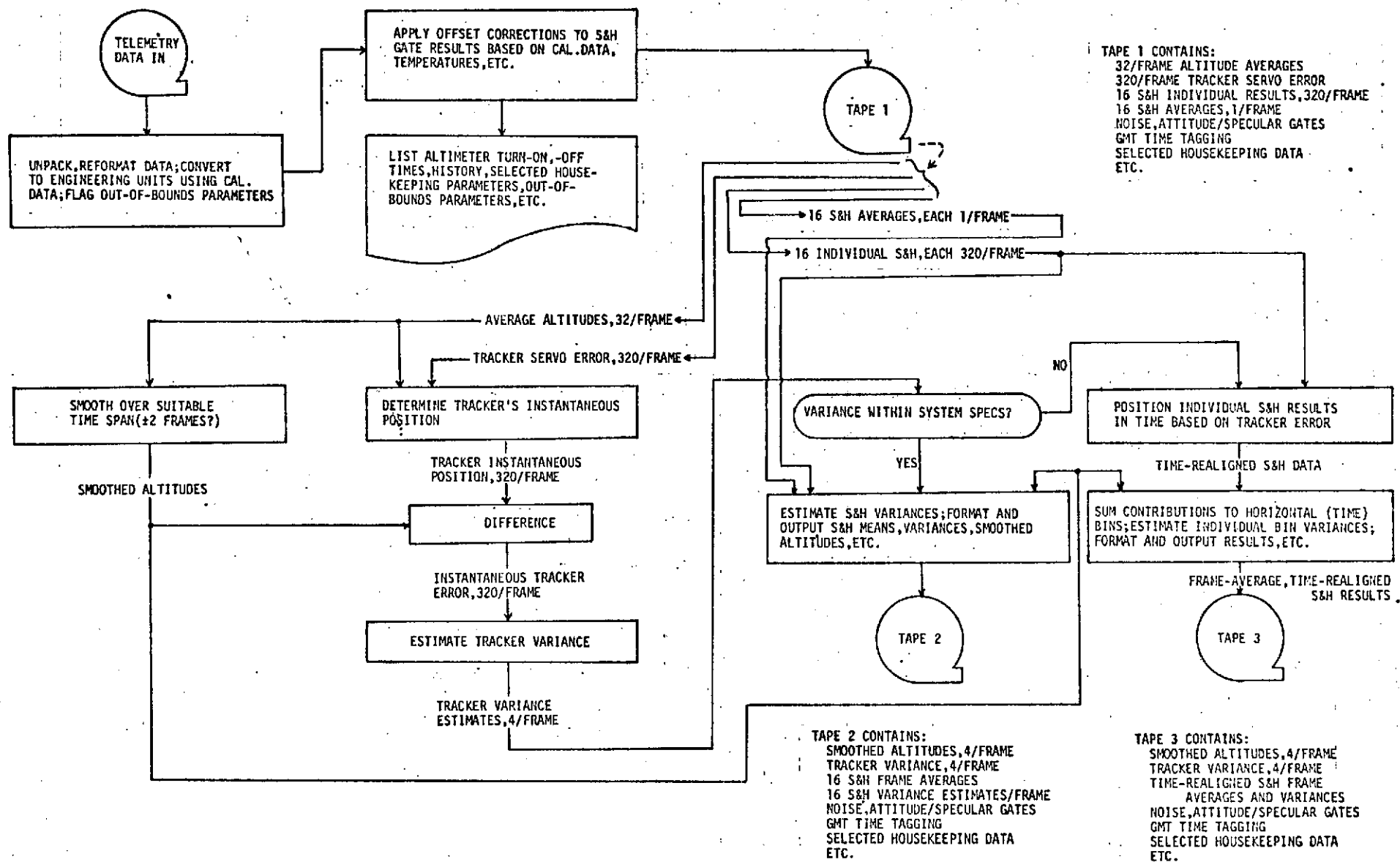


Figure 2.5 Geos-C Waveform Processing for Mode 2 (first of the two high-data-rate telemetry modes). 1 Frame = 3.277 seconds.

the greater the waveheight resolution. The upper limit on averaging period is determined by ocean surface homogeneity; typical data relating to waveheight spatial variability was given in Figures 2.3 and 2.4. Receiver noise can be shown to produce little effect on waveheight resolution for pre-detection signal-to-noise ratios ≥ 10 dB, and this effect will not be considered.

In the following we will assume that the point-target pulse shape and the waveheight probability distribution are both Gaussian functions. This will give rise to an average waveform which is a cumulative Gaussian, as shown in Figure 2.6, and will permit closed form analysis of several important parameters. Since the received waveform corresponds to the integral of a Gaussian which in turn is the convolution of pulse shape and waveheight Gaussian functions, the composite variance is:

$$\sigma_c^2 = \sigma_p^2 + \sigma_t^2$$

or from Figure 2.6 the composite standard deviation in nanoseconds is

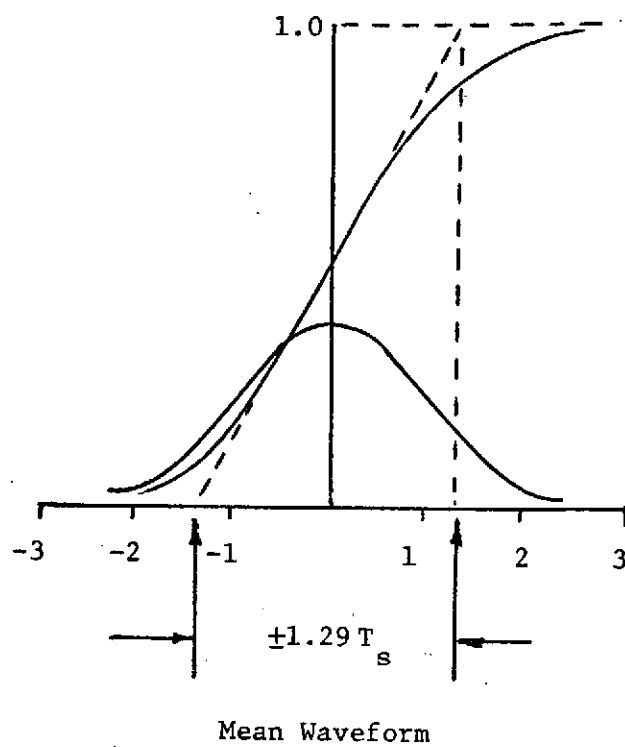
$$T_s = \sqrt{(.508 H_{1/3})^2 + (.602 T_p)^2}$$

where $H_{1/3}$ is a significant waveheight in feet and T_p is the 3 dB video pulse width in nanoseconds. Therefore, a ramp period, T_r (the dotted curve in Figure 2.6) may be defined as:

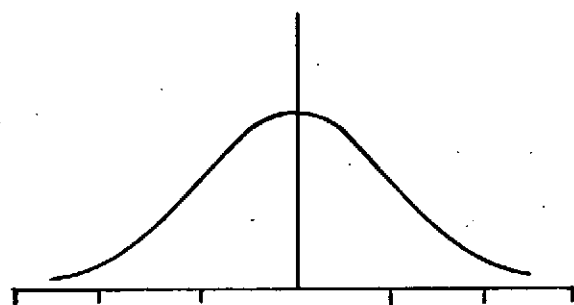
$$\begin{aligned} T_r &= 2.58 \sqrt{.258 H_{1/3}^2 + .362 T_p^2} \\ &= 1.31 \sqrt{H_{1/3}^2 + 1.4 T_p^2} . \end{aligned}$$

This represents the time expanse of the ramp period as defined by the projection of the mid-point slope as shown in Figure 2.6. On this basis the ramp period is equivalent to $1.55 T_p$ for the case of $H_{1/3} = 0$. Other rise time definitions could have been used. For example, rise time of pulse-like waveforms is sometimes taken as the 7 and 93 percent amplitude points. The definition used here is convenient because of its relationship to the mid-point slope.

First we consider the statistics of tracking jitter as these are affected by quantization and correlation properties of the altimeter system. In the



Radar Pulse Shape

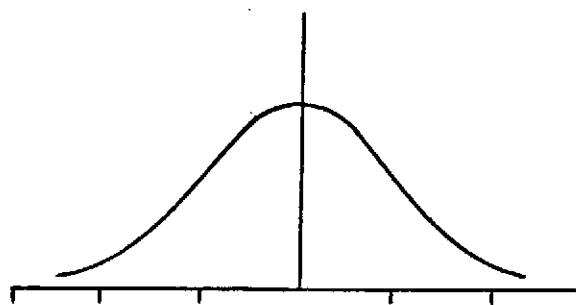


$$T_{3db} = .83\sigma_p$$

$$\text{or } \sigma_p = .602 T_p \quad (T_{3db} = 0.5 T_p)$$

for T_p = 3db video pulse width in ns

Wave Height Distribution



$$\sigma_{ft.} = \frac{c\sigma_t}{2}$$

$$\sigma_t = 2.03 \text{ ovt.}$$

$$H_{1/3} = 4 \text{ ovt.}$$

$$\sigma_t = \frac{2.03}{4} (H_{1/3}) = .508 H_{1/3}$$

(H 1/3 in ft.)

Figure 2.6 Waveform Relationships

Skylab altimeter, altitude tracker standard deviation and quantizer step-size were comparable in magnitude; therefore, on the average, the output signal constituted roughly a 4 level discrete random process. With the much smaller step-size used in the GEOS-C system, the range tracker signal more nearly resembles a continuous-time process.

Statistics of the mean-waveforms derive both from the chi-squared distribution of the basic received waveforms and from the superimposed time jitter of the tracking process. Since 100 statistically independent waveforms are received per second and the tracker jitter decorrelates in about 10 waveforms, the central question is the time-wise behavior of the combined process.

Starting with the normalized cumulative Gaussian to describe the mean waveform,

$$g(t) = \Phi\left(\frac{t-\mu}{T_s}\right) = \frac{1}{\sqrt{2\pi}} \int_{-\infty}^{(t-\mu)/T_s} \exp\left\{-\frac{x^2}{2}\right\} dx,$$

the probability that the jitter is $k\tau$ (where $\tau = 5/32$ ns is the GEOS-C quantization value) is given by the discrete Gaussian density function,

$$p_k = \Phi\left(\frac{(2k+1)\tau}{2\sigma_j}\right) - \Phi\left(\frac{(2k-1)\tau}{2\sigma_j}\right), \quad k = \pm 1, \pm 2, \pm 3, \dots$$

$$p_0 = \Phi\left(\frac{\tau}{2\sigma_j}\right) - \Phi\left(\frac{-\tau}{2\sigma_j}\right), \quad k = 0,$$

where μ is the mean on the time scale corresponding to the normalized mean voltage equal to 0.5, and σ_j is the standard deviation of the jitter process.

We first consider the idealized case in which the tracker signal only executes step changes every 10 pulses and then examine the validity of this simple model. Assume that $N_t = 10$ independent samples of the tracker signal and $N_{prf} = 100$ independent waveform samples are available per second; then it is desired to relate the variance of the average of N waveforms to the parameters T_s , $H_{1/3}$, and σ_j (assumed to be 3 ns), in order to provide some knowledge of sea state resolution. The time varying received signal has a χ^2 (chi-square) distribution with 2 degrees of freedom, with mean and standard deviation both equal to $g(t + k\tau)$ where $k\tau$ is the tracking jitter. With no jitter the average of $N = 100$ independent or uncorrelated signals would have

a variance equal to $g^2(t)/100$. With tracking jitter the average of 100 such waveforms would have a mean and variance as determined below.

The following derivation is limited to the determination of the mean and variance because the average of fifteen χ^2 variables can be assumed to have approximately a Gaussian distribution. Typically, the χ^2 distribution with 30 degrees of freedom is approximated by the Gaussian distribution. This would occur on averaging 15 χ^2 variables each with two (2) degrees of freedom because of the additive property of the χ^2 distribution. The determination of the mean is not affected by the correlation between successive values of the tracking jitter and the results given below are general in this respect. On the other hand, the correlation of the tracking jitter does affect the variance but this is minor when the sample size is large. The effect is small because: (1) jitter variance is small compared to the composite variance, and (2) relative length of the averaging period is large, (say, greater than 1 second) as compared to the less than 0.1 second period over which the correlation is positive. Utilizing these remarks, the following derivations are performed.

2.2.1 Computation of the Mean With Jitter Present

Let the average of $r = 10$ waveforms (for 0.1 sec.) be denoted by $\bar{v}(t)$ and for N waveforms (or $N/100$ seconds) by $\bar{\bar{v}}(t)$. The jitter value is fixed for r waveforms and then shifts to another value independently selected from the statistical distribution. This is an approximation to the actual waveform process with autocorrelation function given by Table 3.1, of [1] which shows that on the average, the actual waveforms shift and decorrelate in 0.1 seconds. The average of N waveforms will be given by:

$$\bar{\bar{v}} = \sum_k r n_k \bar{v}_k / N, \quad n = \sum n_k = N/r,$$

where

$$\bar{v}_k = \sum_{j=1}^{r n_k} v_j(t + k\tau) / r n_k$$

$$E\{\bar{\bar{v}}\} = E_{\underline{n}} E_{\underline{v}} (\bar{\bar{v}} | \underline{n})$$

$$= E_{\underline{n}} \{ \sum r n_k g(t + k\tau) / N \}$$

$$= \sum r n p_k g(t+k\tau)/N = \sum p_k g_k, g_k = g(t+k\tau).$$

If the jitter variable is denoted by X_1 and the composite variable (waveform) by X_2 , the sum (for the case $t = \mu$ which occurs at the midpoint of the ramp)

$$\sum p_k g(t+k\tau)$$

can be approximated very closely for small τ (jitter step in ns), by the integral:

$$\int \text{Prob. } \{X_1 \text{ is in the interval } (k, k+dk)\} \cdot \text{Prob. } \{X_2 \text{ is less than or equal to } k\} dk$$

and this is equivalent to:

$$P\{X_1 \geq X_2\}$$

which is equal to 0.5 for $t = \mu$ because X_1 is $N(0, \sigma_j)^*$ and X_2 is $N(0, T_s)$. If $t = \mu + T_s$ say, it can similarly be shown that the sum $\sum p_k g(t+k\tau)$ is approximately equal to

$$\text{Prob. } \{X_2 \leq X_1 + T_s\}$$

where X_1 and X_2 are distributed as above and thus $X_2 - X_1 - T_s$ is $N(-T_s, \sqrt{\sigma_j^2 + T_s^2})$. As an example, for $T_s = 8.8$, $\sigma_j = 3$, $T_s^2 + \sigma_j^2 = (9.3)^2$

$$\text{Prob. } \left[u \leq \frac{T_s}{\sqrt{\sigma_j^2 + T_s^2}} = 0.9462 \right] = 0.8279$$

Thus the mean is biased slightly downward at $t = \mu + T_s$; without jitter it is 0.8413. Figure 2.7 shows the mean waveform distortion due to uncorrected tracking jitter.

Note that this result can be generalized to any multiple m of T_s to yield

$$\sum p_k g(t+k\tau)$$

$$\approx \text{Prob. } \{X_2 \leq X_1 + mT_s\}$$

* This notation denotes X_1 is normally distributed with mean 0 and standard deviation σ_j .

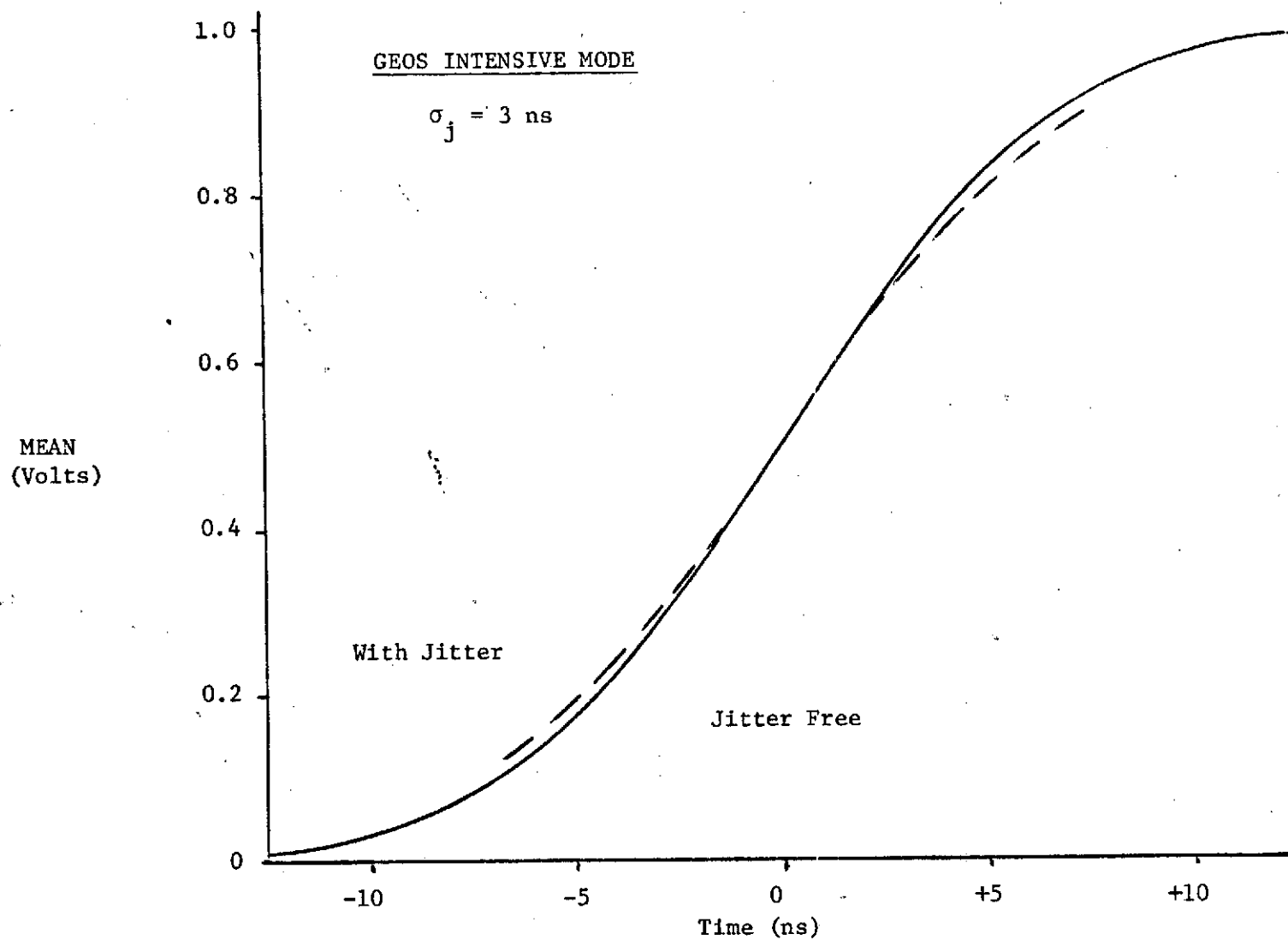


Fig. 2.7 Mean Waveform Tracking Jitter

given by

$$\text{Prob. } \left\{ u < \frac{mT_s}{\sqrt{\sigma_j^2 + T_s^2}} \right\},$$

where

$$T_s = \sqrt{(0.508 H_{1/3})^2 + (.602 T_p)^2}$$

σ_j = standard deviation of tracking jitter (in ns)

$H_{1/3}$ = waveheight (in feet)

2.2.2 Computation of the Variance With Jitter Present

The variance of $\bar{v}(t)$ is computed by use of the formula,

$$\sigma^2\{\bar{v}\} = E_{\underline{n}} \sigma_{\bar{v}}^2\{\bar{v}|\underline{n}\} + \sigma_{\underline{n}}^2 E_{\bar{v}}\{\bar{v}|\underline{n}\}.$$

See reference [2] for these general formulas for the unconditional means and variances in terms of the conditional means and variances. The subscript variable indicates the one with respect to which the moment is being taken conditional on the remaining variables being fixed.

$$E_{\underline{n}} \sigma_{\bar{v}}^2\left\{\frac{\sum r n_k \bar{v}_k}{N}\right\} = E_{\underline{n}} \frac{1}{N^2} \left[\sum r^2 n_k^2 g^2(t+k\tau)/r n_k \right]$$

$$= \frac{1}{r n} \sum p_k g_k^2$$

$$\sigma_{\underline{n}}^2 E_{\bar{v}}\{\bar{v}|\underline{n}\} = \sigma_{\underline{n}}^2 E_{\bar{v}}\left\{\frac{\sum r n_k \bar{v}_k}{N}\right\}$$

$$= \sigma_{\underline{n}}^2 \left\{ \frac{\sum r n_k g(t+k\tau)}{N} \right\}$$

$$= \frac{1}{n^2} \left[\sum g_k^2 \{n p_k (1-p_k)\} - 2 \sum_{k < \ell} g_k g_{\ell} n p_k p_{\ell} \right]$$

Substituting the results in equation (2) yields

$$\sigma^2\{\bar{v}\} = \frac{1}{r n} \sum p_k g_k^2 + \frac{1}{n} \sum g_k^2 p_k (1-p_k) - \frac{2}{n} \sum p_k p_{\ell} g_k g_{\ell}.$$

Using the following relationship

$$(\sum p_k g_k)^2 = \sum p_k^2 g_k^2 + 2 \sum_{k < l} p_k p_l g_k g_l.$$

The above becomes

$$\sigma^2\{\bar{v}\} = \frac{(r+1)}{rn} \sum p_k g_k^2 - \frac{1}{n} (\sum p_k g_k)^2.$$

If $n = 10$, $r = 10$, $N = 100$,

$$\sigma^2\{\bar{v}\} = \frac{11}{100} \sum p_k g_k^2 - \frac{1}{10} (\sum p_k g_k)^2.$$

The calculations become tedious for $\tau = \frac{5}{32}$ ns, as there are at least $2 \times 6 \times 32/5 = 87$ intervals for inclusion of 95% of the jitter values. An approximation was run by using $\tau = 40/32$ ns and the results extrapolated to $\tau = 5/32$ ns for the case in which

$$T_s = 8.8 \text{ ns}$$

$$\sigma_j = 3 \text{ ns}$$

$$t = \mu \text{ and } t = \mu + T_s.$$

In this example, at $t = \mu$,

$$\sum p_k g_k^2 \approx 0.2643, \sum p_k g_k = 0.5$$

$$E\{\bar{v}\} = 0.5.$$

Therefore with jitter

$$\sigma^2\{\bar{v}\} \approx (.064)^2.$$

Without jitter, assuming independence, $\sigma^2\{\bar{v}\} = (.05)^2$.

At $t = \mu + T_s$, $\sum p_k g_k^2 \approx 0.6927$, $\sum p_k g_k = 0.828$.

With jitter $E\{\bar{v}\} = 0.828$

$$\sigma^2\{\bar{v}\} = (.087)^2.$$

Without jitter, $\sigma^2\{\bar{v}\} = (.084)^2$.

These results are shown in Figure 2.8.

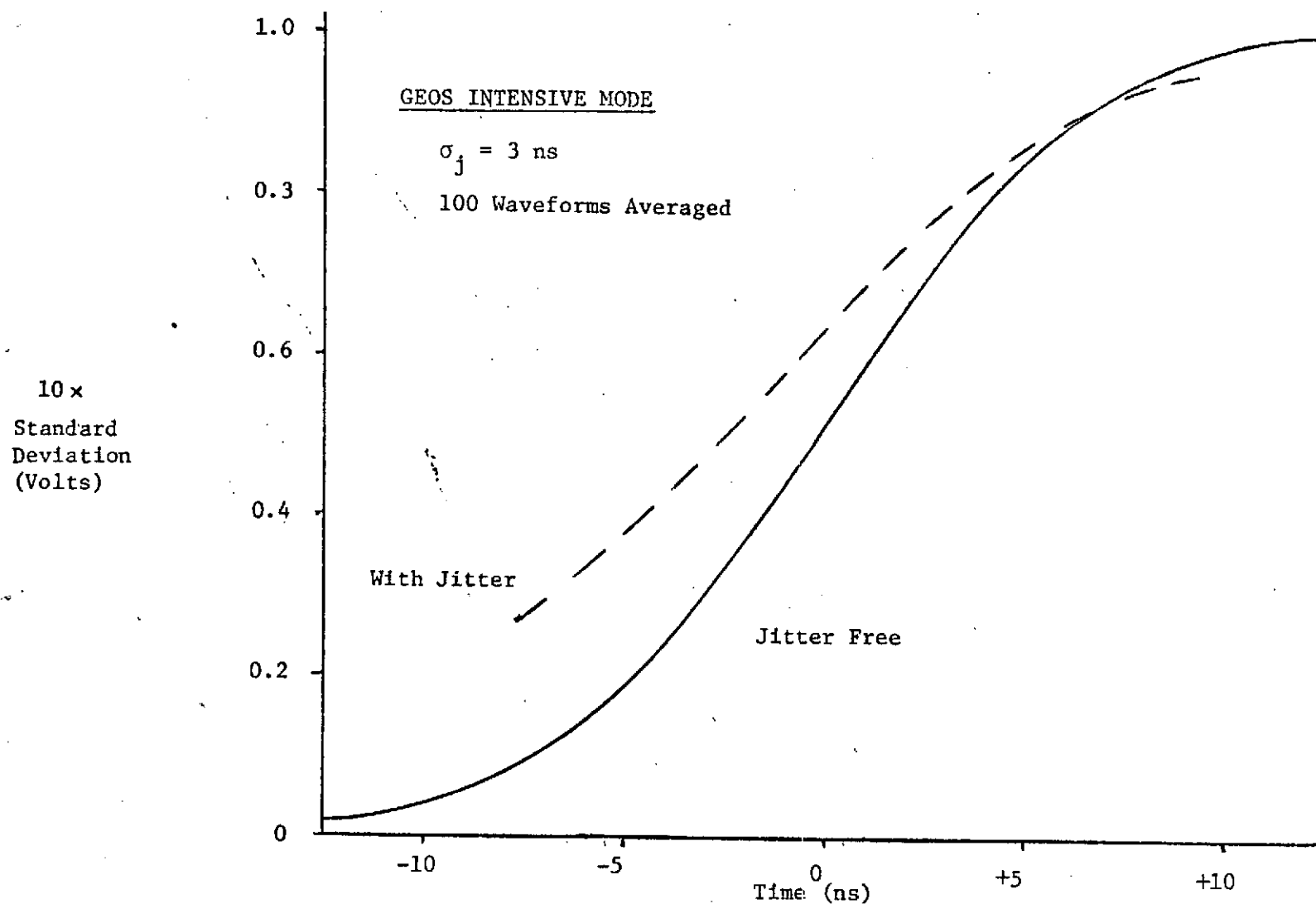


Fig. 2.8 Waveform Standard Deviation With and Without Tracking Jitter

2.2.3 Comments

Some comments or remarks concerning these results are in order. First suppose that the results are compared to that of averaging 100 independent waveforms with jitter present (no correlation). For $\sigma = 3$ ns, $T_s = 8.8$ ns, $t = \mu + T_s$, and for an approximation to be subsequently discussed,

$$\begin{aligned}\sigma^2 \text{ (1 waveform with jitter)} &= (\text{corrected mean})^2 + \frac{\sigma_j^2}{T_s^2} \frac{1}{\pi e} \\ &= (.836)^2\end{aligned}$$

$$\sigma^2 \text{ (average of 100 waveforms)} = (.0836)^2$$

which may be compared with the .087 results of the previous, more exact, analysis. Also note that the approximation which assumes that σ_j is fully correlated over 10 pulses

$$\sigma^2 \text{ (average of 100 waveforms)} = \frac{(\text{corrected mean})^2}{N_{\text{prf}}} + \frac{\sigma_j^2}{N_T T_s^2} \frac{1}{\pi e} = (.90)^2$$

(where $N_{\text{prf}} = 100$, $N_T = 10$)

is seen to result in the same order of approximation. As expected, variance of the true process is midway between two limiting cases of tracker signal correlation. The term $\sigma_j^2/T_s^2 \pi e$ in the above equations represents a transformation, by Taylor series expansion, of nanoseconds² to volts². Note that the formula for $\sigma^2\{\bar{v}\}$ is directly proportional to $1/n$, i.e., the variance decreases as n , or the standard deviation as $1/\sqrt{n}$. Also for $r = 1$, the result reduces to

$$\sigma^2\{\bar{v}\} = \frac{2}{n} \sum p_k g_k^2 - \frac{1}{n} (\sum p_k g_k)^2$$

This result is applicable when the autocorrelation function is zero.

The variance of \bar{v} increases slowly as r increases for N fixed (=100 say) as tabulated below for $N = rn = 100$, $t = \mu + T_s$.

r	n	$\sigma^2\{\bar{v}\}$
1	100	.0070
2	50	.0071
4	25	.0072
10	10	.0074

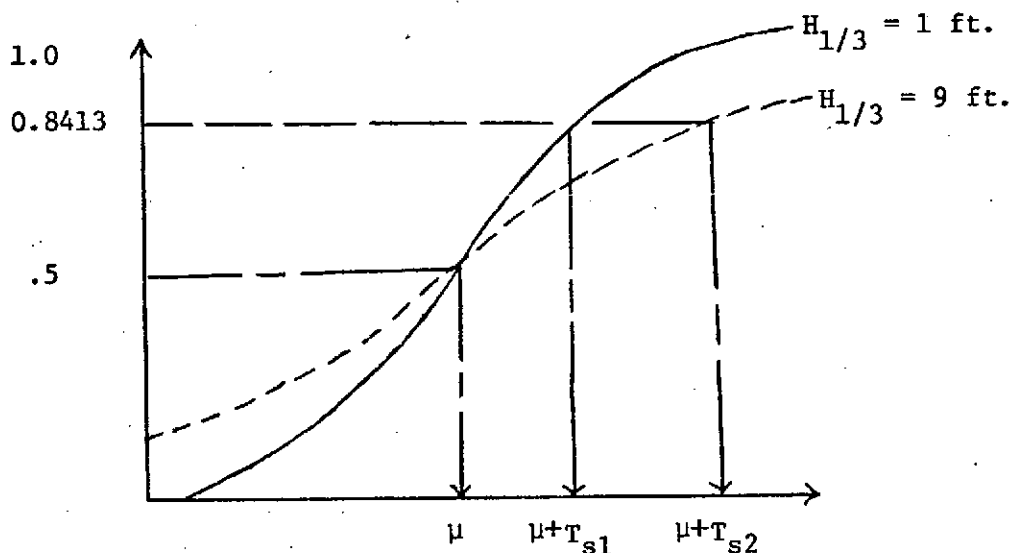
This shows the results to be largely insensitive to the detailed averaging properties of the tracking loop.

2.2.4 Sea State Resolution

Suppose that only significant waveheight is subject to change, then

$$\begin{aligned} T_s &= \sqrt{0.258 H_{1/3}^2 + .362 T_p^2} \\ &= \sqrt{0.258 H_{1/3}^2 + 56.63} \end{aligned}$$

for $T_p = 12.5$ ns. Assume that σ_j is given or has been measured to be 3 ns. The following figure illustrates the effect of SWH on the total variance of the process.



The difference of two values (for different $H_{1/3}$ values) is

$$\frac{T_{s2}^2 - T_{s1}^2}{0.258} = H_{1/3,2}^2 - H_{1/3,1}^2$$

The difference $T_{s2}^2 - T_{s1}^2$ is estimated by the difference in the estimated values obtained from the data or by squaring the values read from the cumulative distribution curves at 0.8413 and taking their difference. The values

from the curve are denoted by \hat{T}_{s2} and \hat{T}_{s1} , respectively. This difference is dependent on the $H_{1/3}$ values through the following approximation:

$$\hat{T}_{s2}^2 - \hat{T}_{s1}^2 = 0.258 (H_{1/3,2}^2 - H_{1/3,1}^2)$$

$$\hat{T}_{s2} - \hat{T}_{s1} \approx .0158 (H_{1/3,2}^2 - H_{1/3,1}^2)$$

and for $H_{1/3,1} = 6$ ft, $H_{1/3,2} = 1, 3, 9$, and 18 ft, the difference $T_{s2} - T_{s1}$ ranges from -0.56 to 4.61 ns. For $H_{1/3,1} = 9$ ft and $H_{1/3,2} = 1, 3, 6$, and 18 feet, $T_{s2} - T_{s1}$ varies from -1.29 to 3.91 ns. (See the following tabulation).

$H_{1/3,1} = 6$ ft.	(Approx.) $T_{s2} - T_{s1}$	$H_{1/3,1} = 9$ ft.	(Approx.) $T_{s2} - T_{s1}$
$H_{1/3,2} = 1$	-0.56	$H_{1/3,2} = 1$	-1.29
3	-0.43	3	-1.16
9	0.72	6	-0.72
18	4.61	18	3.91

Now consider the precision of the estimated variances (standard deviations) as read from the averaged waveform. The variance of the ordinate $\bar{v}(t)$ was obtained earlier as a function of n (no. of 0.1 second intervals), p_k , and g_k . For $t = \mu + T_s$, $H_{1/3} = 9$ ft, the estimated variance was given as 0.0076 volts^2 .

This variance in volts^2 can be transformed to nanoseconds^2 by using the Taylor series expansion of the Gaussian $\Phi(t_o; T_s)$. (The inverse of this was used earlier to convert jitter variance to a transformed jitter variance in volts^2). Given $t = \mu + T_s$ and

$$v \approx \Phi(t_o; T_s) + (t-t_o) \phi(t_o; T_s) + \dots$$

$$\sigma\{v\} \approx \frac{1}{T_s \sqrt{2\pi e}} \sigma\{t\}.$$

Thus

$$\sigma\{t\} = T_s \sqrt{2\pi e} \sigma\{\bar{v}\}$$

and using $\sigma^2\{\bar{v}\} = 0.0076$, the variance of a 1 second average, the following values are obtained for several averaging periods.

Table 1

$\sigma\{t\}$, $\sqrt{2}\sigma\{t\}$ vs. Averaging Time (Seconds) at $t = \mu + T_s$, $v(t) = 0.8413$

Averaging Time (Seconds)	$\sigma\{t\}$	$\sqrt{2}\sigma\{t\}$
1	3.17	4.48
10	1.01	1.43
20	0.72	1.02
40	0.51	0.72
80	0.36	0.51
120	0.29	0.41

Assuming that the difference in two times has a standard deviation of $\sqrt{2} \sigma\{t\}$ (since the times are assumed to be equal under the hypothesis of no difference) then the above results need to be multiplied by $\sqrt{2} = 1.414$, see last column of Table 1. Hence, for average waveform data collected over one second, the standard deviation of the observed difference is estimated to be 4.48 ns.

In comparing data for $H_{1/3} = 9$ ft with that for $H_{1/3} = 1$ ft, the expected or average difference of $T_{s2} - T_{s1} = 1.29$ ns. The probability that the hypothesis $T_{s1} - T_{s2}$ will be rejected is given by the power of the test (see [3], p. 229).

$$\lambda = \frac{1.29}{1.02} = 1.265, \text{ Power} = .24 \text{ for } \alpha = .05$$

i.e., for a level of significance of $\alpha = 0.05$ (a 5% risk of stating that the $H_{1/3}$'s differ when in fact they do not differ), the probability that the $H_{1/3}$'s will be indicated as different is approximately 0.24. If $\lambda = 2.8$, the power is 0.80, i.e.

$$T_{s2} - T_{s1} = 2.8 (1.02) = 2.86,$$

a value exceeded only by comparing $H_{1/3} = 9$ ft vs. $H_{1/3} = 18$ feet.

Similar results may be obtained using a chi-squared formulation. For an averaging period of 10 seconds, first assume that 10 waveforms are available, averaged over 1 second. From the above tabulation the standard deviation to be associated with a one-second average waveform is 4.48 ns. In order to obtain uncertainty values for an 80% confidence bound, chi-squared (χ^2) values for 10 and 90% levels are used, i.e.,

$$\begin{aligned}\sigma_{\text{MAX}}^2 &= \frac{n\sigma^2}{\chi_{10\%}^2} & \sigma_{\text{MIN}}^2 &= \frac{n\sigma^2}{\chi_{90\%}^2} \\ &= \frac{9(4.48)^2}{4.17} & &= \frac{9(4.48)^2}{14.68} \\ \sigma_{\text{MAX}} &= 6.58 & \sigma_{\text{MIN}} &= 3.51,\end{aligned}$$

where n = number of degrees of freedom. Using the previous equation

$$T_{s2} - T_{s1} = .0158 (H_{1/3,2}^2 - H_{1/3,1}^2)$$

with the above range of σ values; as an example if one $H_{1/3}$ value is taken as 8 ft, we find the other to be 16.1 ft. As another example for $H_{1/3,1} = 3$ ft, we find $H_{1/3,2} = 14$ ft. This means that the probability that a waveheight observation will lie within these values is 80 percent.

The preceeding analysis has focused on the general statistical aspects of the mean waveform, variance, and waveheight estimation areas. This work will next be used as a framework for deriving an approximate, closed form solution to the waveheight resolution question. The initial problem formulation assumed Gaussian functional forms for both the system waveshape and the waveheight probability distribution function based on justifications given in [4] and [5], and because this leads to analytical tractability. Without the latter assumption, as must be the case with initial radar altimeter waveform studies, a considerably more complex deconvolution approach is needed to extract waveheight information. That is, for the Gaussian assumption only a differentiation is required to recover the combined system waveshape and waveheight distribution. Except for the increase in process

variance which may result from differentiation, we know that the $\pm T_s$ point on the mean waveform will directly map on the differentiated waveforms. For this reason the following waveheight analysis considers only the average received waveforms. For future reference, note that variances will propagate through differentiation (for a continuous-time analogy) as follows: for the signal power spectrum, which at the output of the square-law detector is the convolution of the IF spectrum, $S(\omega)$, the differentiated process variance, σ_p^2 , is

$$\sigma_p^2 = \int_0^{\infty} \omega^2 S(\omega) d\omega.$$

For the noise spectrum (this analysis is assumed free of receiver noise) an identical form applies. Therefore, the differentiation operation will alter the signal-to-noise relationship only to the extent that these spectra differ (c.f., [1] for a computation of $S(\omega)$). For essentially band limited processes, this factor is rather small.

To proceed, the previous analysis showed that the waveform standard deviation in volts could be transformed into time uncertainty $\sigma(t)$, as

$$\sigma(t) \simeq \frac{T_s \sqrt{2\pi e}}{\sqrt{t}}, \quad \sigma(\bar{v}) \simeq \frac{0.36 T_s}{\sqrt{t}}$$

t in seconds.

Also as previously discussed, the approximate total time uncertainty is due to the uncorrelated variance of T_s along with σ_j ; the waveform statistics and the tracking jitter random sources. Denoting the combined one-sigma variance as $\sigma(t)$,

$$\sigma^2(t) \simeq \frac{(0.36 T_s)^2}{t} + \frac{\sigma_j^2}{10t}.$$

Using the previously defined value for T_s ,

$$T_s = .602 \sqrt{.712 H_{1/3}^2 + T_p^2}.$$

and using a differential of T_s to convert the time uncertainty $\sigma(t)$ into an $H_{1/3}$ uncertainty gives

$$\Delta T_s \approx \frac{.428 H_{1/3} \Delta H_{1/3}}{\sqrt{.712 H_{1/3}^2 + T_p^2}}$$

Equating $(\Delta T)^2$ with $\sigma^2(t)$ and substituting for T_s gives a significant wave-height uncertainty $\sigma_{H_{1/3}}$ of

$$\sigma_{H_{1/3}} \approx \frac{\sqrt{.256(.712 H_{1/3}^2 + T_p^2)^2 + .546\sigma_j^2(.712 H_{1/3}^2 + T_p^2)}}{H_{1/3} \sqrt{t}}$$

This gives a first order solution to the one-sigma uncertainty in wave-height resolution. In accordance with previous work [6], we adopt an 80 percent confidence bound (for a Gaussian process this bound is approximately 1.3σ). Therefore

$$H_{1/3} \text{ resolution} \approx \frac{\sqrt{.433(.712 H_{1/3}^2 + T_p^2)^2 + .923\sigma_j^2(.712 H_{1/3}^2 + T_p^2)}}{H_{1/3} \sqrt{t}}$$

(80% confidence bound)

The results obtained using the above approximate formulation may be compared to the two previously given results and seen to be in satisfactory agreement. Graphical results, obtained through use of this last equation, were discussed at the beginning of this section.

References

1. Miller, L. S., G. S. Brown and G. S. Hayne, "Engineering Studies Related to Geodetic and Oceanographic Remote Sensing Using Short Pulse Techniques," Final Report, Contract No. NAS6-2135, Research Triangle Institute, Durham, North Carolina, February 1973.
2. Panjer, H. H., "On the Decomposition of Moments by Conditional Moments," The American Statistician, Oct. 1973, Vol. 27, No. 4, pp. 170-171.
3. Hald, A., Statistical Theory With Engineering Applications, John Wiley & Sons, Inc., 1952.

4. Kinsman, B., Wind Waves, Prentice Hall, 1965.
5. Papoulis, A., Systems and Transforms with Applications in Optics, McGraw Hill Co., 1968.
6. Hofmeister, E. and B. Keenery, "Radar Altimeter Return Waveform Sampling Study," Final Report on NASA Contract No. NAS6-1823, Oct. 1971.

3.0 SPATIAL FILTER EFFECT AND OPTIMAL FILTER FOR GEOID DATA PROCESSING

3.1 Geoidal Data Processing Results

The purpose of this section is to present derivations and results relating to optimum data processing methods and required data rates for GEOS-C altitude information. The first part of this section addresses the effects of (1) geoidal power spectral density, (2) spatial filter function, and (3) altimeter measurement random error on data processing characteristics. Weighting functions are derived for both undulation and slope filtering based on geoidal spectral data extracted from the Skylab altimeter observations. The results are optimal in an additive Gaussian noise, minimum-mean-square error sense and largely represent an extension of the earlier work of Cohen and Zondek [1]. The second part of this section gives a detailed analysis of the spatial filter effect which results from the finite area illuminated by the altimeter. We assume that the altimeter spatial filter effect averages over all significant waveheight spectral components.

Results of the analyses argue that the GEOS-C altimeter will be capable of measuring geoidal components to a short wavelength cutoff in the neighborhood of 20-40 km for geographic regions containing pronounced short-wavelength features. For a satellite ground-track velocity of ~ 7 km/sec, this corresponds to a Nyquist frequency of ~ 0.3 Hz. Taking this Nyquist rate and the time-expanse of the derived weighting functions as a measure of the geoidal information rate of the altimeter, the GEOS-C 10 sample/second data base is considered to be more than adequate.

Figure 3.1 displays a power-spectral-density (PSD) plot for the Puerto Rican Trench region which was computed using fast Fourier Transform methods and a Hanning type convolutional window. The data base comprised SL-2, Pass 4, Mode 5 with 100 and 130 nanosecond pulsewidths (pulse compression was not functioning during SL-2). The Puerto Rican Trench data was used since we desired to obtain PSD results for an anomalous region, which should contain more energy in short-wavelength components than anomaly-free regions. The PSD so obtained, and data processing results derived therefrom, should represent the best opportunity for the altimeter to obtain information relating to short wavelength undulations and should yield an approximate upper bound on data processing requirements.

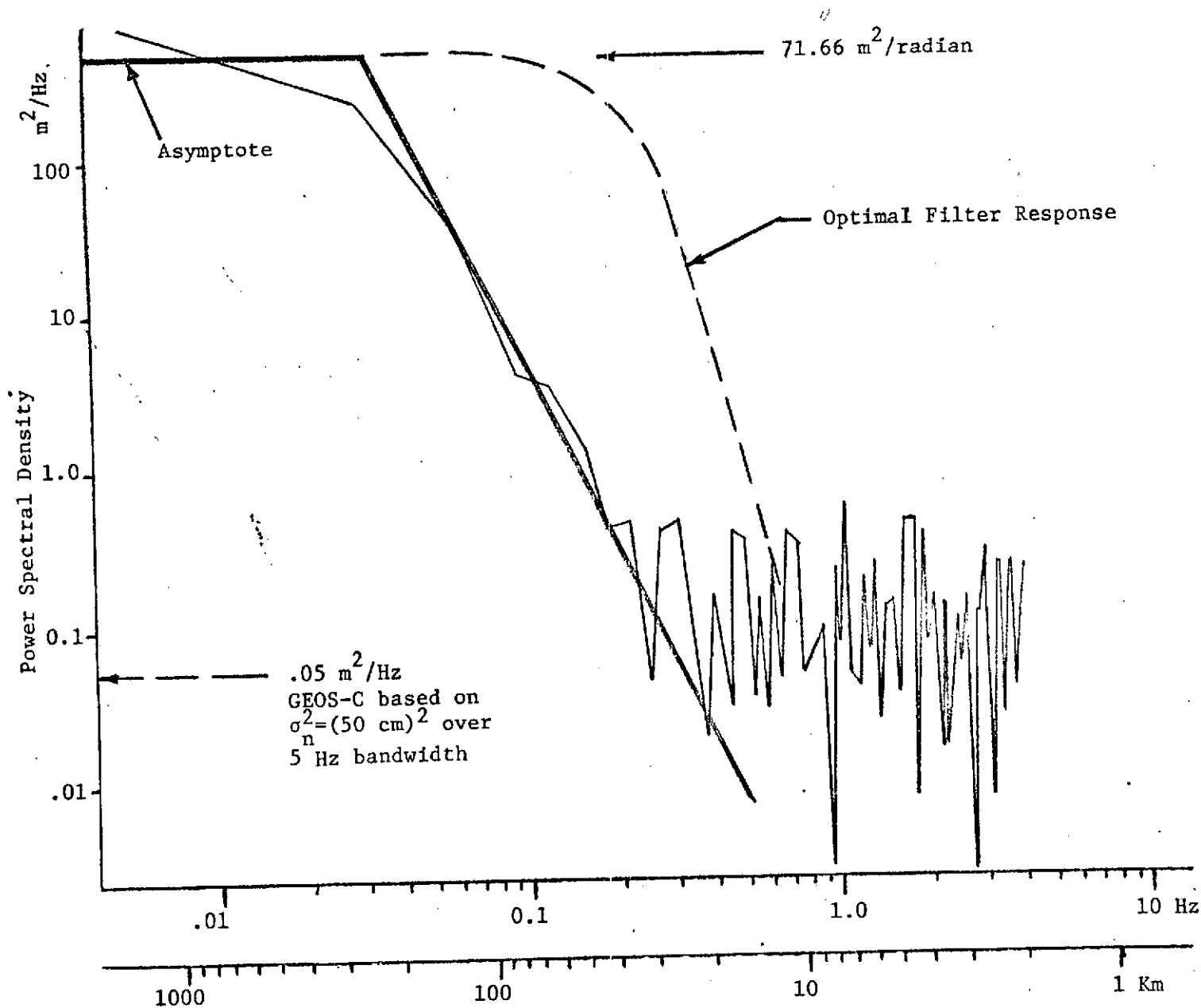


Fig. 3.1 Geoid Undulation Spectrum of Puerto Rican Trench Area and Wiener Filter Transfer Function.

Referring to Figure 3.1, the dashed line corresponds to the density level for which a 5 Hz rectangular bandwidth, white noise spectrum would yield an rms level equal to 0.5 meters. Since the S-193 tracker has approximately a 3.3 Hz equivalent noise bandwidth, this level constitutes an approximation to known GEOS-C intensive-mode system characteristics. The noise level shown in the calculated spectrum represents the Skylab altimeter noise level (1-2 meters rms). We will subsequently verify that the spatial filter function corresponds to considerably shorter wavelengths (less than 10 km) and that the calculated PSD is not contaminated by the altimeter footprint effect.

Note that the observed spectrum represents an asymptotic behavior which in the frequency parameter (f) is approximately f^{-4} . As discussed in [2], Kaula's model of one-dimensional spectral behavior behaves as f^{-3} .

Since observable geoidal components are of much longer wavelengths than spatial filter effects, we interpret the data in Figure 3.1 as a cut through a two-dimensional spectrum. In wave-number space (k_x, k_y) a directional spectrum $S(k_x, k_y)$ with a k^{-4} behavior will yield a one-dimensional asymptotic behavior of k^{-3} (due to integration over the angular coordinate of the polar coordinate set). Therefore, we feel that the observed spectrum depicts the proper theoretical behavior.

The optimization technique we use is the Wiener-Hopf formulation, which for the correlation functions $R(\cdot)$ of signal s and observation y , gives the optimum impulse response $h_o(t)$ as the solution to the integral equation [3]

$$R_{sy}(\tau+\eta) = \int_0^{\infty} h_o(\mu) R_y(\tau-\mu) d\mu \quad \tau \geq 0.$$

For non-real time processing, an estimate of a value at time t can be based on both past and future values. Therefore, the proper lower limit on the integral is $-\infty$ and the integral equation becomes a convolution form which is readily solved by transform theory. For our purposes the form of the solution is [3]

$$H(\omega) = \frac{S(\omega)}{S(\omega) + N(\omega)}$$

where $S(\omega)$ is the geoid undulation power spectrum and $N(\omega)$ is the additive noise spectrum. Since the altitude tracker has a noise equivalent bandwidth of ~ 5 Hz

and a random error standard deviation of ~ 0.5 m, $N(\cdot)$ may be represented as a white noise spectrum with a density of $(.5)^2 \text{m}^2 / 5 \text{ Hz} = .05 \text{ m}^2 / \text{Hz}$ or $7.96 \times 10^{-3} \text{ m}^2 / \text{radian}$. Using the break-point approximation (the asymptotes of which are shown in Figure 3.1) to $S(\omega)$ as

$$S(\omega) = \frac{71.66 \cdot 6.554 \times 10^{-4}}{\omega^4 - .0512\omega^2 + 6.554 \times 10^{-4}}$$

the optimum transfer function is found to be

$$H_o(\omega) = \frac{5.9}{\omega^4 - .0512\omega^2 + 5.9006}$$

This function is also shown in Figure 3.1. Note that the asymptote is twice as steep as the spectral decay. At the intersection of the break-point spectral approximation and the GEOS-C noise level (which occurs at ~ 22 km), $H_o(\omega)$ introduces an attenuation of ~ 12 dB. The 3 dB attenuation point occurs at ~ 40 km.

Figure 3.2 shows the spatial filter response function for the GEOS-C system, which is derived in section 3.2. Note that the solution $[H_o(\omega)]$ given above effectively truncates geoidal data at considerably longer wavelengths than does the spatial filter effect (its 3 dB point occurs at ~ 10 km). Had this not been the case, a considerably more involved Wiener-Hopf form would have been required.

The optimal filter $H_o(\omega)$ has been inverse Fourier transformed through use of contour integration, and the normalized impulse response found to be

$$h(t) = e^{-0.8755t} (\cos 1.289t + 0.6792 \sin 1.289t) \text{ for } t > 0.$$

Knowing that the optimal geodetic slope filter is the derivative of the optimum undulation filter, the impulse response for slope estimation is

$$\begin{aligned} \frac{d h(t)}{dt} = & -0.8755 e^{-0.8755t} (\cos 1.289t + .6792 \sin 1.289t) \\ & + e^{-0.8755t} (.8755 \cos 1.289t - 1.289 \sin 1.289t) \text{ for } t > 0. \end{aligned}$$

The undulation filter impulse response will be an even function of time, whereas the slope filter impulse response will be an odd function [1]. Both response

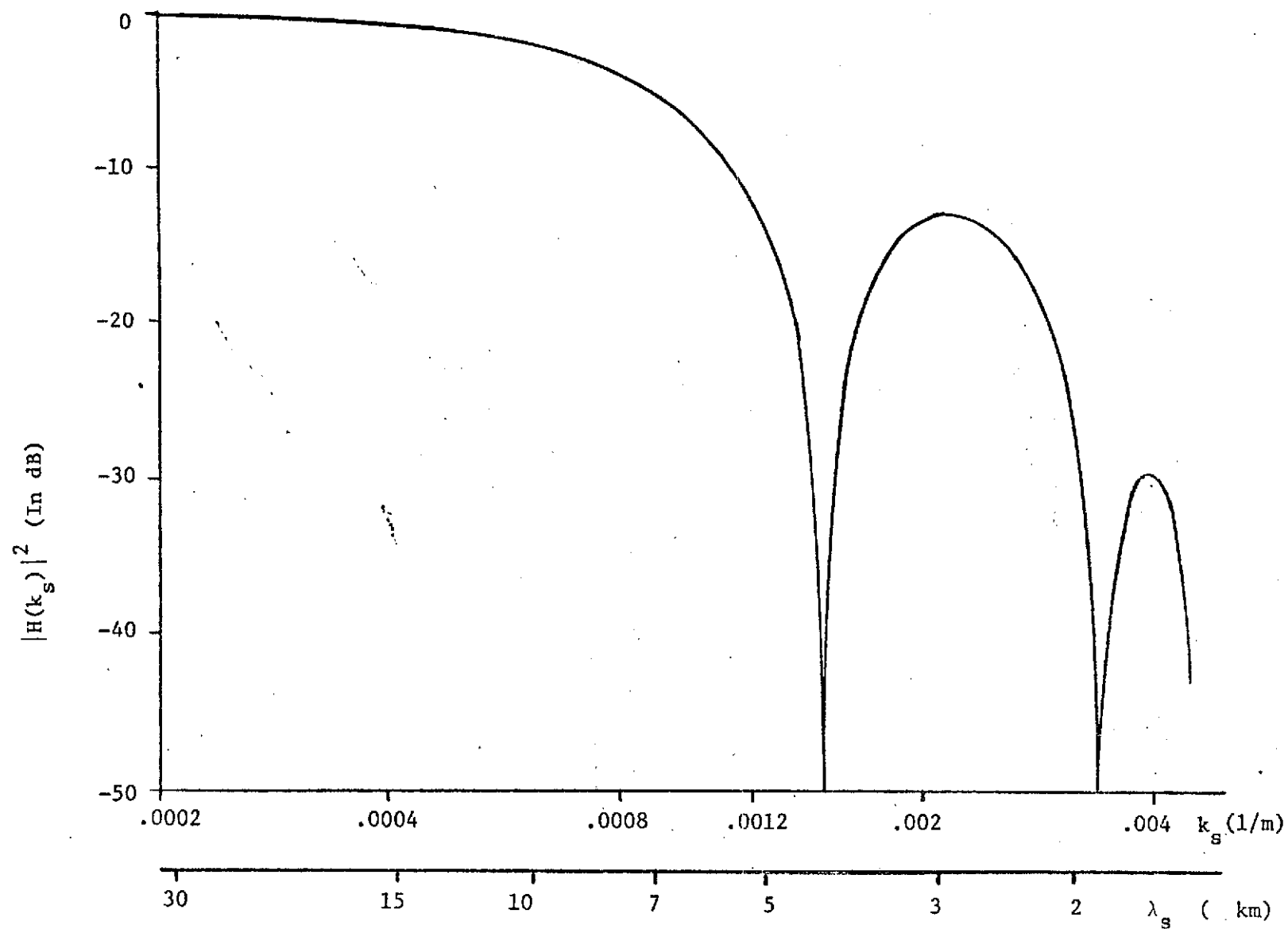


Fig. 3.2 GEOS-C Intensive Mode Spatial Filter Transfer Function for Calm to Moderate Seas.

functions are graphed in Figure 3.3 and tabulated values are given in Appendix A. This figure shows the overall characteristics of the two filters; for digital computer implementation the response functions must be truncated and properly re-normalized. To insure that the long wavelength structure is invariant under discrete-time filtering, the truncated convolution weighting coefficients should sum to unity. Also, in application of this form of filtering, the geoid power-spectral density of the actual area of interest should be investigated and the mean square error properties, given by

$$e = \frac{1}{2\pi} \int_{-\infty}^{\infty} H_0(\omega) N(\omega) d\omega,$$

should be compared with weighting functions which are computationally more efficient (e.g., rectangular or arithmetic moving average). It is interesting to note that the time expanse of an ideal rectangular impulse response function which has a $\sin x/x$ frequency domain response that matches $H_0(\omega)$ at the 3 dB point, corresponds to an averaging period or impulse response width of 2.22 seconds. The $h_0(t)$ form shown in Figure 3.3 has a width at the e^{-1} points of ~2 seconds.

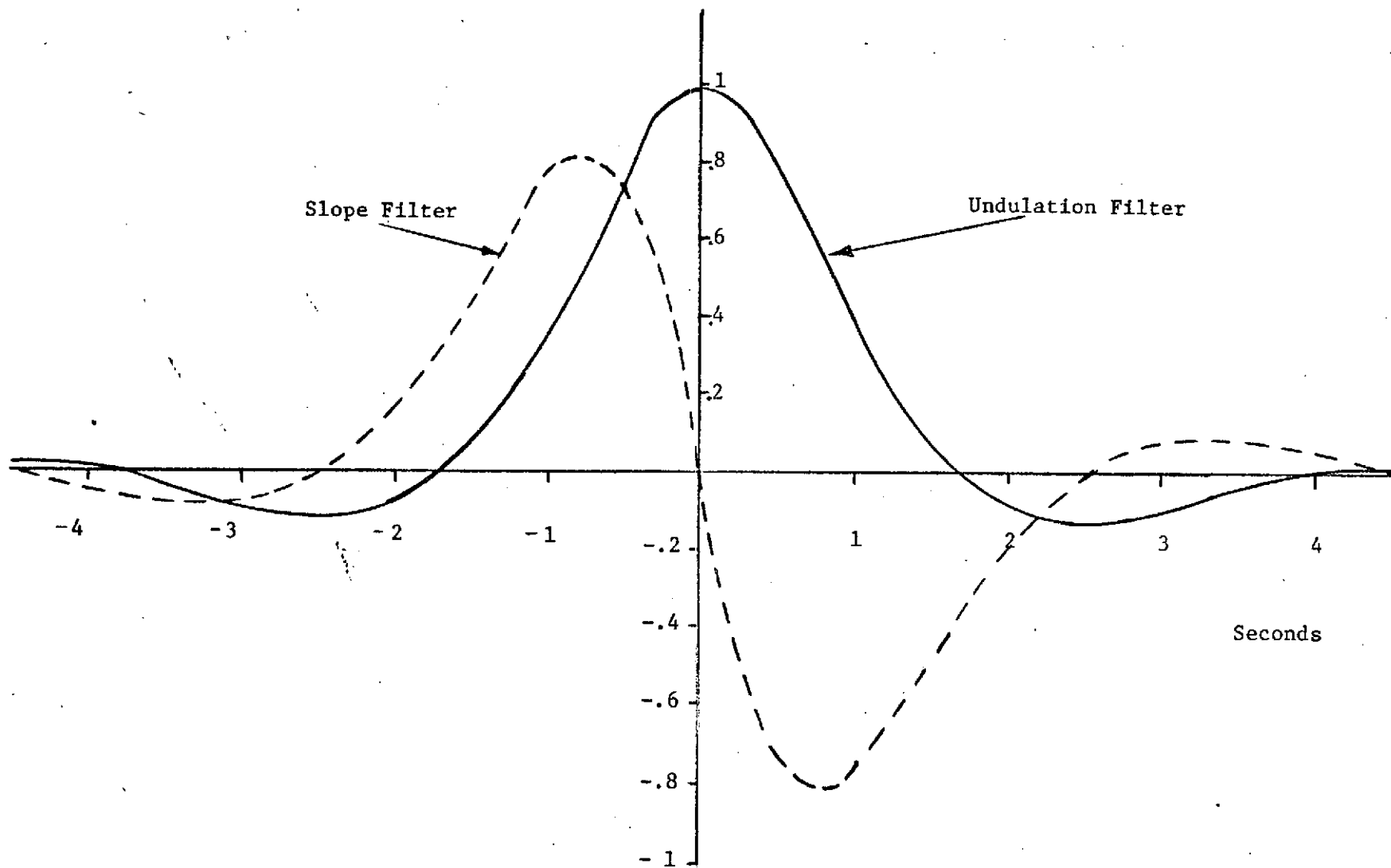


Fig. 3.3 Derived Weighting Functions for Geoidal Data Processing.

3.2 SPATIAL FILTER EFFECT

3.2.1 Background Discussion

The term spatial filtering effect as applied to radar altimetry denotes the ideal, i.e., noise-free, capability of the altimeter to resolve surface features. Spatial filtering is inherent in an altimeter system because of the non-zero width of the system point-target response. Thus, even if we consider the measurement process to be noise-free, the above factor limits the ability of the system to "map" small scale surface features.

Typically, one calculates the radar footprint radius R for pulse-length limited geometries from the relationship

$$R = \sqrt{hcT}$$

where h is the satellite altitude, c is the speed of light, and T is the radar pulse length. It is then assumed that the footprint diameter ($2R$) approximates the minimum surface wavelength which the altimeter can measure, and that the altimeter response is essentially flat for surface wavelengths greater than $2R$ and zero for wavelengths less than $2R$. In essence then, the altimeter is treated as an ideal (rectangular) low-pass filter whose cut-off frequency is determined by the transmitted pulse length. While such a characterization of the altimeter may be sufficient for "order-of-magnitude" calculations, it is inadequate for more precise system modeling. The problem of specifying altitude sampling rates and optimal data filtering require that the asymptotic (high frequency) behavior of the altimeter spatial filter characteristics be investigated.

In a previous work [4], approximate formulas were obtained for determining the effect of a one-dimensional, sinusoidal, corrugated surface on the mean return waveform. Upon further analysis, we have determined that the approximations used to obtain those formulas are not always valid. In this report we correct this formulation for the scattering process to obtain the effects of the surface on the mean return waveforms. For the GEOS-C altitude, pulse width and split-gate tracking configuration we obtain results which illustrate the sensitivity of the system to surface undulation wavelengths.

For the purposes of this report we will represent the geoidal surface undulation as a single sinusoid of small amplitude and very low frequency. In other words we will assume that on a very localized basis the geoidal perturbations of the mean flat sea may be represented as a sinusoid of relatively small

amplitude and low frequency. The analysis could be extended to the case of two or more surface harmonics; however, the analysis and computations become prohibitively tedious.

The geometry of the problem is shown in Figure 3.4 along with a definition of pertinent terms. We assume that the surface undulations vary in one direction only. That is, the deterministic component of the surface height may be represented as

$$z_s = a_s \sin(k_s \tilde{\rho} \cos \phi - \alpha_s)$$

where a_s is the peak amplitude of the undulation, $k_s = 2\pi/\lambda_s$ is the wave-number, and α_s is the "phase" of the surface directly beneath the altimeter. For the time being, the altimeter will be considered to be fixed relative to the surface.

3.2.2 Determination of the Mean Return Waveform

The mean return waveform is given by the following expression [5]

$$P_r(t) = \frac{\lambda^2}{(4\pi)^3} \int \frac{P_t(t - \frac{2r}{c}) G^2(\Theta, \omega) \sigma^0(\Theta, \omega)}{r^4} dA \quad (1)$$

SCATTERING
AREA

where t is the time relative to the time of transmission and dA is the elemental scattering area on the ocean surface. For purposes of this analysis, we consider the altimeter antenna to be nadir pointed, thus $\omega = \phi$ and $\Theta = \psi$. We also will only consider the case of pulse width limited geometries and very short pulses, i.e.

$$P_r(t) \approx \frac{\lambda^2 G_o^2 \sigma^0}{(4\pi)^3} \int \frac{P_t(t - \frac{2r}{c})}{r^4} dA \quad (2)$$

where G_o is the boresight gain of the antenna and σ^0 is the surface scattering cross-section per unit scattering surface at 0° angle of incidence. If we define r_o as the distance from the altimeter to the point on the $z = 0$ surface which is at the same radial distance $\tilde{\rho}$ as the intersection point of r with the true mean surface, then from Figure 3.5

$$r \approx r_o - \frac{z_s}{\sqrt{1 + (\tilde{\rho}/h)^2}},$$

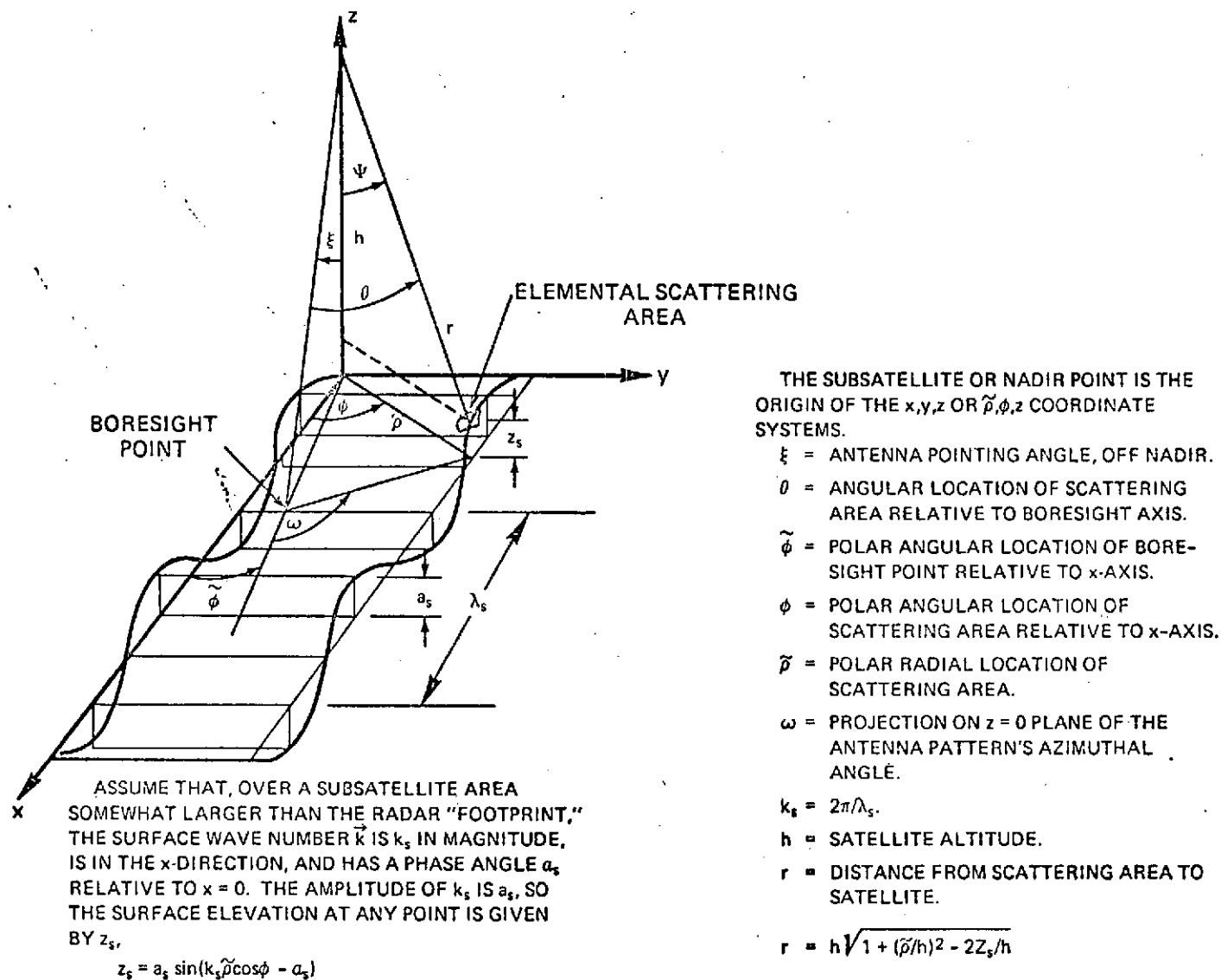


Fig. 3.4 Satellite-Ocean Surface Geometry and Summary of Notation.

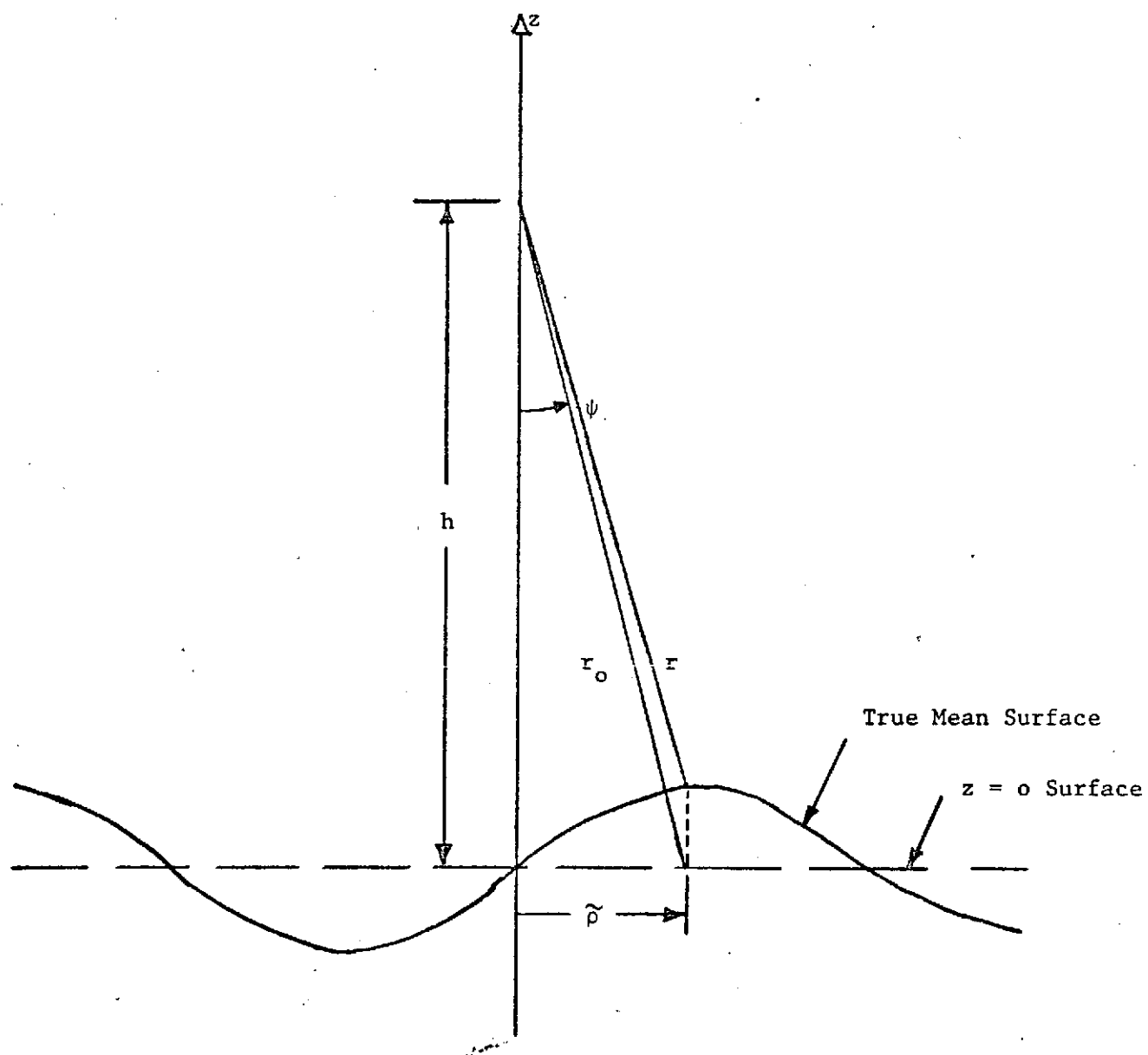


Fig. 3.5 Diagram Illustrating the Relationship Between the Distance from the Altimeter to the True Surface (r) and to the Mean Flat Surface (r_0).

where $r_o = \sqrt{\tilde{\rho}^2 + h^2}$ and $z_s = a_s \sin(k_s \tilde{\rho} \cos \phi - \alpha_s)$; thus

$$t - \frac{2r}{c} = t - \frac{2r_o}{c} + \frac{2z_s}{c} \frac{1}{\sqrt{1 + (\tilde{\rho}/h)^2}}$$

where c is the speed of light. For $\tilde{\rho} \ll h$,

$$t - \frac{2r}{c} \approx t - \frac{2h}{c} - \frac{\tilde{\rho}^2}{ch} + \frac{2z_s}{c}.$$

Equation (2) becomes

$$P_r(t) \approx \frac{\lambda^2 G_o^2 \sigma^o}{(4\pi)^3} \int \frac{P_t(t - \frac{2h}{c} - \frac{\tilde{\rho}^2}{hc} + \frac{2z_s}{c})}{r_o^4} dA. \quad (3)$$

where we have approximated the r^{-4} factor by r_o^{-4} . Substituting $\tau = t - \frac{2h}{c}$ and approximating dA by $\tilde{\rho} d\tilde{\rho} d\phi$, i.e., we integrate over the $z = 0$ plane but retain the z_s dependence in P_t , yields

$$P_r(\tau + \frac{2h}{c}) \approx \frac{\lambda^2 G_o^2 \sigma^o}{(4\pi)^3} \int \frac{P_t(\tau - \frac{\tilde{\rho}^2}{hc} + \frac{2z_s}{c})}{r_o^4} \tilde{\rho} d\tilde{\rho} d\phi. \quad (4)$$

We now take the transmitted pulse to be Gaussian, i.e.,

$$P_t(t) = P_T e^{-\frac{t^2}{2\sigma^2}},$$

then (4) becomes

$$P_r(\tau + \frac{2h}{c}) = \frac{\lambda^2 G_o^2 \sigma^o P_T}{h^4 (4\pi)^3} \int_0^\infty \int_0^{2\pi} e^{-\frac{1}{2\sigma^2} (\tau - \frac{\tilde{\rho}^2}{hc} + \frac{2z_s}{c})^2} \frac{\tilde{\rho} d\tilde{\rho} d\phi}{(1 + \tilde{\rho}^2/h^2)^2} \quad (5)$$

Substituting $\tilde{\rho} = \frac{\rho}{ch}$ in (5) yields

$$P_r(\tau + \frac{2h}{c}) \approx \frac{\lambda^2 G_o^2 \sigma^o P_T c}{2h^3 (4\pi)^3} \int_0^\infty \int_0^{2\pi} \exp \left\{ -\frac{1}{2\sigma^2} (\rho - \tau - 2z_s/c)^2 \right\} d\rho d\phi \quad (6)$$

where we have ignored the factor $(1+c\rho/h)^{-2}$ since it has little effect relative to the Gaussian dependence on ρ . With the change of variables in ρ , z_s becomes

$$z_s = a_s \sin(k_s \sqrt{hc\rho} \cos\phi - \alpha_s).$$

After some trigonometric manipulations, the exponent inside the integral in (6) becomes

$$\begin{aligned} [\rho - \tau - 2z_s/c]^2 &= (\rho - \tau)^2 - \frac{4a_s}{c}(\rho - \tau) \sin(k_s \sqrt{hc\rho} \cos\phi - \alpha_s) \\ &\quad + \frac{2a_s^2}{c} [1 - \cos(2k_s \sqrt{hc\rho} \cos\phi - 2\alpha_s)] \end{aligned} \quad (7)$$

We then use the following identities [6] to remove the last two factors from the exponent:

$$\begin{aligned} \exp \left\{ \frac{2a_s}{c\sigma^2} (\rho - \tau) \sin(\beta \cos\phi - \alpha_s) \right\} &= I_0(x) \\ &+ 2 \sum_{m=0}^{\infty} (-1)^m I_{2m+1}(x) \sin\{(2m+1)(\beta \cos\phi - \alpha_s)\} \\ &+ 2 \sum_{m=1}^{\infty} (-1)^m I_{2m}(x) \cos\{2m(\beta \cos\phi - \alpha_s)\} \end{aligned} \quad (8)$$

and

$$\begin{aligned} \exp \left\{ -\frac{a_s^2}{c^2\sigma^2} + \frac{a_s^2}{c^2\sigma^2} \cos(2\beta \cos\phi - 2\alpha_s) \right\} &= \exp -\left(\frac{a_s}{c\sigma}\right)^2 \left\{ I_0(y) \right. \\ &\quad \left. + 2 \sum_{n=1}^{\infty} I_n(y) \cos\{2n(\beta \cos\phi - \alpha_s)\} \right\} \end{aligned} \quad (9)$$

where

$$\beta = k_s \sqrt{hc\rho}$$

$$x = \frac{2a_s}{c\sigma^2} (\rho - \tau) \quad y = \frac{a_s^2}{c^2\sigma^2}$$

and the $I_n(\cdot)$ are Bessel functions of the second kind and order n . Taking the product of (8) and (9), expanding the trigonometric in series of Bessel functions of the first kind and integrating term by term yields the following:

$$\begin{aligned}
 & \int_0^{2\pi} \exp \left\{ -\frac{1}{2\sigma^2} \left[\rho - \tau - \frac{2z_s}{c} \right]^2 \right\} d\phi = 2\pi e^{-\frac{(\rho-\tau)^2}{2\sigma^2} - \left(\frac{a_s}{c\sigma}\right)^2} \left\{ I_0(x) I_0(y) \right. \\
 & \quad + 2I_0(x) \sum_{n=1}^{\infty} I_n(y) J_0(2n\beta) \cos(2n\alpha_s) \\
 & \quad - 2 \sum_{m=0} \sum_{n=0} (-1)^m I_{2m+1}(x) I_n(y) \delta_{n,o} \left[J_0([2m+1-2n]\beta) \sin([2m+1-2n]\alpha_s) \right. \\
 & \quad \left. + J_0([2m+1+2n]\beta) \sin([2m+1+2n]\alpha_s) \right] \\
 & \quad + 2 \sum_{m=1} \sum_{n=0} (-1)^m I_{2m}(x) I_n(y) \delta_{n,o} \left[J_0([2m-2n]\beta) \cos([2m-2n]\alpha_s) \right. \\
 & \quad \left. + J_0([2m+2n]\beta) \cos([2m+2n]\alpha_s) \right] \left. \right\}
 \end{aligned}$$

where

$$\delta_{n,o} = \begin{cases} 1/2 & n = 0 \\ 1 & n = 1, 2, \dots \end{cases}$$

Rearranging and changing the indices on the various terms in the above leads to the following result;

$$\begin{aligned}
 & \int_0^{2\pi} \exp \left\{ -\frac{1}{2\sigma^2} \left[\rho - \tau - \frac{2z_s}{c} \right]^2 \right\} d\phi = 2\pi e^{-\frac{(\rho-\tau)^2}{2\sigma^2} - \left(\frac{a_s}{c\sigma}\right)^2} \\
 & \quad \cdot \sum_{m=0} \sum_{n=0} I_m(x) I_n(y) \delta_{n,o} \delta_{m,o} \left\{ J_0([m-2n]\beta) \right.
 \end{aligned}$$

$$\begin{aligned}
& \left[\{1+(-1)^m\} \cos \frac{m\pi}{2} \cos([m-2n]\alpha_s) - \{1-(-1)^m\} \cos(m-1)\frac{\pi}{2} \sin([m-2n]\alpha_s) \right] \\
& + J_0([m+2n]\beta) \left\{ \{1+(-1)^m\} \cos \frac{m\pi}{2} \cos([m+2n]\alpha_s) \right. \\
& \left. - [1-(-1)^m] \cos[(m-1)\frac{\pi}{2}] \sin([m+2n]\alpha_s) \right\} \quad (10)
\end{aligned}$$

Equation (10) is the result of integrating (6) with respect to the ϕ -variable; it is exact in that no approximations were employed to obtain (10) from (6). The right hand side of (10) may be simplified considerably when

$$y = \frac{a_s^2}{c^2 \sigma^2} \ll 1,$$

or the pulse length is much larger than the peak amplitude of the sinusoidal undulation. Under this condition we note that

$$I_n(y) \approx \frac{y^n}{2^n \Gamma(n+1)},$$

and we only need to take the first two terms in the I_n series. Thus, the mean return waveform is given by

$$\begin{aligned}
P_r\left(\tau + \frac{2h}{c}\right) & \approx \frac{\lambda^2 G_o^2 \sigma^2 P_T \pi c}{(4\pi)^3 h^3} e^{-\left(\frac{a_s}{c\sigma}\right)^2} \int_0^\infty e^{-\frac{1}{2\sigma^2}[\rho-\tau]^2} \\
& \sum_{m=0}^{\infty} I_m\left(\frac{2a_s}{c\sigma}\right) \delta_{m,0} \left\{ [(-1)^m + 1] \cos \frac{m\pi}{2} [J_0(mk_s \sqrt{hc\rho}) \cos(m\alpha_s) \right. \\
& \quad + \frac{1}{2}\left(\frac{a_s}{c\sigma}\right)^2 \{J_0([m-2]k_s \sqrt{hc\rho}) \cos([m-2]\alpha_s) \\
& \quad + J_0([m+2]k_s \sqrt{hc\rho}) \cos([m+2]\alpha_s)\}] - [1-(-1)^m] \cos \frac{(m-1)\pi}{2} \\
& \quad \cdot [J_0(mk_s \sqrt{hc\rho}) \sin m\alpha_s + \frac{1}{2}\left(\frac{a_s}{c\sigma}\right)^2 \{J_0([m-2]k_s \sqrt{hc\rho}) \sin([m-2]\alpha_s)
\end{aligned}$$

$$+ J_0([m+2]k_s \sqrt{hc\rho}) \sin([m+2]\alpha_s) \Big\} \Big\} d\rho. \quad (11)$$

Equation (11) represents the mean return waveform scattered from a unidirectional sinusoidal surface under the following assumptions:

- (a) pulsewidth limited geometry, and
- (b) the peak amplitude of the surface undulation is small compared to the pulsewidth, i.e., $\frac{a_s}{c} \ll \sigma$.

Expanding the first few terms of (11) yields

$$\begin{aligned} P_r\left(\tau + \frac{2h}{c}\right) &= \frac{\lambda^2 G_o^2 \sigma^2 P_T \pi c}{(4\pi)^3 h^3} e^{-\left(\frac{a_s}{c\sigma}\right)^2} \int_0^\infty e^{-\frac{1}{2\sigma^2}[\rho-\tau]^2} \left\{ I_0\left(\frac{2a_s}{c\sigma^2}[\rho-\tau]\right) \right. \\ &\quad \cdot \left[1 + \left(\frac{a_s}{c\sigma}\right)^2 J_0(2k_s \sqrt{hc\rho}) \cos 2\alpha_s \right] - 2 I_1\left(\frac{2a_s}{c\sigma^2}[\rho-\tau]\right) \\ &\quad \cdot \left[J_0(k_s \sqrt{hc\rho}) \sin \alpha_s + \frac{1}{2} \left(\frac{a_s}{c\sigma}\right)^2 \left\{ -J_0(k_s \sqrt{hc\rho}) \sin \alpha_s + J_0(3k_s \sqrt{hc\rho}) \sin 3\alpha_s \right\} \right] \\ &\quad - 2 I_2\left(\frac{2a_s}{c\sigma^2}[\rho-\tau]\right) \left[J_0(2k_s \sqrt{hc\rho}) \cos 2\alpha_s + \frac{1}{2} \left(\frac{a_s}{c\sigma}\right)^2 \left\{ 1 \right. \right. \\ &\quad \left. \left. + J_0(4k_s \sqrt{hc\rho}) \cos 4\alpha_s \right\} \right] + 2 I_3\left(\frac{2a_s}{c\sigma^2}[\rho-\tau]\right) \left[J_0(3k_s \sqrt{hc\rho}) \sin 3\alpha_s \right. \\ &\quad \left. \left. + \frac{1}{2} \left(\frac{a_s}{c\sigma}\right)^2 \left\{ J_0(k_s \sqrt{hc\rho}) \sin \alpha_s + J_0(5k_s \sqrt{hc\rho}) \sin 5\alpha_s \right\} \right] \right\} + \dots d\rho. \end{aligned} \quad (12)$$

Of all the terms appearing in (12), only the first can be approximately integrated in closed form. For $\frac{a_s}{c} \ll \sigma$, as shown in Appendix B,

$$\int_0^\infty e^{-\frac{1}{2\sigma^2}(\rho-\tau)^2} I_0\left(\frac{2a_s}{c\sigma^2}[\rho-\tau]\right) d\rho \approx \frac{\sqrt{2\pi}\sigma}{2} \left\{ \operatorname{erf}\left(\frac{\tau}{\sigma\sqrt{2}}\right) + e^{\left(\frac{a_s}{c\sigma}\right)^2} I_0\left(\frac{a_s^2}{c^2\sigma^2}\right) \right\}$$

Thus,

$$P_r\left(\tau + \frac{2h}{c}\right) \approx \frac{\lambda^2 G_o^2 \sigma^2 P_T \pi c}{(4\pi)^3 h^3} \left\{ \frac{\sqrt{2\pi}\sigma}{2} \left[e^{-\frac{a_s^2}{c^2\sigma^2}} \operatorname{erf}\left(\frac{\tau}{\sigma\sqrt{2}}\right) + I_0\left(\frac{a_s^2}{c^2\sigma^2}\right) \right] \right\}$$

$$\begin{aligned}
& + e^{-\left(\frac{a_s}{c\sigma}\right)^2} \int_0^\infty e^{-\frac{1}{2\sigma^2}(\rho-\tau)^2} \left[I_0\left(\frac{2a_s}{c\sigma^2}[\rho-\tau]\right) \left(\frac{a_s}{c\sigma}\right)^2 J_0(2k_s \sqrt{hc\rho}) \cos 2\alpha_s \right. \\
& - 2I_1\left(\frac{2a_s}{c\sigma^2}[\rho-\tau]\right) \left\{ J_0(k_s \sqrt{hc\rho}) \sin \alpha_s + \frac{1}{2}\left(\frac{a_s}{c\sigma}\right)^2 \left[-J_0(k_s \sqrt{hc\rho}) \sin \alpha_s \right. \right. \\
& \left. \left. + J_0(3k_s \sqrt{hc\rho}) \sin 3\alpha_s \right] \right\} - 2I_2\left(\frac{2a_s}{c\sigma^2}[\rho-\tau]\right) \left\{ J_0(2k_s \sqrt{hc\rho}) \cos 2\alpha_s \right. \\
& \left. + \frac{1}{2}\left(\frac{a_s}{c\sigma}\right)^2 \left[1 + J_0(4k_s \sqrt{hc\rho}) \cos 4\alpha_s \right] \right\} + 2I_3\left(\frac{2a_s}{c\sigma^2}[\rho-\tau]\right) \left\{ \right. \\
& \left. J_0(3k_s \sqrt{hc\rho}) \sin 3\alpha_s + \frac{1}{2}\left(\frac{a_s}{c\sigma}\right)^2 \left[J_0(k_s \sqrt{hc\rho}) \sin \alpha_s \right. \right. \\
& \left. \left. + J_0(5k_s \sqrt{hc\rho}) \sin 5\alpha_s \right] \right\} + \dots \Big] d\rho \Big\} \quad (13)
\end{aligned}$$

and since

$$e^{-\left(\frac{a_s}{c\sigma}\right)^2} \operatorname{erf}\left(\frac{\tau}{\sigma\sqrt{2}}\right) + I_0\left(\frac{a_s^2}{c^2\sigma^2}\right) \approx \operatorname{erf}\left(\frac{\tau}{\sigma\sqrt{2}}\right) + 1, \quad (14)$$

the first square bracketed term in (13) is essentially the flat-sea mean scattered return. The term in (13) involving $I_2\left(\frac{2a_s}{c\sigma^2}[\rho-\tau]\right)$ which is independent of k_s is a higher order correction to (14) which may be ignored when $a_s/c \ll \sigma$. The remaining terms in (13) depend on k_s and thus exhibit the dependence of the mean return waveform on the surface wave number. Provided $k_s \sqrt{hc}$ is not too large, the dominant term inside the integral in (13) is

$$-2\sin \alpha_s \int_0^\infty e^{-\frac{1}{2\sigma^2}[\rho-\tau]^2} I_1\left(\frac{2a_s}{c\sigma^2}[\rho-\tau]\right) J_0(k_s \sqrt{hc\rho}) d\rho.$$

The exact value of $k_s \sqrt{hc}$ for which the above term no longer dominates the k_s dependent terms in (13) is not analytically obtainable, but may be readily determined by numerical integration of (13).

For a flat sea, the mean return waveform is a convolution of the five following factors:

- (a) transmitted waveform,
- (b) flat sea impulse response,
- (c) radar observed waveheight distribution
- (d) radar receiver impulse response, and
- (e) tracker loop time positioning jitter.

However, for the non-flat sea surface such as we are dealing with in this example, it is not possible to deal with an "undulating sea impulse response" or the analog of (b). That is, if we found the response of the undulating surface to an impulse function, the response to another pulse shape would not be equal to a simple convolution. This can be seen by referring to equation (1). The convolution property arises because for a mean flat sea, $dA = r dr d\phi$ and the ϕ -integration can be accomplished independent of r and the argument of P_t remains as the difference $t - 2r/c$. For the undulating sea $dA \neq r dr d\phi$ and r is a function of both ϕ and $\tilde{\rho}$; thus, after performing the ϕ -integration in (1) the argument of P_t will not necessarily depend on the difference $t - 2r/c$. For this reason, the concept of a "undulating sea impulse response" has no meaning. In fact, the concept of linear scatter theory or the entire multiple convolution model of the process may be questionable; for conditions under which geoidal and ocean surface wave lengths are of comparable length. However, this topic is much beyond the scope of this investigation.

For the purposes of this report, we will assume the following: the system point target response* of the altimeter is Gaussian with a 3dB pulsewidth of T_p ; the radar observed waveheight probability density function is Gaussian with an rms waveheight equal to σ_{ss} and the tracker loop time positioning jitter is a continuous Gaussian process with standard deviation equal to σ_j . If we assume that the significant waveheight of the waves ($H_{1/3}$) is equal to four times the rms waveheight, the pulse width parameter σ is given by

$$\sigma = \sqrt{(.508 H_{1/3})^2 + (.602 T_p)^2 + \sigma_j^2}$$

where $H_{1/3}$ has units of feet and T_p and σ_j have units of nanoseconds. For the GEOS-C altimeter system $\sigma_j \approx 3$ ns. For this study we have chosen a composite

*The point target response of the system is the convolution of (a) and (d), above.

σ of 8.16 ns. Table I shows the combinations of T_p and $H_{1/3}$ which satisfy the above equation with $\sigma = 8.16$ ns and $\sigma_j = 3$ ns. If the system point target response pulsewidth is 12.5 ns then $H_{1/3} = 1.98$ feet which is a small sea.

3.2.3 Determination of the Split-Gate Tracker Response

Equation (13) represents the mean return waveform as influenced by a random scattering surface having a mean sinusoidal profile. In order to determine how the altimeter tracker responds to this return waveform, we must apply the split-gate tracking algorithm to the return. We first normalize $P_r(\tau + \frac{2h}{c})$ such as would be done by the receiver AGC, i.e.,

$$\bar{P}_r(\tau) = \frac{P_r(\tau + 2h/c)}{\Gamma}$$

where

$$\Gamma = \frac{\lambda^2 G_o^2 P_T \sigma^o \pi c}{(4\pi)^3 h^3}$$

We now integrate over the ramp part* of the normalized return to form the function $H_R(k_s, a_s, \alpha_s)$ where

$$H_R(k_s, a_s, \alpha_s) = \int_{-T_p/2}^{T_p/2} \bar{P}_r(\tau) d\tau, \quad (15)$$

TABLE I

Combinations of pulsewidth and significant waveheight which yield $\sigma = 8.16$ ns with $\sigma_j = 3$ ns.

T_p Pulsewidth (ns)	$H_{1/3}$ Significant Waveheight (feet)
8	11.55
10	9.1
12.5	1.98

*For GEOS-C the tracking gates have the same width as the system point target response, i.e., T_p .

while the plateau gate function $H_p(k_s, a_s, \alpha_s)$ is formed by integrating $\bar{P}_r(\tau)$ over the same time interval but starting at a time well into the plateau region of the mean return, i.e.,

$$H_p(k_s, a_s, \alpha_s) = \int_{T-T_p/2}^{T+T_p/2} \bar{P}_r(\tau) d\tau, \quad (16)$$

where $T \gg T_p$.

When $a_s = 0$, the normalized mean return becomes

$$\lim_{a_s \rightarrow 0} \bar{P}_r(\tau) = \frac{\sqrt{2\pi}\sigma}{2} [1 + \operatorname{erf}(\frac{\tau}{\sigma\sqrt{2}})],$$

thus

$$H_R(k_s, a_s = 0, \alpha_s) = \sqrt{2\pi} \sigma \left(\frac{T}{2}\right) \quad (17)$$

and

$$H_p(k_s, a_s = 0, \alpha_s) = \sqrt{2\pi} \sigma T_p \quad (18)$$

Comparing (17) and (18) we see that

$$H_R(k_s, a_s = 0, \alpha_s) = \frac{1}{2} H_p(k_s, a_s = 0, \alpha_s) \quad (19)$$

and, thus, for the mean flat sea, the tracking law is satisfied when the integrated ramp and plateau gate values are defined as in (15) and (16).

In the actual system the altitude tracker develops an error signal for each received pulse, each of which is an ensemble member of the mean power versus time relationship of the backscattered signal. Averaging characteristics of the closed-loop system thus provide a measure of mean signal properties. Since we can only calculate signal statistics - not individual ensemble members - it is necessary to conceptually reverse the order of the altitude measurement and averaging processes. This amounts to an ergodic assumption, which previous Monte Carlo simulation studies have shown to apply. Also, since the altimeter uses a square-law detector, the averaged video signal should correspond to the calculated $\bar{P}_r(t)$ for the noise-free case.

We further assume that the mean return waveform as a function of k_s does not differ appreciably from a shifted replica of the mean flat sea return and,

also, that $2a_s/c \ll \sigma$, i.e., the maximum possible two-way time shift due to the sinusoidal mean surface is small compared to a pulse length. Under these assumptions we can mathematically replace the closed-loop tracking process by a fixed discriminator relationship, i.e.,

$$\epsilon_t = \beta \left[H_R(k_s, a_s, \alpha_s) - \frac{1}{2} H_p(k_s, a_s, \alpha_s) \right] \quad (20)$$

where ϵ_t is the time position error relative to $2h/c$ and we define β such that when $k_s = 0$ ($\lambda_s = \infty$) and $\alpha_s = \pi/2$ or the surface is flat but a_s meters below the $\epsilon_t = 0$ sea surface then $\epsilon_t = 2a_s/c$.

To obtain (20) we note first of all that if T is sufficiently large (as defined in equation (16)) then

$$H_p(k_s, a_s, \alpha_s) \approx H_p(k_s, a_s=0, \alpha_s) = \sqrt{2\pi} \sigma T_p,$$

or changes in the location of the leading edge of the pulse as a function of k_s have no effect on the plateau gate integrated value. Thus, (20) reduces to

$$\epsilon_t = \beta \left[H_R(k_s, a_s, \alpha_s) - \frac{\sqrt{2\pi}}{2} \sigma T_p \right].$$

When $k_s = 0$ and $\alpha_s = \pi/2$, we determine β so that $\epsilon_t = 2a_s/c$, i.e.,

$$\beta = \frac{2a_s/c}{H_R(k_s=0, a_s, \alpha_s=\pi/2) - \frac{\sqrt{2\pi}}{2} \sigma T_p}$$

When $k_s = 0$, the normalized mean return waveform may readily be obtained from equation (6) and

$$\lim_{k_s \rightarrow 0} \bar{P}_r\left(\tau + \frac{2h}{c}\right) = \frac{\sqrt{2\pi}\sigma}{2} \left[1 + \operatorname{erf}\left(\frac{\tau + \frac{2a_s}{c} \sin(-\alpha_s)}{\sigma \sqrt{2}}\right) \right]$$

Integrating $\lim_{k_s \rightarrow 0} \bar{P}_r\left(\tau + \frac{2h}{c}\right)$ between the limits of $-T_p/2$ and $+T_p/2$ and setting $\alpha_s = \pi/2$, we find

$$H_R(k_s=0, a_s, \alpha_s=\pi/2) = \frac{\sigma \sqrt{2\pi}}{2} \left\{ T_p + \left(-\frac{T_p}{2} - \frac{2a_s}{c}\right) \operatorname{erf}\left(\frac{1}{\sigma \sqrt{2}} \left[\frac{T_p}{2} - \frac{2a_s}{c}\right]\right) \right\}$$

$$\begin{aligned}
& - \left(\frac{T_p}{2} + \frac{2a_s}{c} \right) \operatorname{erf} \left(\frac{1}{\sigma\sqrt{2}} \left[\frac{T_p}{2} + \frac{2a_s}{c} \right] \right) + \frac{\sigma\sqrt{2}}{\sqrt{\pi}} e^{-\frac{1}{2\sigma^2} \left(\frac{T_p}{2} + \frac{2a_s}{c} \right)^2} \\
& - \frac{\sigma\sqrt{2}}{\sqrt{\pi}} e^{-\frac{1}{2\sigma^2} \left(\frac{T_p}{2} + \frac{2a_s}{c} \right)^2} \left. \right\} \quad (21)
\end{aligned}$$

Substituting $\sigma = 8.16$ ns, $T_p = 12.5$ ns and $a_s = 0.4$ meter in the above yields

$$H_R(k_s=0, a_s, \alpha_s=\pi/2) - \frac{\sqrt{2\pi}}{2} \sigma T_p = -29.898,$$

and

$$\beta = -29.898.$$

The time shift of the tracking loop is therefore given by

$$\epsilon_t = -\frac{(2a_s/c)}{29.898} \left\{ H_R(k_s, a_s, \alpha_s) - \frac{\sqrt{2\pi}}{2} \sigma T_p \right\} \quad (22)$$

where $H_R(k_s, a_s, \alpha_s)$ is given by (15) with $\bar{P}_r(\tau)$ computed from (13).

The height of a point on the surface directly beneath the altimeter is given by

$$h_A = h - z_s$$

or

$$h_A = h - a_s \sin(k_s \tilde{\rho} \cos \phi - \alpha_s) \quad (23)$$

where h is the height of the altimeter above the mean flat sea. The phase α_s can be put into a one to one correspondence with the spacecraft velocity in the x -direction by the following:

$$\alpha_s = k_s V_x t,$$

where V_x is the spacecraft velocity in the x -direction and t is spacecraft time. Setting $\tilde{\rho}=0$ in (23), results in the following altitude profile encountered by the altimeter as it moves with constant velocity in the x -direction:

$$h_A = h + a_s \sin \alpha_s \quad (24)$$

or

$$h_A = h + a_s \sin(k_s V_x t).$$

From (24), we see that the time displacement, ϵ_t , of the tracker should be proportional to the sine of the surface phase angle. As noted previously, for relatively small values of $k_s \sqrt{hc}$ such will be the case; however, when $k_s \sqrt{hc}$ becomes large, the dependence of ϵ_t on α_s is no longer sinusoidal.

To demonstrate the sinusoidal behavior, we return to equation (13) and compute the AGC'd mean return in the limit of $k_s \rightarrow 0$. The details of the integrations are given in Appendix B and

$$\begin{aligned} \lim_{k_s \rightarrow 0} \bar{P}_r(\tau + \frac{2h}{c}) &\approx \frac{\sqrt{2\pi} \sigma}{2} \left\{ \operatorname{erf}\left(\frac{\tau}{\sigma \sqrt{2}}\right) + 1 \right\} + \frac{\sqrt{2\pi}}{2} \frac{a_s^2}{c^2 \sigma} \cos 2\alpha_s \left\{ 1 + \operatorname{erf}\left(\frac{\tau}{\sigma \sqrt{2}}\right) \right\} \\ &\quad - 2 \left(\frac{a_s}{c}\right) \left[1 - \frac{q_r}{\sigma \sqrt{2}} \left\{ 1 - e^{-\left(\frac{\tau}{\sigma \sqrt{2}}\right)^2} \right\} \right] \left[\sin \alpha_s + \frac{1}{2} \left(\frac{a_s}{c\sigma}\right)^2 \left\{ -\sin \alpha_s \right. \right. \\ &\quad \left. \left. + \sin 3\alpha_s \right\} \right] - \frac{a_s^2 \sqrt{2\pi}}{2c^2 \sigma} \left[1 + \frac{1}{\sigma \sqrt{2}} \left\{ 1 + \operatorname{erf}\left(\frac{\tau}{\sigma \sqrt{2}}\right) - \frac{4\tau}{\sqrt{\pi}} e^{-\left(\frac{\tau}{\sqrt{2}\sigma}\right)^2} \right\} \right] \\ &\quad \cdot \left[\cos 2\alpha_s + \frac{1}{2} \left(\frac{a_s}{c\sigma}\right)^2 (1 + \cos 4\alpha_s) \right] + \dots \end{aligned}$$

and

$$\begin{aligned} \int_{-\frac{T_p}{2}}^{\frac{T_p}{2}} \lim_{k_s \rightarrow 0} \bar{P}_r(\tau + \frac{2h}{c}) d\tau &= \frac{\sqrt{2\pi} \sigma}{2} (T_p) + \frac{\sqrt{2\pi}}{2} \frac{a_s^2}{c^2 \sigma} \cos 2\alpha_s (T_p) \\ &\quad - 2 \left(\frac{a_s}{c}\right) (T_p) \left[\sin \alpha_s + \frac{1}{2} \left(\frac{a_s}{c\sigma}\right)^2 \left\{ -\sin \alpha_s + \sin 3\alpha_s \right\} \right] \\ &\quad - \frac{a_s^2 \sqrt{2\pi}}{2c^2 \sigma} (T_p) \left[\cos 2\alpha_s + \frac{1}{2} \left(\frac{a_s}{c\sigma}\right)^2 (1 + \cos 4\alpha_s) \right] + \dots, \end{aligned}$$

therefore the tracker loop time positioning becomes

$$\lim_{k_s \rightarrow 0} \epsilon_t = - \frac{(2a_s/c)}{29.898} T_p \left\{ \frac{\sqrt{2\pi}}{2} \frac{a_s^2}{c^2 \sigma} \cos 2\alpha_s - 2 \left(\frac{a_s}{c}\right) \left[\sin \alpha_s \right. \right.$$

$$+ \frac{1}{2} \left(\frac{a_s}{c\sigma} \right)^2 \left\{ -\sin \alpha_s + \sin 3\alpha_s \right\} \left[-\frac{a_s^2 \sqrt{2\pi}}{2c^2 \sigma} \left[\cos 2\alpha_s \right. \right. \\ \left. \left. + \frac{1}{2} \left(\frac{a_s}{c\sigma} \right)^2 (1 + \cos 4\alpha_s) \right] + \dots \right\}.$$

Substituting $\sigma = 8.16$ ns, $a_s = 0.4$ meter yields

$$\lim_{k_s \rightarrow 0} \epsilon_t = -\frac{(2a_s/c)}{29.898} T_p \left\{ .273 \cos 2\alpha_s - 2.67[\sin \alpha_s + (.013)(-\sin \alpha_s \right. \\ \left. + \sin 3\alpha_s)] - .273[\cos 2\alpha_s + (.013)(1 + \cos 4\alpha_s)] + \dots \right\} \quad (25)$$

or

$$\lim_{k_s \rightarrow 0} \epsilon_t \approx (1.11) \left(\frac{2a_s}{c} \right) \sin \alpha_s. \quad (26)$$

The factor (1.11) is due to the fact that the integration of (13) as shown in Appendix B is approximate while the denominator in (25), i.e., 29.898, was exact (see equation (21)). The important point to note in (26) is that the tracker loop time positioning is proportional to $\sin \alpha_s$.

When k_s is not equal to zero, it is not an easy task to demonstrate the dependence of ϵ_t on $\sin \alpha_s$. Because of the complexity of the integrand in (13), it is not possible to analytically obtain the value of k_s for which the terms multiplying $\sin \alpha_s$ are dominant. That is, we would like to find the value of k_s such that for $k_s \leq \bar{k}_s$

$$\bar{P}_r(\tau + \frac{2h}{c}) \approx \frac{\sqrt{2\pi} \sigma}{2} \left[e^{-\left(\frac{a_s}{c\sigma}\right)^2} \operatorname{erf}\left(\frac{\tau}{\sigma\sqrt{2}}\right) + I_0\left(\frac{a_s^2}{c^2 \sigma^2}\right) \right] \\ - 2 \sin \alpha_s e^{-\left(\frac{a_s}{c\sigma}\right)^2} \int_0^\infty I_1\left(\frac{2a_s}{c\sigma^2}[\rho-\tau]\right) J_0(k_s \sqrt{hc\rho}) \left[1 - \frac{1}{2} \left(\frac{a_s}{c\sigma} \right)^2 \right] e^{-\frac{(\rho-\tau)^2}{2\sigma^2}} d\rho \quad (27)$$

and for ϵ_t we then have

$$\epsilon_t \approx + \frac{(2a_s/c)}{29.898} \left\{ 2 \sin \alpha_s e^{-\left(\frac{a_s}{c\sigma}\right)^2} \int_{-\frac{T_p}{2}}^{\frac{T_p}{2}} \int_0^\infty I_1\left(\frac{2a_s}{c\sigma^2}[\rho-\tau]\right) J_0(k_s \sqrt{hc\rho}) \right.$$

$$\cdot \left[1 - \frac{1}{2} \left(\frac{a_s}{c\sigma} \right)^2 \right] e^{-\frac{(\rho-\tau)^2}{2\sigma^2}} d\rho d\tau \Bigg\} . \quad (28)$$

Equation (28) can be rewritten in the following form:

$$\epsilon_t = \left(\frac{2a_s}{c} \right) A(k_s) \sin \alpha_s$$

where $A(k_s)$ has a maximum value of one when $k_s = 0$ and it determines the dependence of ϵ_t on k_s . Because of the J_0 function in (28), $A(k_s)$ will go to zero for certain values of k_s and as k_s increases beyond this value, $A(k_s)$ will change sign. A change in the sign of $A(k_s)$ indicates that while the altimeter may be profiling the gross variation of the surface, i.e., $\sin \alpha_s$, properly, it is interpreting peaks and valleys in the surface as valleys and peaks, respectively. With the limited amount of computation that we have accomplished on this problem, we have found that (28) is a reasonable approximation to (22) for k_s slightly less than that value for which $A(k_s)$ goes to zero for the second time. For values of k_s beyond this point, the variation of ϵ_t with surface phase is no longer sinusoidal since other α_s dependent terms in (13) become dominant. However, for spatial wave lengths at which (28) becomes invalid, an absurd noise level for altimeter observations would be required to permit compensation of spatial filter effects.

3.2.4 Results for GEOS-C Intensive Mode of Operation

Much of the preceding material has been concerned with the spatial filter problem in general. In particular we have attempted to show how the sinusoidal surface affects the mean return waveform and how this effect may be translated into the profiling capability of the altimeter's tracking loop. We have also pointed out some of the simplifying assumptions that can be made in dealing with the rather complicated form of the mean return waveform. We will now address the GEOS-C problem. As before we will assume a 3 dB pulse width (T_p) of 12.5 ns for the system point target response, a significant waveheight of 1.98 feet and a tracking loop jitter standard deviation of 3 ns. The orbiting altitude of the altimeter will be taken as 880 km, while both the ramp and plateau tracking gates will be assumed to be 12.5 ns wide. The system parameters assumed represent our present knowledge of the expected final configuration of GEOS-C in the Intensive Mode while the altitude and waveheight parameters are taken to be nominal operating conditions.

For the parameters listed above, we have computed the mean return waveform by numerically integrating equation (12) including all terms out to $I_6(2a_s[\rho-\tau]/c\sigma^2)$. All computations were for a peak surface amplitude of 0.4 m. The resulting waveforms were integrated over the time interval $-\frac{T_p}{2} \leq \tau \leq \frac{T_p}{2}$ and the output of the tracking loop time discriminator was computed using (22). A plot of ϵ_t , normalized by $2a_s/c$ and as a function of surface wave number and wavelength is shown in Figure 3.6. This plot illustrates the extent to which the profiling ability of the altimeter degrades as the wavelength of the surface undulation decreases. Due to sea-state and jitter effects, the equivalent 3 dB pulse width of the system increases from 12.5 ns to 13.55 ns. The approximate cutoff wavelength of such a system is given by

$$\lambda_c = 2\sqrt{hc(13.55)}$$

or $\lambda_c = 3.78$ km. As shown in Figure 3.6, λ_c is slightly smaller than the first zero in ϵ_t . As λ_s decreases beyond the point for which $\epsilon_t = 0$, ϵ_t changes sign. That is, the altimeter indicates the presence of a valley in the surface when it is actually measuring a peak. Near the second zero of ϵ_t , the altimeter profiling capability entirely breaks down because the altimeter no longer sees a sinusoidal surface. Thus, for $\lambda_s \leq 2$ km the altimeter is no longer profiling the surface. Such an observation can not be made by just examining Figure 3.6; this statement requires that the variation of ϵ_t with surface phase, α_s , be examined and compared with the $\sin\alpha_s$. Thus, the plot in Figure 3.6 should be "cutoff" at $\lambda_s = 2$ km.

While Figure 3.6 is the desired output of this study, it is also interesting to examine how the mean return varies as a function of surface wavelength. The solid line in Figure 3.7 is that portion of the normalized return for a mean flat sea surface, i.e., $a_s = 0$. The dashed curve for $\lambda_s = 31.4$ km is essentially a shifted replica of the flat sea curve. It is shifted to the right (later in time) because the nadir point on the surface is a "valley" in the sinusoidal mean surface, i.e., $a_s \sin(-\alpha_s) = -a_s$. As the wavelength of the undulating surface decreases, the mean return shifts closer to the flat sea curve and also begins to change shape. The curve in Figure 3.7 for $\lambda_s = 6.98$ km corresponds to the -5.5 dB point on the ϵ_t versus λ_s curve in Figure 3. Figure 3.8 illustrates how returns from surfaces having $\lambda_s = 4.49$ km and 2.73 km compare with the flat

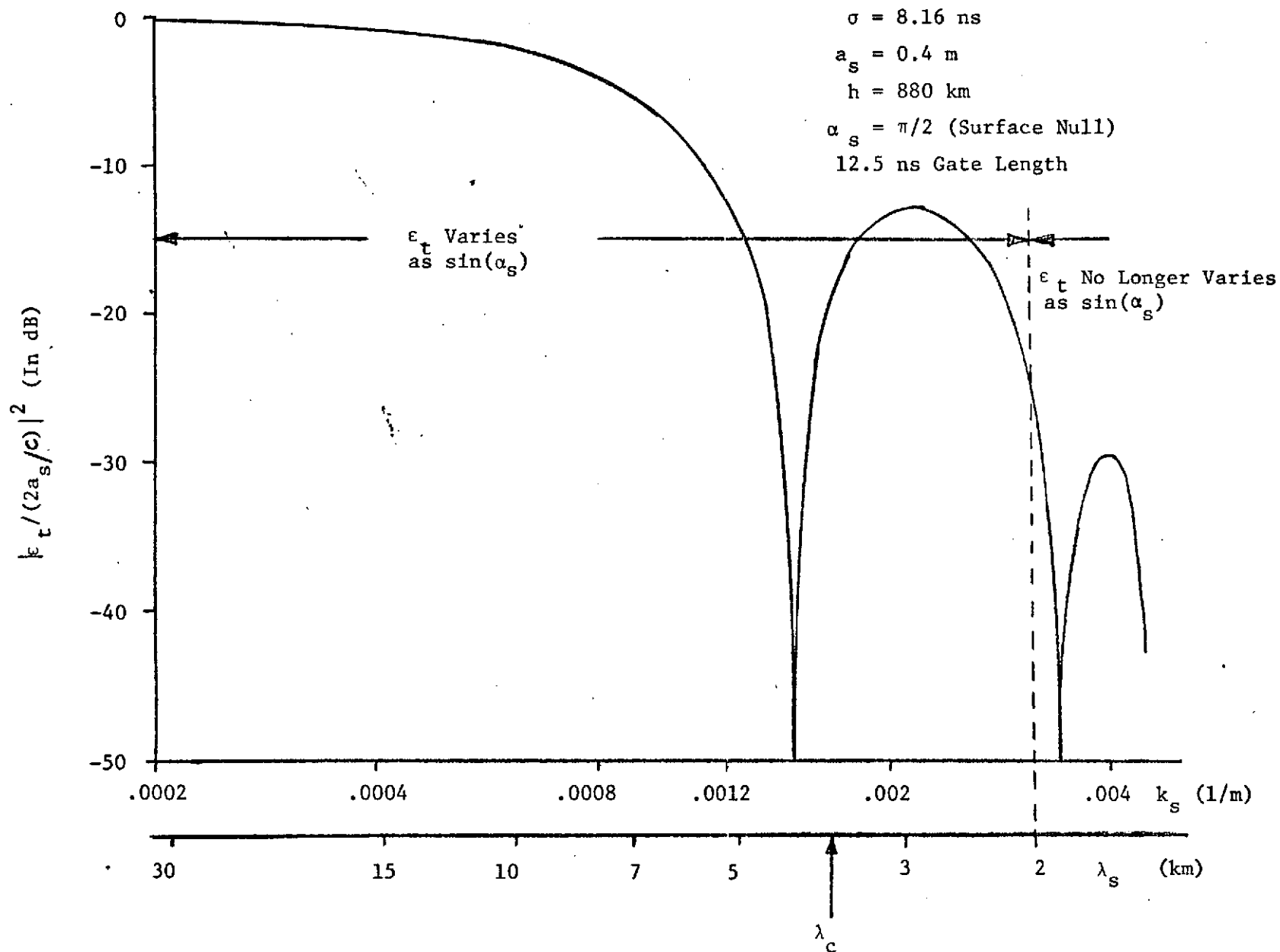


Fig. 3.6 A Plot of the Altimeter Tracker Response to a Sinusoidal Surface as the Wavelength of the Surface Varies.

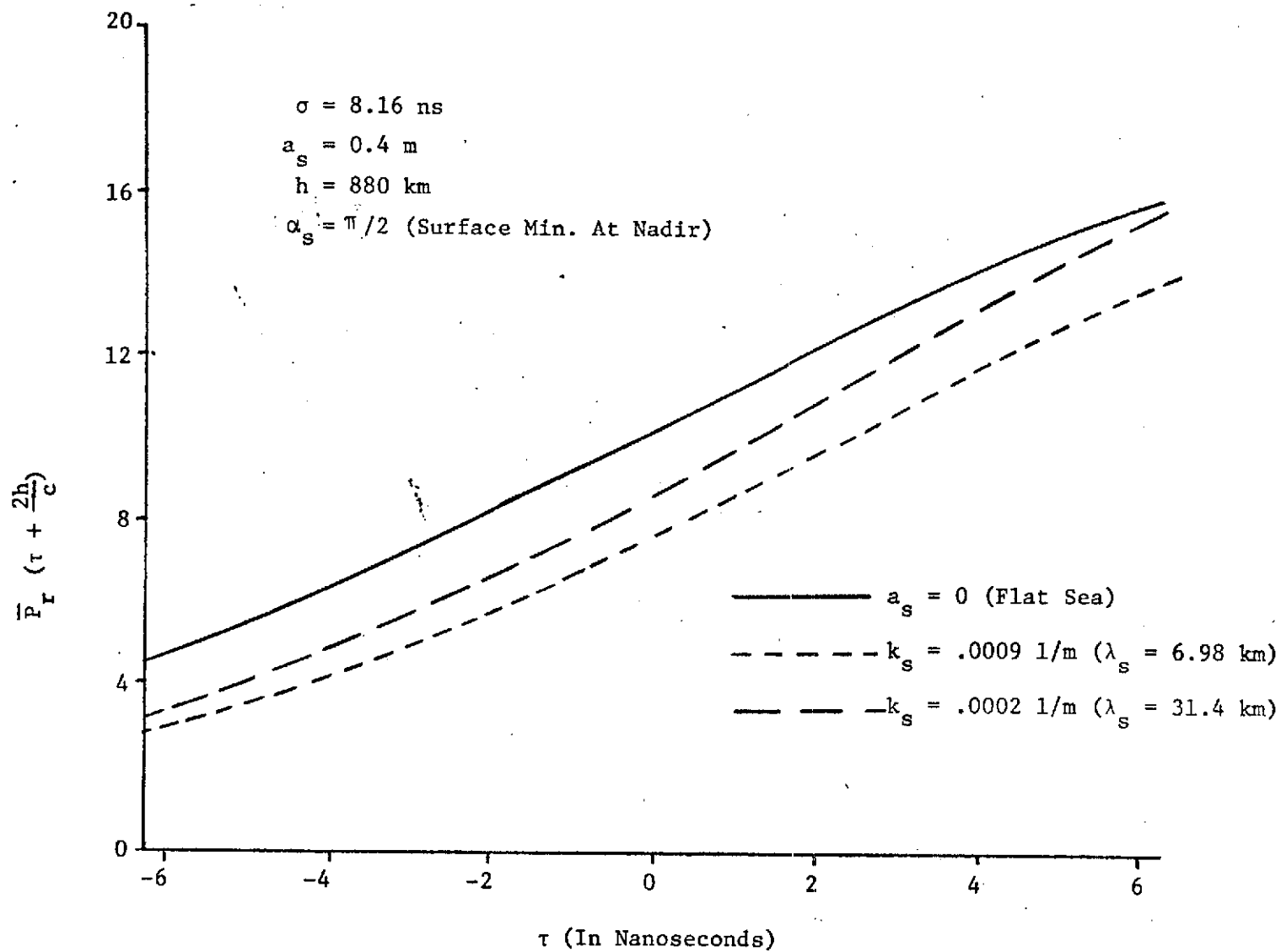


Fig. 3.7 Mean Return Waveforms Within the Ramp Gate Interval for a Flat Sea, $\lambda_s = 31.4 \text{ km}$ and $\lambda_s = 6.98 \text{ km}$.

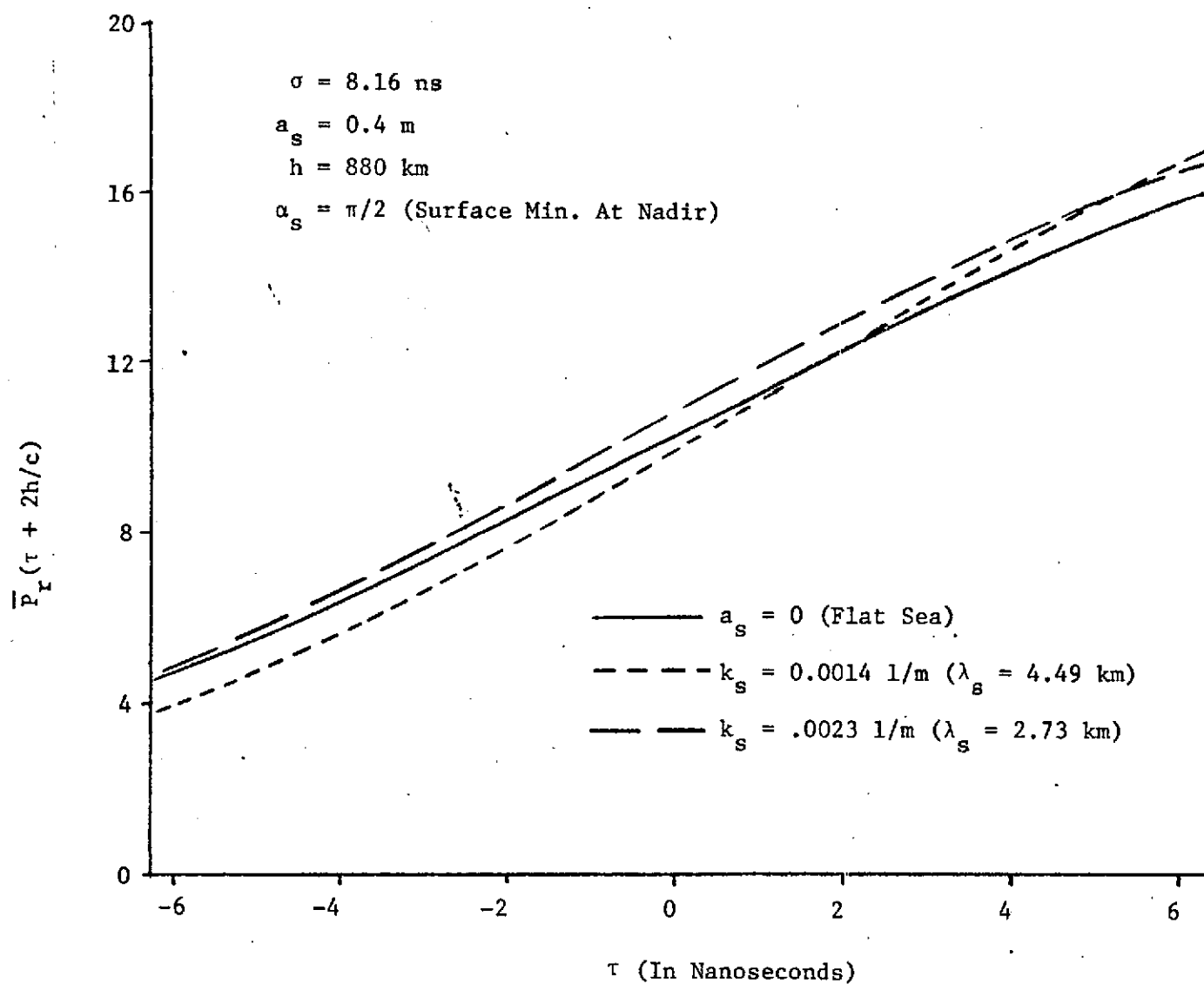


Fig. 3.8 Mean Return Waveforms Within the Ramp Gate Interval for a Flat Sea, $\lambda_s = 4.49 \text{ km}$ and $\lambda_s = 2.73 \text{ km}$.

sea return. For the 4.49 km return, the portion nearest the plateau region actually appears earlier in time than the flat sea. For $k_s = 2.73$ km, the entire portion of the return shown in Figure 3.8 appears earlier in time than the flat sea return, thus giving the appearance of having been scattered from an elevated surface. This character of the return, of course, gives rise to the sign reversal in ϵ_t , i.e., the altimeter interprets peaks in the surface as valleys.

References

1. Cohen, C. J. and B. Zondek, "Accuracy of Deflection of the Vertical Derived from Satellite Altimetry," NWL Technical Report TR-2626, October 1971.
2. Brown, R. D. and S. Vincent, "Power Spectra of Geoid Undulations," Presentation at the December 1972 AGU Meeting, San Francisco.
3. Davenport W. and W. Root, Random Signals and Noise, McGraw Hill, 1958.
4. Miller, L. S., G. S. Brown and G. S. Hayne, "Engineering Studies Related to Geodetic and Oceanographic Remote Sensing Using Short Pulse Techniques," Final Report, Contract No. NAS6-2135, Research Triangle Institute, Durham, North Carolina, February 1973.
5. Moore, R. K. and C. S. Williams, Jr., "Radar Terrain Return at Near Vertical Incidence," Proc. of I.R.E., Vol. 45, pp. 228-238, February 1957.
6. Abramowitz, M. and I. A. Stegun (Editors), Handbook of Mathematical Functions, NBS Applied Math Series, Vol. 55, U.S.G.P.O., pp. 376, June 1964.

Appendix A

This Appendix contains a tabulation of weighting coefficients for the optimum undulation and slope extraction filters. The "T" column is incremented by 0.1 seconds corresponding to the output altitude data rate. The "H" column is a list of the corresponding weights for extracting geoidal undulation data. The "DHDT" column is a list of the weights for extracting geoidal slope data. As discussed in section 3.1, both columns of weights should be renormalized based on the truncation point selected for the data processing.

T=	0.00,	H=	1.0000	,	DHDT=	0.00000
T=	0.10,	H=	0.98854	,	DHDT=	-0.22181
T=	0.20,	H=	0.95694	,	DHDT=	-0.40306
T=	0.30,	H=	0.90915	,	DHDT=	-0.54624
T=	0.40,	H=	0.84883	,	DHDT=	-0.65428
T=	0.50,	H=	0.77932	,	DHDT=	-0.73042
T=	0.60,	H=	0.70366	,	DHDT=	-0.77810
T=	0.70,	H=	0.62451	,	DHDT=	-0.80082
T=	0.80,	H=	0.54420	,	DHDT=	-0.80209
T=	0.90,	H=	0.46468	,	DHDT=	-0.78533
T=	1.00,	H=	0.38761	,	DHDT=	-0.75380
T=	1.10,	H=	0.31431	,	DHDT=	-0.71053
T=	1.20,	H=	0.24579	,	DHDT=	-0.65851
T=	1.30,	H=	0.18281	,	DHDT=	-0.60017
T=	1.40,	H=	0.12589	,	DHDT=	-0.53785
T=	1.50,	H=	0.75310D-01,	DHDT=	-0.47359	
T=	1.60,	H=	0.31182D-01,	DHDT=	-0.40913	
T=	1.70,	H=	-0.65511D-02,	DHDT=	-0.34592	
T=	1.80,	H=	-0.38078D-01,	DHDT=	-0.28518	
T=	1.90,	H=	-0.63694D-01,	DHDT=	-0.22786	
T=	2.00,	H=	-0.83780D-01,	DHDT=	-0.17468	
T=	2.10,	H=	-0.98777D-01,	DHDT=	-0.12615	
T=	2.20,	H=	-0.10917	,	DHDT=	-0.82623D-01
T=	2.30,	H=	-0.11547	,	DHDT=	-0.44247D-01
T=	2.40,	H=	-0.11818	,	DHDT=	-0.11052D-01
T=	2.50,	H=	-0.11784	,	DHDT=	0.17057D-01
T=	2.60,	H=	-0.11493	,	DHDT=	0.40272D-01
T=	2.70,	H=	-0.10993	,	DHDT=	0.58862D-01
T=	2.80,	H=	-0.10330	,	DHDT=	0.73158D-01
T=	2.90,	H=	-0.95429D-01,	DHDT=	0.83532D-01	
T=	3.00,	H=	-0.86704D-01,	DHDT=	0.90382D-01	
T=	3.10,	H=	-0.77453D-01,	DHDT=	0.94124D-01	
T=	3.20,	H=	-0.67966D-01,	DHDT=	0.95171D-01	
T=	3.30,	H=	-0.58493D-01,	DHDT=	0.93936D-01	
T=	3.40,	H=	-0.49241D-01,	DHDT=	0.90810D-01	
T=	3.50,	H=	-0.40380D-01,	DHDT=	0.86168D-01	
T=	3.60,	H=	-0.32046D-01,	DHDT=	0.80357D-01	
T=	3.70,	H=	-0.24337D-01,	DHDT=	0.73692D-01	
T=	3.80,	H=	-0.17326D-01,	DHDT=	0.66460D-01	
T=	3.90,	H=	-0.11056D-01,	DHDT=	0.58913D-01	
T=	4.00,	H=	-0.55475D-02,	DHDT=	0.51268D-01	
T=	4.10,	H=	-0.80030D-03,	DHDT=	0.43711D-01	
T=	4.20,	H=	0.32021D-02,	DHDT=	0.36397D-01	
T=	4.30,	H=	0.64905D-02,	DHDT=	0.29449D-01	
T=	4.40,	H=	0.91064D-02,	DHDT=	0.22962D-01	
T=	4.50,	H=	0.11100D-01,	DHDT=	0.17006D-01	
T=	4.60,	H=	0.12526D-01,	DHDT=	0.11630D-01	
T=	4.70,	H=	0.13445D-01,	DHDT=	0.68580D-02	
T=	4.80,	H=	0.13917D-01,	DHDT=	0.27003D-02	
T=	4.90,	H=	0.14004D-01,	DHDT=	-0.84949D-03	
T=	5.00,	H=	0.13766D-01,	DHDT=	-0.38102D-02	
T=	5.10,	H=	0.13260D-01,	DHDT=	-0.62107D-02	
T=	5.20,	H=	0.12541D-01,	DHDT=	-0.80876D-02	
T=	5.30,	H=	0.11658D-01,	DHDT=	-0.94832D-02	
T=	5.40,	H=	0.10658D-01,	DHDT=	-0.10444D-01	
T=	5.50,	H=	0.95822D-02,	DHDT=	-0.11018D-01	
T=	5.60,	H=	0.84658D-02,	DHDT=	-0.11255D-01	
T=	5.70,	H=	0.73405D-02,	DHDT=	-0.11204D-01	
T=	5.80,	H=	0.62329D-02,	DHDT=	-0.10912D-01	

T=	5.90,	H=	0.51646D-02,	DHDT=	-0.10424D-01
T=	6.00,	H=	0.41531D-02,	DHDT=	-0.97831D-02
T=	6.10,	H=	0.32117D-02,	DHDT=	-0.90275D-02
T=	6.20,	H=	0.23502D-02,	DHDT=	-0.81927D-02
T=	6.30,	H=	0.15748D-02,	DHDT=	-0.73098D-02
T=	6.40,	H=	0.88898D-03,	DHDT=	-0.64063D-02
T=	6.50,	H=	0.29355D-03,	DHDT=	-0.55055D-02
T=	6.60,	H=	-0.21277D-03,	DHDT=	-0.46270D-02
T=	6.70,	H=	-0.63303D-03,	DHDT=	-0.37868D-02
T=	6.80,	H=	-0.97172D-03,	DHDT=	-0.29973D-02
T=	6.90,	H=	-0.12344D-02,	DHDT=	-0.22681D-02
T=	7.00,	H=	-0.14274D-02,	DHDT=	-0.16055D-02
T=	7.10,	H=	-0.15578D-02,	DHDT=	-0.10137D-02
T=	7.20,	H=	-0.16325D-02,	DHDT=	-0.49446D-03
T=	7.30,	H=	-0.16590D-02,	DHDT=	-0.47607D-04
T=	7.40,	H=	-0.16443D-02,	DHDT=	0.32853D-03
T=	7.50,	H=	-0.15954D-02,	DHDT=	0.63695D-03
T=	7.60,	H=	-0.15190D-02,	DHDT=	0.88167D-03
T=	7.70,	H=	-0.14210D-02,	DHDT=	0.10675D-02
T=	7.80,	H=	-0.13072D-02,	DHDT=	0.11997D-02
T=	7.90,	H=	-0.11826D-02,	DHDT=	0.12840D-02
T=	8.00,	H=	-0.10518D-02,	DHDT=	0.13263D-02
T=	8.10,	H=	-0.91853D-03,	DHDT=	0.13323D-02
T=	8.20,	H=	-0.78629D-03,	DHDT=	0.13077D-02
T=	8.30,	H=	-0.65782D-03,	DHDT=	0.12580D-02
T=	8.40,	H=	-0.53536D-03,	DHDT=	0.11883D-02
T=	8.50,	H=	-0.42067D-03,	DHDT=	0.11034D-02
T=	8.60,	H=	-0.31505D-03,	DHDT=	0.10076D-02
T=	8.70,	H=	-0.21939D-03,	DHDT=	0.90475D-03
T=	8.80,	H=	-0.13422D-03,	DHDT=	0.79835D-03
T=	8.90,	H=	-0.59752D-04,	DHDT=	0.69129D-03
T=	9.00,	H=	0.40855D-05,	DHDT=	0.58606D-03

Appendix B

In the course of the analysis presented in section 3.2, it will be necessary to evaluate integrals of the form

$$I = \int_0^{\infty} e^{-\frac{1}{2\sigma^2}(\rho-\tau)^2} I_n\left(\frac{2a_s}{c\sigma^2}[\rho-\tau]\right) d\rho \quad (B1)$$

The purpose of this Appendix is to demonstrate how these integrals may be evaluated. First, we substitute $\eta = \rho - \tau$ in (B1), then

$$I = \int_{-\tau}^{\infty} e^{-\frac{\eta^2}{2\sigma^2}} I_n\left(\frac{2a_s}{c\sigma^2} \eta\right) d\eta$$

which can be split into two integrals, i.e.

$$I = \int_0^{\infty} e^{-\frac{\eta^2}{2\sigma^2}} I_n\left(\frac{2a_s}{c\sigma^2} \eta\right) d\eta + \int_{-\tau}^0 e^{-\frac{\eta^2}{2\sigma^2}} I_n\left(\frac{2a_s}{c\sigma^2} \eta\right) d\eta \quad (B2)$$

The first integral can be found in standard references on integrals of Bessel functions and

$$\int_0^{\infty} e^{-\frac{\eta^2}{2\sigma^2}} I_n\left(\frac{2a_s}{c\sigma^2} \eta\right) d\eta = \frac{\sqrt{2\pi} \sigma}{2} e^{\left(\frac{a_s}{c\sigma}\right)^2} I_{n/2}\left(\frac{a_s^2}{c^2\sigma^2}\right) \quad (B3)$$

For the second integral in (B2), we will only be concerned with that portion of the return for which $|\tau| \leq T_{s/2}^*$, thus

$$\frac{2a_s}{c\sigma^2} |\eta| \leq \frac{2a_s}{c\sigma^2} \left(T_{s/2}\right).$$

Because of jitter and sea-state effects, the 3dB pulsewidth of the system

* T_s is defined as the 3 dB width of the system point target response.

point target response will always be less than or equal to 1.67σ , thus

$$\frac{2a_s}{c\sigma^2} |\eta| \leq \frac{a_s}{c\sigma^2} (1.67\sigma) = \frac{1.67a_s}{c\sigma}$$

For the case to be considered here, $a_s = 0.4\text{m}$ and $\sigma = 8.16\text{ns}$, thus

$$\frac{2a_s}{c\sigma^2} |\eta| \leq 0.272$$

Therefore, for the second integral in (B2) we may use the small argument

approximation for $I_n \left(\frac{2a_s \eta}{c\sigma^2} \right)$ or

$$I_n \left(\frac{2a_s}{c\sigma^2} \eta \right) \approx \frac{\left(\frac{2a_s}{c\sigma^2} |\eta| \right)^n}{2^n \Gamma(n+1)} \quad |\eta| \leq \frac{T_p}{2}$$

Therefore, for $\tau \leq 0$

$$\int_{-\tau}^0 e^{-\frac{\eta^2}{2\sigma^2}} I_n \left(\frac{2a_s}{c\sigma^2} \eta \right) d\eta \approx \frac{\left(\frac{2a_s}{c\sigma^2} \right)^n}{2^n \Gamma(n+1)} \int_{-\tau}^0 e^{-\frac{\eta^2}{2\sigma^2}} \eta^n d\eta$$

while for $\tau \geq 0$

$$\int_{-\tau}^0 e^{-\frac{\eta^2}{2\sigma^2}} I_n \left(\frac{2a_s}{c\sigma^2} \eta \right) d\eta \approx \frac{\left(\frac{2a_s}{c\sigma^2} \right)^n}{2^n \Gamma(n+1)} (-1)^n \int_{-\tau}^0 e^{-\frac{\eta^2}{2\sigma^2}} \eta^n d\eta$$

The above integral can be evaluated by noting that

$$\int_{-\tau}^0 e^{-a^2 \eta^2} \eta^n d\eta = \lim_{b \rightarrow 0} \left\{ \frac{1}{(-2)^n} \frac{d^n}{db^n} \int_{-\tau}^0 e^{-a^2 \eta^2 - 2b\eta} d\eta \right\}$$

$$= \lim_{b \rightarrow 0} \left\{ \frac{\sqrt{\pi}}{(-2)^n 2\sqrt{a}} \frac{d^n}{db^n} \left[e^{\frac{b^2}{a}} \operatorname{erf} \left(\sqrt{a} \eta + \frac{b}{\sqrt{a}} \right) \right] \right\}_{-\tau}^0$$

Thus,

$$\begin{aligned} \int_{-\tau}^0 e^{-\frac{\eta^2}{2\sigma^2}} d\eta &= \frac{\sqrt{2\pi} \sigma}{2} \operatorname{erf} \left(\frac{\tau}{\sigma\sqrt{2}} \right) \\ \int_{-\tau}^0 \eta e^{-\frac{\eta^2}{2\sigma^2}} d\eta &= -\frac{\sqrt{2}}{2} \sigma \left[1 + e^{-\left(\frac{\tau}{\sigma\sqrt{2}}\right)^2} \right] \\ \int_{-\tau}^0 \eta^2 e^{-\frac{\eta^2}{2\sigma^2}} d\eta &= \frac{2\sqrt{\pi} \sigma^2}{4} \left[1 + \operatorname{erf} \left(\frac{\tau}{\sigma\sqrt{2}} \right) - \frac{4\tau}{\sqrt{\pi}} e^{-\left(\frac{\tau}{\sigma\sqrt{2}}\right)^2} \right] \end{aligned}$$

and

$$\int_{-\tau}^0 e^{-\frac{\eta^2}{2\sigma^2}} I_0 \left(\frac{2a_s}{c\sigma^2} \eta \right) d\eta \approx \frac{\sqrt{2\pi} \sigma}{2} \operatorname{erf} \left(\frac{\tau}{\sigma\sqrt{2}} \right) \quad (B4)$$

$$\int_{-\tau}^0 e^{-\frac{\eta^2}{2\sigma^2}} I_1 \left(\frac{2a_s}{c\sigma^2} \eta \right) d\eta \approx -q_\tau \frac{\sqrt{2} a_s}{2c\sigma} \left[1 - e^{-\left(\frac{\tau}{\sigma\sqrt{2}}\right)^2} \right] \quad (B5)$$

$$\int_{-\tau}^0 e^{-\frac{\eta^2}{2\sigma^2}} I_2 \left(\frac{2a_s}{c\sigma^2} \eta \right) d\eta \approx \frac{\sqrt{\pi} a_s^2}{4c^2 \sigma^2} \left[1 + \operatorname{erf} \left(\frac{\tau}{\sigma\sqrt{2}} \right) - \frac{4\tau}{\sqrt{\pi}} e^{-\left(\frac{\tau}{\sigma\sqrt{2}}\right)^2} \right] \quad (B6)$$

where

$$q_\tau = \begin{cases} 1 & \tau \geq 0 \\ -1 & \tau < 0 \end{cases}$$

If we also use the fact that $(\frac{a_s}{c\sigma})^2 \ll 1$, then

$$I_0 \left(\frac{a_s^2}{c^2 \sigma^2} \right) \approx 1$$

$$I_{\frac{1}{2}} \left(\frac{a_s^2}{c^2 \sigma^2} \right) \approx \frac{2 \left(\frac{a_s}{c \sigma \sqrt{2}} \right)}{\sqrt{\pi}}$$

$$I_1 \left(\frac{a_s^2}{2c^2 \sigma^2} \right) \approx \frac{a_s^2}{2c^2 \sigma^2}$$

and substituting the above in (B3) and using (B4), (B5) and (B6), we have

$$\int_0^\infty e^{-\frac{1}{2\sigma^2}(\rho-\tau)^2} I_0 \left(\frac{2a_s}{c\sigma^2} [\rho-\tau] \right) d\rho \approx \frac{\sqrt{2\pi} \sigma}{2} \left[e^{\left(\frac{a_s}{c\sigma} \right)^2} + \operatorname{erf} \left(\frac{\tau}{\sigma\sqrt{2}} \right) \right]$$

$$\begin{aligned} \int_0^\infty e^{-\frac{1}{2\sigma^2}(\rho-\tau)^2} I_1 \left(\frac{2a_s}{c\sigma^2} [\rho-\tau] \right) d\rho &\approx \frac{\sqrt{2\pi} \sigma}{2} e^{\left(\frac{a_s}{c\sigma} \right)^2} \left[\frac{2a_s}{c\sigma\sqrt{2\pi}} \right] \\ &- q_\tau \frac{a_s}{c\sigma\sqrt{2}} \left[1 - e^{-\left(\frac{\tau}{\sigma\sqrt{2}} \right)^2} \right] \end{aligned}$$

$$\begin{aligned} \int_0^\infty e^{-\frac{1}{2\sigma^2}(\rho-\tau)^2} I_2 \left(\frac{2a_s}{c\sigma^2} [\rho-\tau] \right) d\rho &\approx \frac{\sqrt{2\pi} \sigma}{2} e^{\left(\frac{a_s}{c\sigma} \right)^2} \left[\frac{a_s^2}{2c^2 \sigma^2} \right] \\ &+ \frac{\sqrt{\pi} a_s^2}{4c^2 \sigma^2} \left[1 + \operatorname{erf} \left(\frac{\tau}{\sigma\sqrt{2}} \right) - \frac{4\tau}{\sqrt{\pi}} e^{-\left(\frac{\tau}{2\sigma} \right)^2} \right] \end{aligned}$$

or after combining terms

$$\begin{aligned} \int_0^\infty e^{-\frac{1}{2\sigma^2}(\rho-\tau)^2} I_0 \left(\frac{2a_s}{c\sigma^2} [\rho-\tau] \right) d\rho &\approx \frac{\sqrt{2\pi} \sigma}{2} \left[e^{\left(\frac{a_s}{c\sigma} \right)^2} + \operatorname{erf} \left(\frac{\tau}{\sigma\sqrt{2}} \right) \right] \\ \int_0^\infty e^{-\frac{1}{2\sigma^2}(\rho-\tau)^2} I_1 \left(\frac{2a_s}{c\sigma^2} [\rho-\tau] \right) d\rho &\approx \frac{a_s}{c} \left[e^{\left(\frac{a_s}{c\sigma} \right)^2} - \frac{q_\tau}{\sigma\sqrt{2}} \left\{ 1 - e^{-\left(\frac{\tau}{\sigma\sqrt{2}} \right)^2} \right\} \right] \end{aligned}$$

$$\int_0^{\infty} e^{-\frac{1}{2\sigma^2}(\rho-\tau)^2} I_2\left(\frac{2a_s}{c\sigma^2} [\rho-\tau]\right) d\rho \approx \frac{a_s^2 \sqrt{2\pi}}{4c^2 \sigma} \left[e^{\left(\frac{a_s^2}{c\sigma}\right)} + \frac{1}{\sigma\sqrt{2}} \left\{ 1 + \operatorname{erf}\left(\frac{\tau}{\sigma\sqrt{2}}\right) - \frac{4\tau}{\sqrt{\pi}} e^{-\left(\frac{\tau}{2\sigma}\right)^2} \right\} \right]$$

If we substitute the values of σ (8.16ns) and a_s (0.4m.) in the above coefficients of the bracketed terms we find that

$$\frac{\sqrt{2\pi} \sigma}{2} = 10.22$$

$$\frac{a_s}{c} = 1.33$$

$$\frac{a_s^2 \sqrt{2\pi}}{4c^2 \sigma} = 0.136$$

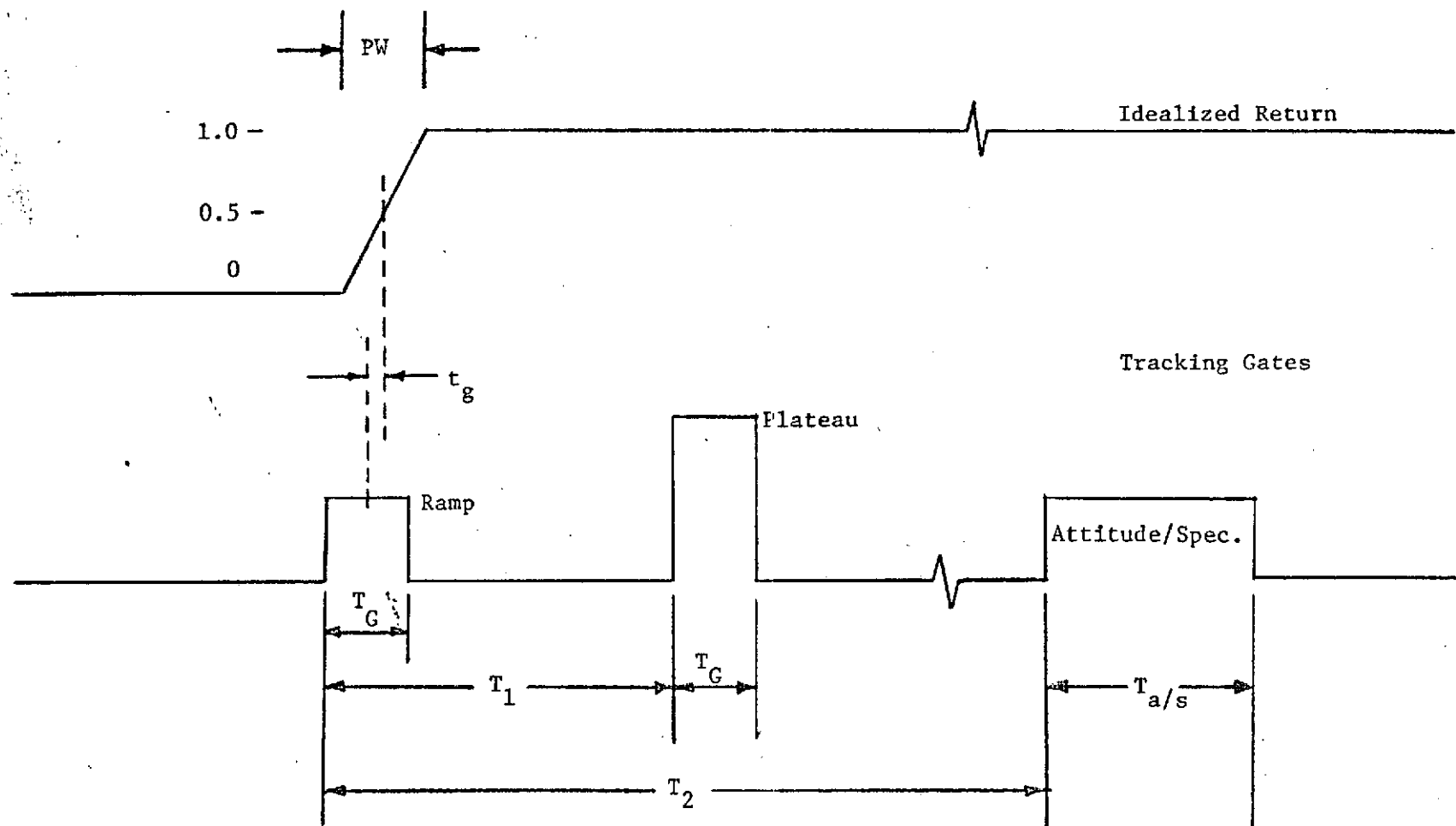
Thus, each coefficient decreases by an order of magnitude from the prior value.

4.0 ALTITUDE-WAVEFORM BIAS EFFECTS AND POINTING ANGLE ESTIMATION

4.1 Waveform Bias Effects on the Altitude

The GEOS-C radar altimeter employs a split-gate time discriminator to extract altitude error on a pulse-by-pulse basis. A typical split-gate arrangement is shown in Figure 4.1 along with an idealized "flat-sea" average return waveform. A discriminator curve is generated by integrating the return waveform over the time extent of the ramp and plateau gates, multiplying the plateau gate integrated value by 0.5, and subtracting this value from the ramp gate integrated value. A typical discriminator curve is shown in Figure 4.2. The discriminator curve is a function of the time variable t_g which is defined (in Figure 4.1) as the shift in position of the two gates relative to the mean return waveform. For purposes of this study, we will set $t_g = 0$ when the center of the ramp gate occurs at a round trip delay time of $2h/c$ where h is the true altitude of the altimeter above mean sea level and c is the speed of light. Since the ramp and plateau gates are separated by a fixed time interval T , a shift in the ramp gate also results in an equal shift in position of the plateau gate. It should also be noted that when the center of the ramp gate occurs later (or earlier) in time than $2h/c$, t_g will be greater (or less) than zero.

The three most important characteristics of the discriminator curve are; (1) the width of the linear position of the curve, (2) the slope of the curve about $\epsilon(t_g) = 0$, and (3) the shift (or bias) of the intercept or $\epsilon(t_g) = 0$ from the $t_g = 0$ point. A large linear range of the discriminator curve is desirable since it permits a one-to-one correspondence between $\epsilon(t_g)$ and t_g for large tracker excursions. The slope must be selected based on sensitivity and stability criteria which are dictated by the design of the remaining portion of the tracker loop. The bias or shift of the $\epsilon(t_g) = 0$ point away from $t_g = 0$ is a consequence of changes in the mean return waveform [1]. All of the above three characteristics are functions of the mean return waveform. In this study, we will investigate how the linear range, slope and bias of the GEOS-C discriminator curve depend on pointing error and sea-state. We will also investigate a slightly different gate configuration which results in a reduced bias for small or moderate waveheights without any sacrifice in the discriminator curve's linear range or slope. This alternate gate configuration demonstrates



INTENSIVE MODE

PW = 12.5 ns

$T_G = 12.5$ ns

$T_1 = 62.5$ ns

$T_2 = 700$ ns

$T_{a/s} = 200$ ns

$\sigma_j \approx 3$ ns

GLOBAL MODE

PW = 200 ns

$T_G = 200$ ns

$T_1 = 300$ ns

$T_2 = 700$ ns

$T_{a/s} = 200$ ns

$\sigma_j \approx 6.5$ ns

Fig. 4.1 GEOS-C Tracking Gate Configuration and Defining Parameters.

Ramp Gate Integrated Value $-0.5 \times (\text{Plateau Gate Integrated Value}) = \epsilon(t_g)$

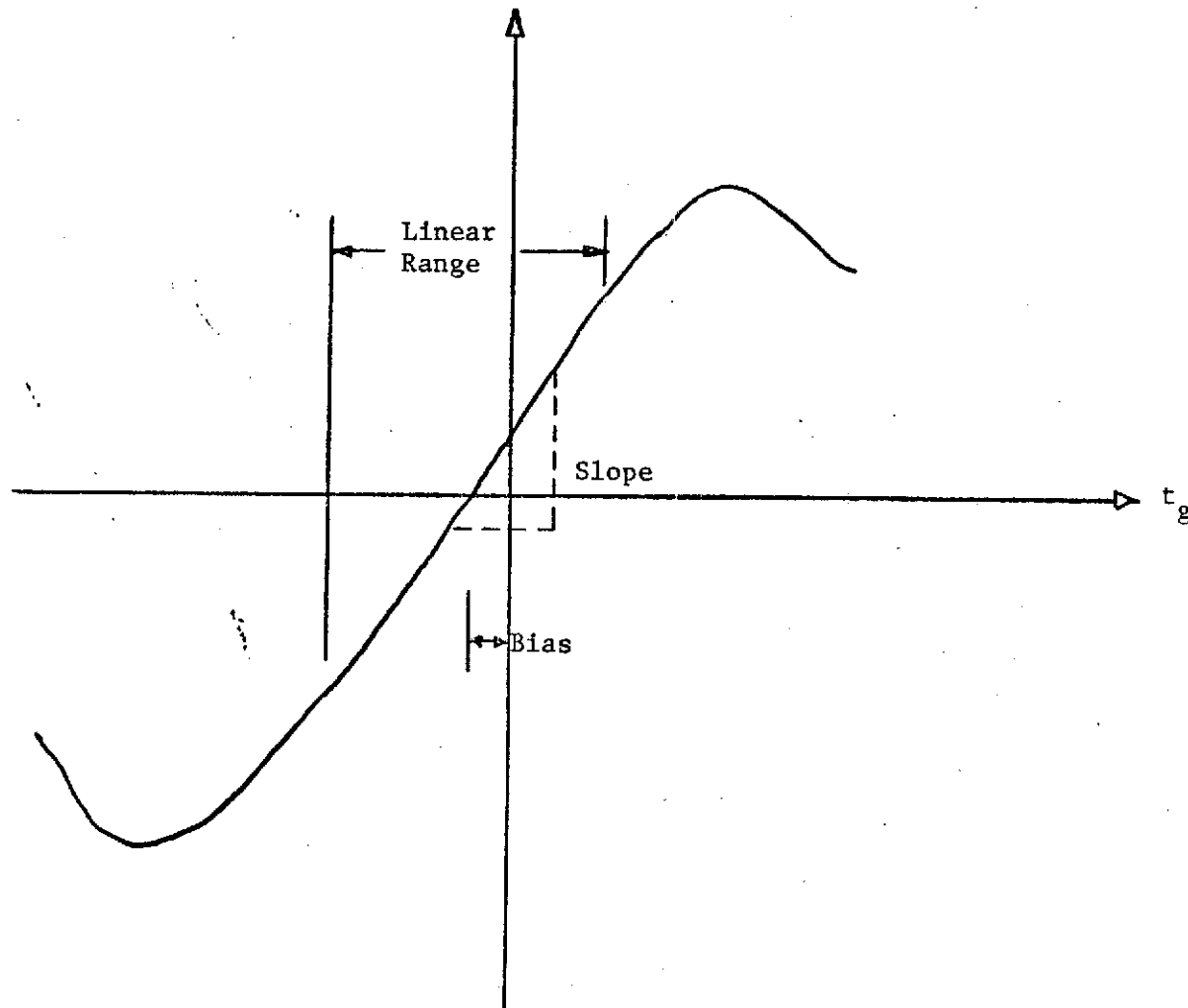


Fig. 4.2 Typical Discriminator Curve Resulting from a Split-Gate Configuration.

the desirability of an adaptive tracker system. No consideration was given to a 3 or 1 ns system since the results presented here for a GEOS-C type system indicate that the bias errors will be very small and, in addition, knowledge of the "sea-state" will permit correction of the bias to a very small value.

4.1.1 Analysis

The mean return waveform for short-pulse altimeters operated at or near nadir is a convolution [2] of the system point target response, the flat-sea impulse response, the waveheight probability density function, and the tracking loop jitter. For purposes of this study, we will ignore the tracker loop time jitter since it will be relatively small for GEOS-C, i.e., $\sigma_j \sim 3$ ns. A Gaussian function will be used to describe the system point target response since previous studies [3] have shown that this is a reasonable approximation. That is, if we denote P_{pt} as the point target response, then

$$P_{pt}(\tau) = e^{-\left(\frac{\tau^2}{2\sigma_p^2}\right)} \quad (1)$$

and the half-power pulsewidth (PW) is related to the standard deviation of the Gaussian approximation (σ_p) by the following,

$$\sigma_p^2 = 0.181(PW)^2.$$

Similarly, the waveheight probability density function will be assumed to be Gaussian, i.e.,

$$P_{ss}(z) = \frac{1}{\sqrt{2\pi\sigma_s^2}} e^{-\left(\frac{z^2}{2\sigma_s^2}\right)}, \quad (2)$$

where σ_s is the rms roughness of the ocean surface. The convolution of (1) and (2), with z converted to two-way ranging time, yields the following Gaussian function

$$P_{pt}(\tau) * P_{ss}(z) = \frac{1}{\alpha} e^{-\left(\frac{\tau^2}{2\sigma_p^2\alpha^2}\right)} \quad (3)$$

where

$$\alpha = \sqrt{\left(\frac{2\sigma_s}{c\sigma_p}\right)^2 + 1}.$$

For the Intensive Mode of GEOS-C, we are dealing with a pulsewidth limited geometry, thus we need only consider the shape of the antenna pattern very near boresight in computing the mean return waveform. We may, therefore, approximate the antenna pattern as circularly symmetric and Gaussian, i.e.,

$$G_A(\theta) = G_0 e^{-\frac{2}{\gamma} \sin^2 \theta}, \quad (4)$$

where G_0 is the boresight gain, θ is the angle measured with respect to boresight, and γ is the antenna pattern taper factor. If we match (4) to the measured pattern at the 1/2-power point, we find that

$$\gamma = 2.895 \sin^2\left(\frac{BW}{2}\right), \quad (5)$$

where BW is the 3 dB beamwidth of the measured antenna pattern. Under the Gaussian antenna pattern assumption, it has been previously shown [3] that the flat-sea impulse response is given by

$$\begin{aligned} P_i(\tau, \xi) = & \frac{G_0^2 \lambda^2 c \sqrt{\pi} \sigma^0(\xi)}{(4\pi)^3 h^3 L_p} \frac{1}{\left(\frac{c\tau}{2h} + 1\right)^3} \exp \left\{ -\frac{4}{\gamma} \left[-\frac{\cos^2 \xi}{\left(\frac{c\tau}{2h} + 1\right)^2} \right. \right. \\ & \left. \left. - \left\{ 1 - \left(\frac{c\tau}{2h} + 1\right)^{-2} \right\} \sin^2 \xi \right] \right\} \cdot \sum_{n=0}^{\infty} \frac{(-1)^n \Gamma(n+1/2)}{\Gamma(n+1)} \\ & \cdot I_n \left(\sqrt{\left(\frac{c\tau}{2h} + 1\right)^2 - 1} \frac{4 \sin 2\xi}{\gamma \left(\frac{c\tau}{2h} + 1\right)} \right) \left[\tan \xi \sqrt{\left(\frac{c\tau}{2h} + 1\right)^2 - 1} \right]^n \end{aligned} \quad (6)$$

for $\tau > 0$ and $P_i(\tau, \xi) = 0$ for $\tau < 0$, where ξ is the pointing angle of the antenna boresight with respect to nadir. The complete mean return waveform is convolution of (6) and (3), i.e.,

$$\begin{aligned}
P_r(\tau, \xi) = & \Gamma \int_0^{\infty} \left[\frac{c\hat{\tau}}{2h} + 1 \right]^{-3} \exp \left\{ -\frac{4}{\gamma} \left[1 - \frac{\cos^2 \xi}{\left(\frac{c\hat{\tau}}{2h} + 1 \right)^2} - \left\{ 1 - \left(\frac{c\hat{\tau}}{2h} + 1 \right)^{-2} \right\} \sin^2 \xi \right] \right\} \\
& \cdot \exp \left\{ -\frac{(\tau - \hat{\tau})^2}{2\sigma_p^2 \alpha^2} \right\} \sum_{n=0}^{\infty} \frac{(-1)^n \Gamma(n+1/2)}{\Gamma(n+1)} I_n \left[\sqrt{\left(\frac{c\hat{\tau}}{2h} + 1 \right)^2 - 1} \frac{4 \sin 2\xi}{\gamma \left(\frac{c\hat{\tau}}{2h} + 1 \right)^2} \right] \\
& \cdot \left[\tan \xi \sqrt{\left(\frac{c\hat{\tau}}{2h} + 1 \right)^2 - 1} \right]^n d\hat{\tau}, \tag{7}
\end{aligned}$$

where

$$\Gamma = \frac{G_o^2 \lambda^2 c \sqrt{\pi} \sigma^o(\xi)}{(4\pi)^3 h^3 L_p} \left[\left(\frac{2\sigma_s}{c\sigma_p} \right)^2 + 1 \right]^{-1/2}$$

and the $I_n(\cdot)$ are Bessel functions of the second kind and order n . If we let $x = \hat{\tau}/\sigma_p \alpha \sqrt{2}$ and $q = c\sigma_p \alpha/h \sqrt{2}$ then (7) becomes

$$\begin{aligned}
P_r(\tau, \xi) = & \Gamma \sigma_p \alpha \sqrt{2} \int_0^{\infty} [qx+1]^{-3} \exp \left\{ -\frac{4}{\gamma} \left[1 - \frac{\cos^2 \xi}{(qx+1)^2} - \left\{ 1 - (qx+1)^{-2} \right\} \sin^2 \xi \right] \right\} \\
& \cdot \exp \left\{ -\left(-x + \frac{\tau}{\sigma_p \alpha \sqrt{2}} \right)^2 \right\} \sum_{n=0}^{\infty} \frac{(-1)^n \Gamma(n+1/2)}{\Gamma(n+1)} I_n \left[\sqrt{(qx+1)^2 - 1} \frac{4 \sin 2\xi}{\gamma (qx+1)^2} \right] \\
& \cdot \left[\tan \xi \sqrt{(qx+1)^2 - 1} \right]^n dx \tag{8}
\end{aligned}$$

For GEOS-C, the point target response half-power pulsewidth (PW) will be assumed to be 12.5 ns; thus, $\sigma_p = 5.32$ ns. Since the beamwidth of the GEOS-C antenna is about 2.6 degrees, $\gamma = 1.49 \times 10^{-3}$. The altitude of the GEOS-C spacecraft will be about 880 km, hence $q = 1.28 \times 10^{-6}$. Provided we restrict the range of τ to less than, say 500 ns, we can ignore all terms in the series in (8) except for $I_0(\cdot)$ since for $\xi \leq 3^\circ$ the factor raised to the n^{th}

power is very small but dominant. To evaluate the remaining integral, we note that all terms inside the integral show a small variation compared to the Gaussian pulse shape factor, and also

$$\begin{aligned} 1-(qx+1)^{-2} \cos^2 \xi &\approx 1 - \cos^2 \xi (1-2qx) \\ &= \sin^2 \xi + 2qx \cos^2 \xi \end{aligned}$$

and

$$[1-(qx+1)^{-2}] \sin^2 \xi \approx 2qx \sin^2 \xi$$

and

$$\frac{\sqrt{(qx+1)^2 - 1}}{(qx+1)^2} \approx \sqrt{2qx}.$$

Hence, for $0 \leq \tau \leq 500$ ns and $\xi \leq 3^\circ$,

$$\begin{aligned} P_r(\tau, \xi) &\approx \Gamma \sigma_p \alpha \sqrt{2\pi} \exp \left\{ -\frac{4}{\gamma} \left[\sin^2 \xi + \frac{2q}{\sigma_p \alpha \sqrt{2}} \tau \cos 2\xi \right] \right\} \\ &\cdot I_0 \left(\frac{4 \sin 2\xi}{\gamma} \sqrt{\frac{2q\tau}{\sigma_p \alpha \sqrt{2}}} \right) \int_0^\infty e^{-\left(-x + \frac{\tau}{\sigma_p \alpha \sqrt{2}}\right)^2} dx \end{aligned} \quad (9)$$

or

$$\begin{aligned} P_r(\tau, \xi) &= \Gamma \sigma_p \alpha \sqrt{2\pi} e^{-\frac{4}{\gamma} \sin^2 \xi} e^{-\frac{4c}{\gamma h} \cos 2\xi \tau} \\ &\cdot I_0 \left(\frac{4 \sqrt{c} \sin^2 \xi}{\gamma \sqrt{h}} \sqrt{\tau} \right) \left\{ \frac{1}{2} \left[1 + \operatorname{erf} \left(\frac{\tau}{\sigma_p \alpha \sqrt{2}} \right) \right] \right\}. \end{aligned} \quad (10)$$

When $\tau < 0$, we see from (8) that the correct expression for $P_r(\tau, \xi)$ is

$$P_r(\tau, \xi) \approx \Gamma \sigma_p \alpha \sqrt{2\pi} e^{-\frac{4}{\gamma} \sin^2 \xi} \left\{ \frac{1}{2} \left[1 + \operatorname{erf} \left(\frac{\tau}{\sigma_p \alpha \sqrt{2}} \right) \right] \right\}. \quad (11)$$

The approximate expressions given by (10) and (11) have been checked with results obtained by numerically integrating (8) and the agreement was found to be excellent.

We normalize (10) and (11) to account for the action of the AGC and form $\bar{P}_r(\tau, \xi)$ where

$$\bar{P}_r(\tau, \xi) = \bar{A}(\tau) \left\{ \frac{1}{2} [1 + \operatorname{erf}(\frac{\tau}{\sigma_p \alpha \sqrt{2}})] \right\}, \quad (12)$$

and

$$\bar{A}(\tau) = \begin{cases} e^{-\frac{4c}{\gamma h} \cos 2\xi \tau} I_0 \left(\frac{4\sqrt{c} \sin 2\xi}{\gamma \sqrt{h}} \sqrt{\tau} \right) & \tau \geq 0 \\ 1 & \tau < 0. \end{cases} \quad (13)$$

The discriminator curve is obtained by integrating (12) over the time expanse of the ramp and plateau gates, multiplying the integrated plateau value by 0.5 and subtracting this value from the integrated ramp value. If $\varepsilon(t_g)$ is the discriminator curve, then

$$\varepsilon(t_g) = \int_{-\frac{T_G}{2} + t_g}^{\frac{T_G}{2} + t_g} w(\tau - t_g) \bar{P}_r(\tau) d\tau - \frac{1}{2} \int_{T - \frac{T_G}{2} + t_g}^{T + \frac{T_G}{2} + t_g} w(\tau - T - t_g) \bar{P}_r(\tau) d\tau \quad (14)$$

where we have assumed that the ramp and plateau gate lengths are equal and

T_G = gate length,

$w(\tau)$ = gate weighting function,

T = time delay between the start of the ramp gate and the start of the plateau gate.

t_g = time shift in the position of the center of the ramp gate with respect to the total two-way delay time of $2h/c$.

For GEOS-C, the gate width T_G is matched to the pulsewidth, thus, $T_G = 12.5$ ns. Since

and
$$\frac{4c}{\gamma h} \cos 2\xi \ll 1$$

$$\frac{4 \sqrt{c} \sin 2\xi}{\gamma \sqrt{h}} \ll 1$$

and the argument of $I_0(\cdot)$ in (13) varies as $\sqrt{\tau}$, the factor $\bar{A}(\tau)$ is almost constant over the ranges of integration in (14) and

$$\begin{aligned} \epsilon(t_g) \approx & \frac{\bar{A}(t_g)}{2} \int_{-\frac{T_G}{2} + t_g}^{\frac{T_G}{2} + t_g} w(\tau - t_g) [1 + \operatorname{erf}(\frac{\tau}{\sigma_p \alpha \sqrt{2}})] d\tau \\ & - \frac{\bar{A}(t_g + T)}{4} \int_{T - \frac{T_G}{2} + t_g}^{\frac{T_G}{2} + t_g} w(\tau - T - t_g) [1 + \operatorname{erf}(\frac{\tau}{\sigma_p \alpha \sqrt{2}})] d\tau \end{aligned} \quad (15)$$

We define the gate weighting function to have unit area, i.e.,

$$\int_{-\frac{T_G}{2}}^{\frac{T_G}{2}} w(\tau) d\tau = 1,$$

thus

$$\epsilon(t_g) = \frac{\bar{A}(t_g)}{2} - \frac{\bar{A}(T + t_g)}{4} + \frac{\bar{A}(t_g)}{2} \int_{-\frac{T_G}{2} + t_g}^{\frac{T_G}{2} + t_g} w(\tau - t_g) \operatorname{erf}(\frac{\tau}{\sigma_p \alpha \sqrt{2}}) d\tau$$

$$\begin{aligned}
& T + \frac{T_G}{2} + t_g \\
& - \frac{\bar{A}(T+t_g)}{4} \int_{T - \frac{T_G}{2} + t_g}^{T + \frac{T_G}{2} + t_g} w(\tau - T - t_g) \operatorname{erf}\left(\frac{\tau}{\sigma_p \alpha \sqrt{2}}\right) d\tau \\
& T - \frac{T_G}{2} + t_g
\end{aligned}$$

The exact shape of the gate weighting function is not known, however, we will assume that it is rectangular, i.e.,

$$w(\tau) = \begin{cases} \frac{1}{T_G} & -\frac{T_G}{2} \leq \tau \leq \frac{T_G}{2} \\ 0 & |\tau| > \frac{T_G}{2} \end{cases}$$

The time discriminator curve thus reduces to the following form;

$$\begin{aligned}
\varepsilon(t_g) = 0.5 \left\{ \bar{A}(t_g) \left[1 + \frac{\sigma_p \alpha \sqrt{2}}{T_G} \left(x \operatorname{erf} x + \frac{e^{-x^2}}{\sqrt{\pi}} \right) \right] \right. \\
\left. - 0.5 \bar{A}(T+t_g) \left[1 + \frac{\sigma_p \alpha \sqrt{2}}{T_G} \left(x \operatorname{erf} x + \frac{e^{-x^2}}{\sqrt{\pi}} \right) \right] \right\} \quad (16)
\end{aligned}$$

Equation (16) can be rewritten in a somewhat more convenient form as follows:

$$\begin{aligned}
\varepsilon(t_g) = 0.5 \left\{ \bar{A}(t_g) \left[1 + S\left(\frac{t_g \pm T_G/2}{\sigma_p \alpha \sqrt{2}}\right) \right] \right. \\
\left. - 0.5 \bar{A}(T+t_g) \left[1 + S\left(\frac{T+t_g \pm T_G/2}{\sigma_p \alpha \sqrt{2}}\right) \right] \right\} \quad (17)
\end{aligned}$$

where $S(\cdot)$ is easily deduced from equation (16). We note from (13) and (16) that the $\bar{A}(\cdot)$ are functions of antenna pointing angle and pattern and altitude

while the $S(\cdot)$ are the gate responses to a mean return waveform which is free of antenna and pointing angle effects. However, unlike the mean return waveform in equation (12), the discriminator output is not a simple product of these two factors.

Equation (16) provides a very rapid means of evaluating the performance of split-gate time discriminator systems. It is a significant result in itself since it results in a closed form expression. Prior studies of discriminator optimization have been hindered by the necessity of accomplishing a three-fold numerical integration for $\epsilon(t_g)$, i.e., a two-dimensional surface integration to obtain $P_r(\tau)$ and third integration to determine the gate response to $P_r(\tau)$. The above formula has been applied to the Skylab S-193 radar altimeter where the pulsewidth is considerably longer (72 ns, 3 dB) and the antenna beamwidth smaller (1.5°, 3 dB). The particular combination of pulsewidth, beamwidth and altitude (435 km) for Skylab results in a mean return which is neither completely beamwidth nor pulsewidth limited. However, the results obtained from (12) and (16) were in excellent agreement with numerical integration calculations. We therefore conclude that (12) and (16) have a greater range of validity than the approximations would tend to indicate. It is interesting to note that from equation (11) it can be shown that the peak of the average return power decreases as $\exp(-4 \sin^2 \xi / \gamma)$ for very near nadir and as $1/\sin 2\xi$ further away from nadir. Such knowledge of the decrease in return power as a function of pointing error is very important in designing the proper AGC dynamic range of the altimeter receiver.

4.1.2 Results

In the following we will present results on time discriminator bias, slope and linearity as a function of pointing angle and waveheight. Figure 4.3 shows the discriminator curve for the GEOS-C gate configuration (where the ramp and plateau gates are separated by 50 ns ($T = 62.5$ ns)), an rms waveheight of 0.1 m, and pointing angles of 0° and 1.5° off-nadir. Apart from a shift in the bias point, i.e., the value of t_g such that $\epsilon(t_g) = 0$, there is no appreciable change in the shape of the curve. We note that the linearity range is about $-0.3T_g \leq t_g \leq 0.3T_g$. Figure 4.4 demonstrates the effect of a 1.0 m (rms) surface waveheight on the discriminator curve. Comparing these results with those shown in Figure 4.3 indicates a slight increase in bias and a decrease in slope while the linearity range increases to $-0.4T_g \leq t_g \leq -0.3T_g$. The decrease in slope will decrease the equivalent gain

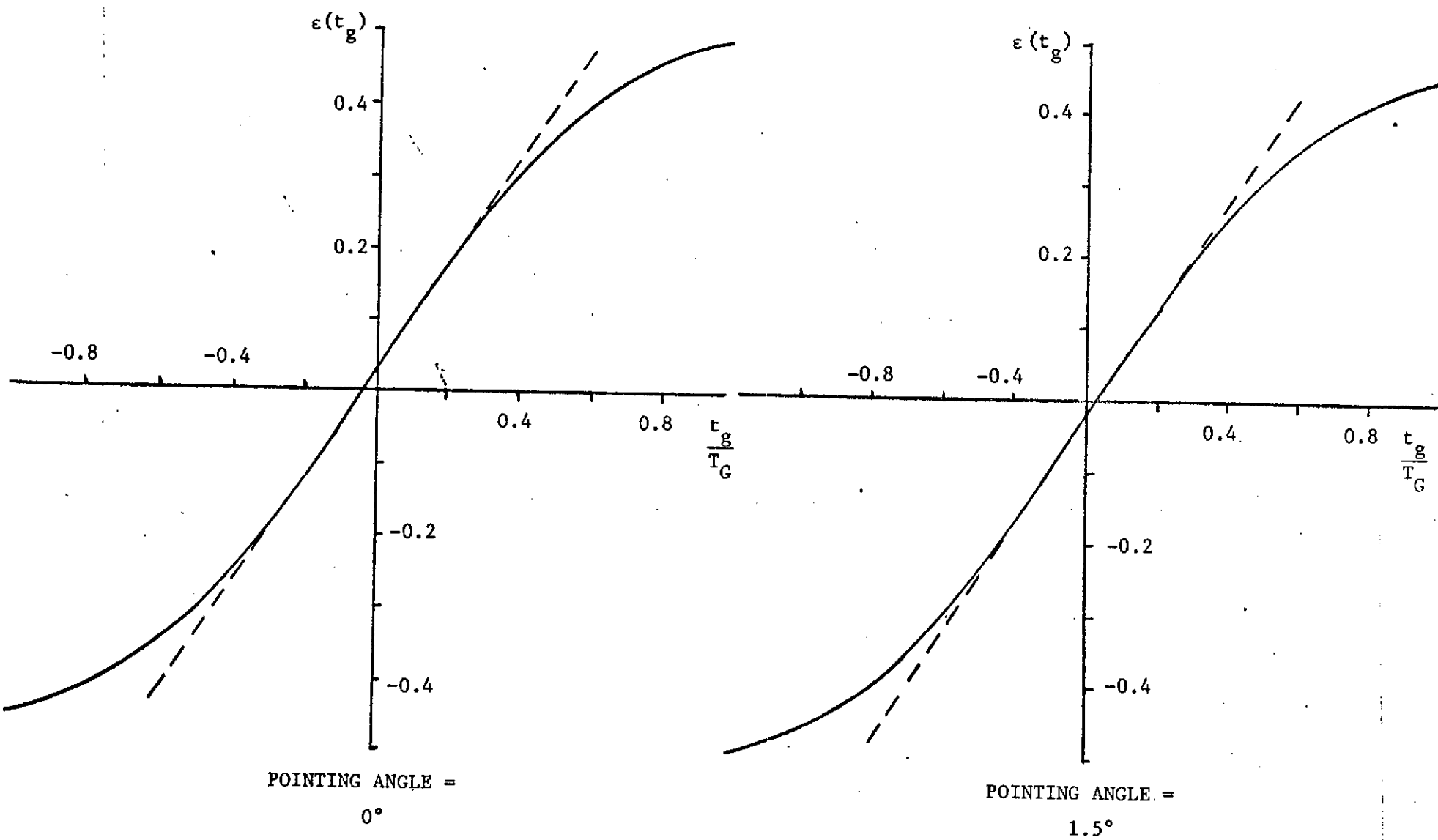


Fig. 4.3 GEOS-C Discriminator Curves for a Gate Separation of 50 ns and $\sigma_s = 0.1$ m ($H_{1/3} = 1.31$ ft.)

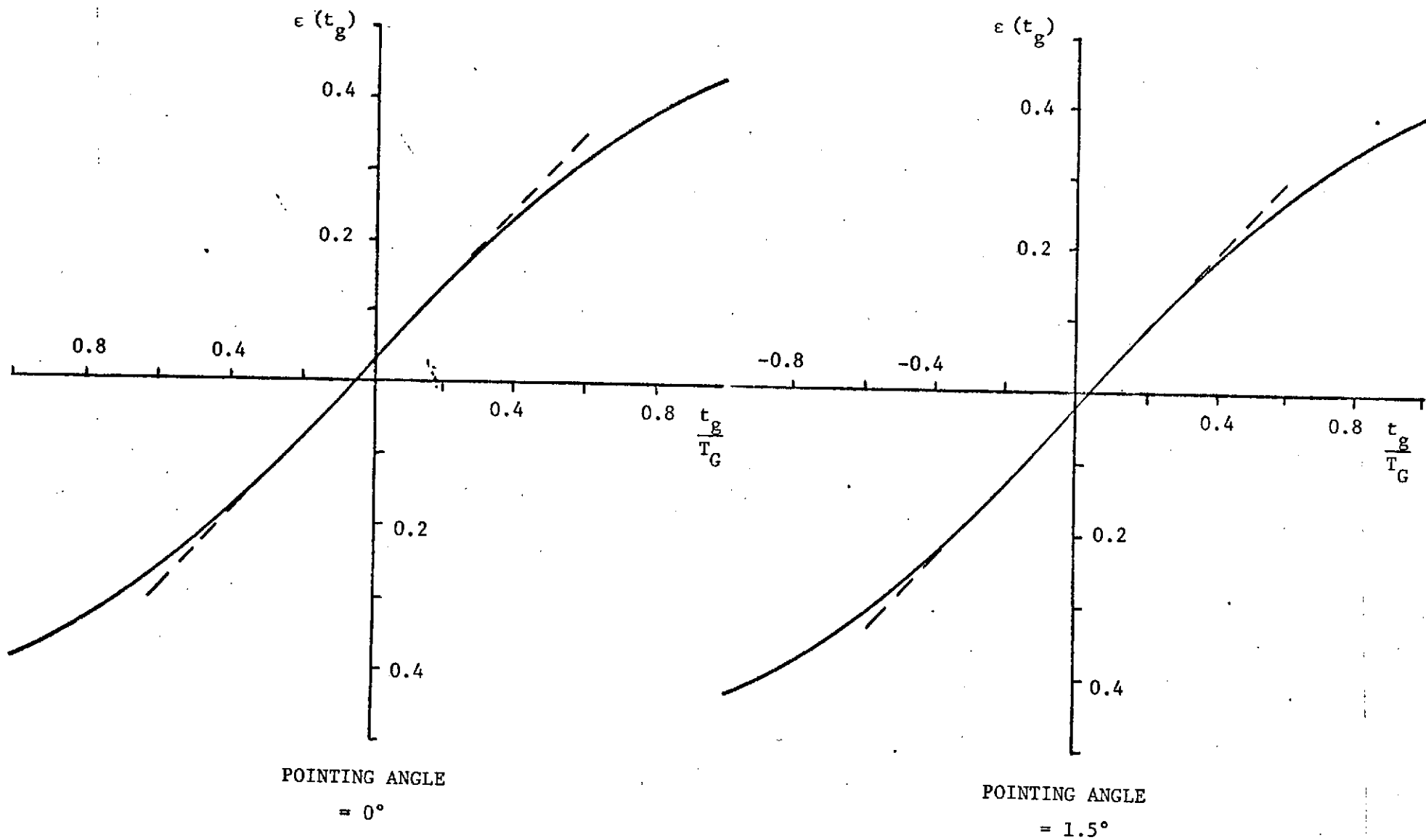


Fig. 4.4 GEOS-C Discriminator Curves for a Gate Separation of 50 ns and $\sigma_s = 1.0$ m ($H_{1/3} = 13.12$ ft.)

of the tracker loop and increase its settling time; however, since the open loop bandwidth is unchanged there will be no appreciable increase in tracker jitter. Figure 4.5 illustrates the effect of a 2.5 m (rms) waveheight on the discriminator curve. Although the linear range of the curve increases, there is a marked reduction in slope and the bias is seen to increase both in magnitude and sensitivity to pointing angle. Figure 4.6 summarizes the resultant altitude bias errors as a function of pointing error and waveheight for the GEOS-C Intensive Mode.

The rather large gate separation in the GEOS-C Intensive Mode tracker loop places the plateau gate in that region of the return waveform which is sensitive to pointing errors. By reducing this separation, it should be possible to reduce the sensitivity of the bias to pointing angle. Figures 4.7, 4.8 and 4.9 show discriminator curves for a gate separation of 12.5 ns and waveheights of 0.1, 1.0 and 2.5 m (rms), respectively. For waveheights of 0.1 and 1.0 m, we note a reduction in bias error and sensitivity to pointing angle without any significant change in linear range or slope from that obtained with the 50 ns gate separation. However, when the waveheight increases to 2.5 m (rms), there is a marked increase in altitude bias although the sensitivity to pointing angle remains small. In addition, the linear portion of the discriminator curve is no longer centered about the bias point but has shifted to the right of the bias point. The bias errors for a gate separation of 12.5 ns are summarized in Figure 4.10 and it is noted that the 12.5 ns gate separation provides improved performance over the 50 ns separation for low to moderate seas but is very poor for high seas.

Figures 4.11, 4.12, 4.13 and 4.14 show the discriminator curves and bias errors for contiguous tracking gates (no separation). We note that the linear range of the discriminator curves are reduced relative to the 50 and 12.5 ns gate separation curves. As shown in Figure 4.14 the bias errors for contiguous tracking gates are much more sensitive to waveheight than the 12.5 and 50 ns configurations.

4.1.3 Conclusions

In this study we have obtained a concise closed form expression for a split-gate time discriminator curve applicable to the GEOS-C Intensive Mode. Results for the GEOS-C tracking gate configuration indicate bias errors on the

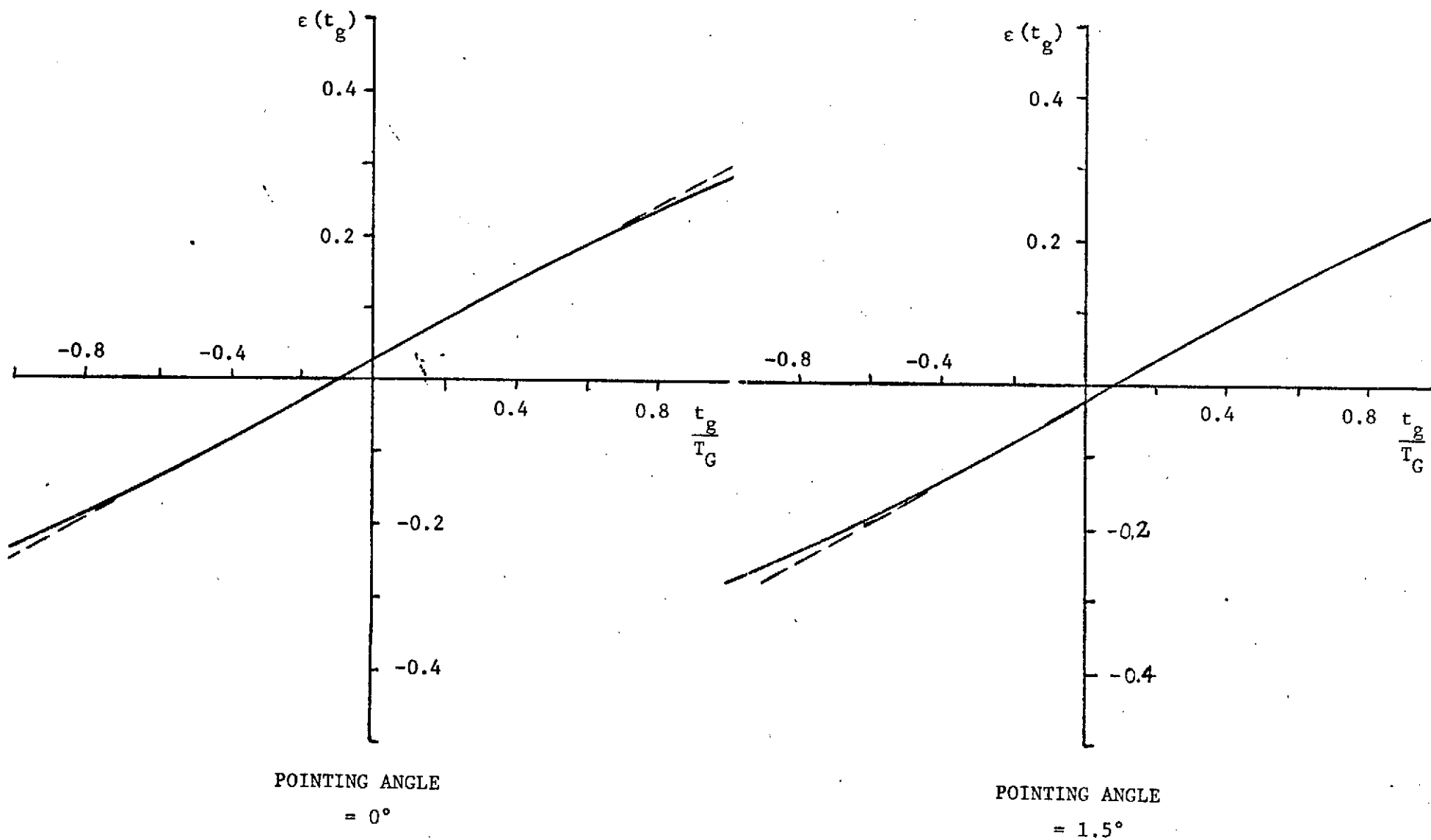


Fig. 4.5 GEOS-C Discriminator Curves for a Gate Separation of 50 ns and $\sigma_s = 2.5$ m ($H_{1/3} = 32.8$ ft.)

ALTITUDE BIAS DUE TO WAVEHEIGHT AND POINTING ERROR EFFECTS
(In Cm)

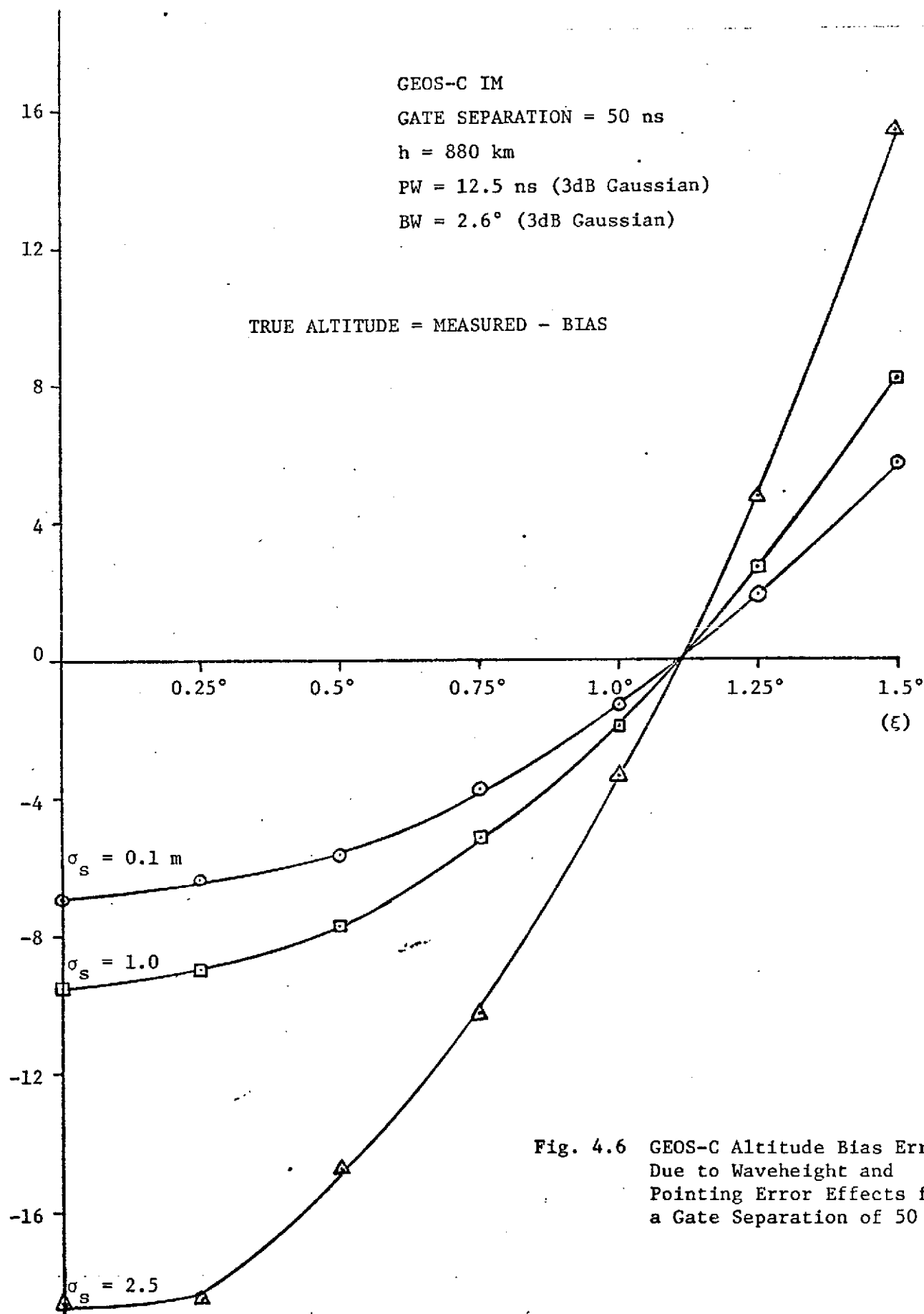


Fig. 4.6 GEOS-C Altitude Bias Error Due to Waveheight and Pointing Error Effects for a Gate Separation of 50 ns.

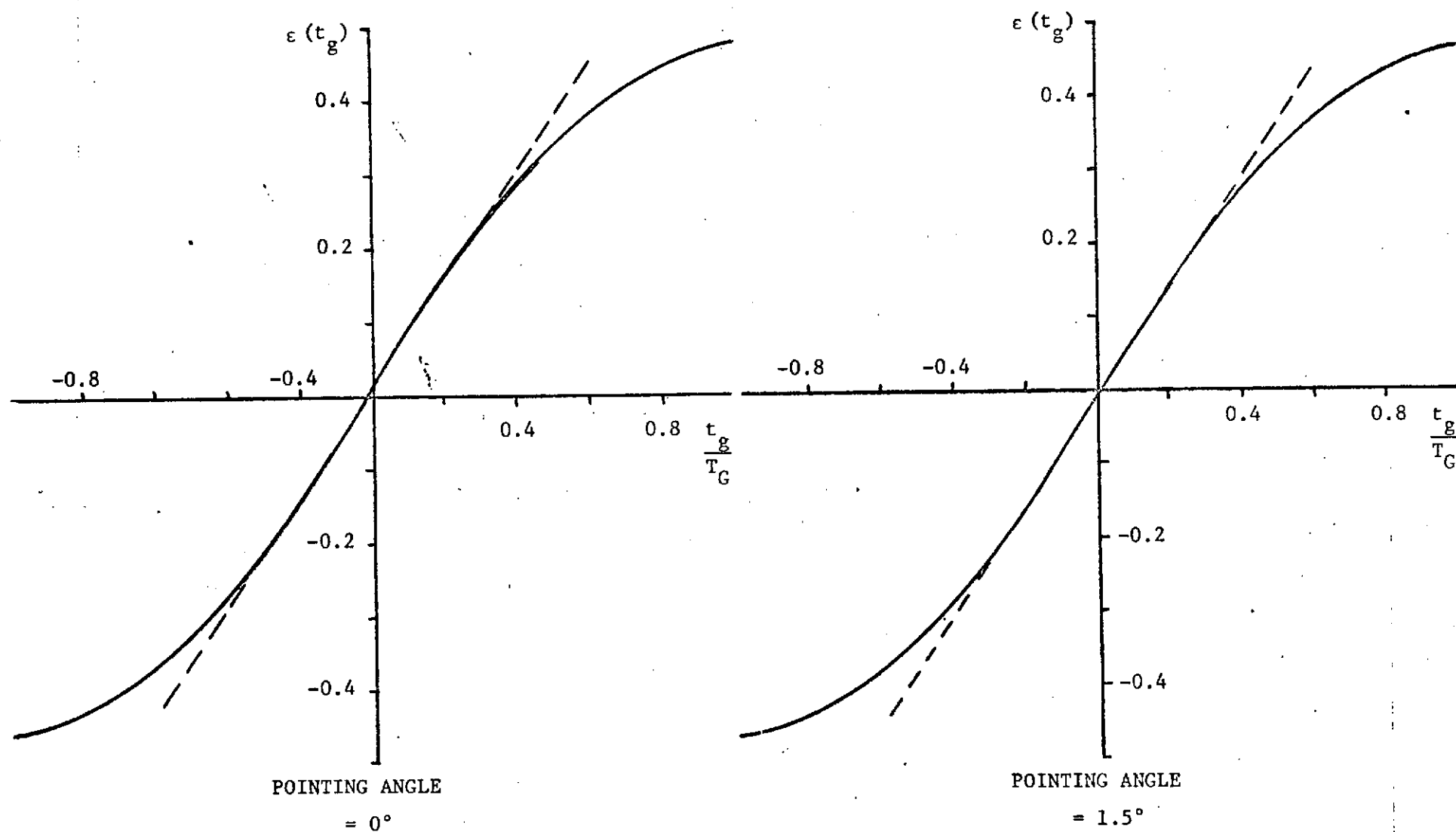


Fig. 4.7 Discriminator Curve for a Gate Separation of 12.5 ns and $\sigma_s = 0.1$ m ($H_{1/3} = 1.31$ ft.).

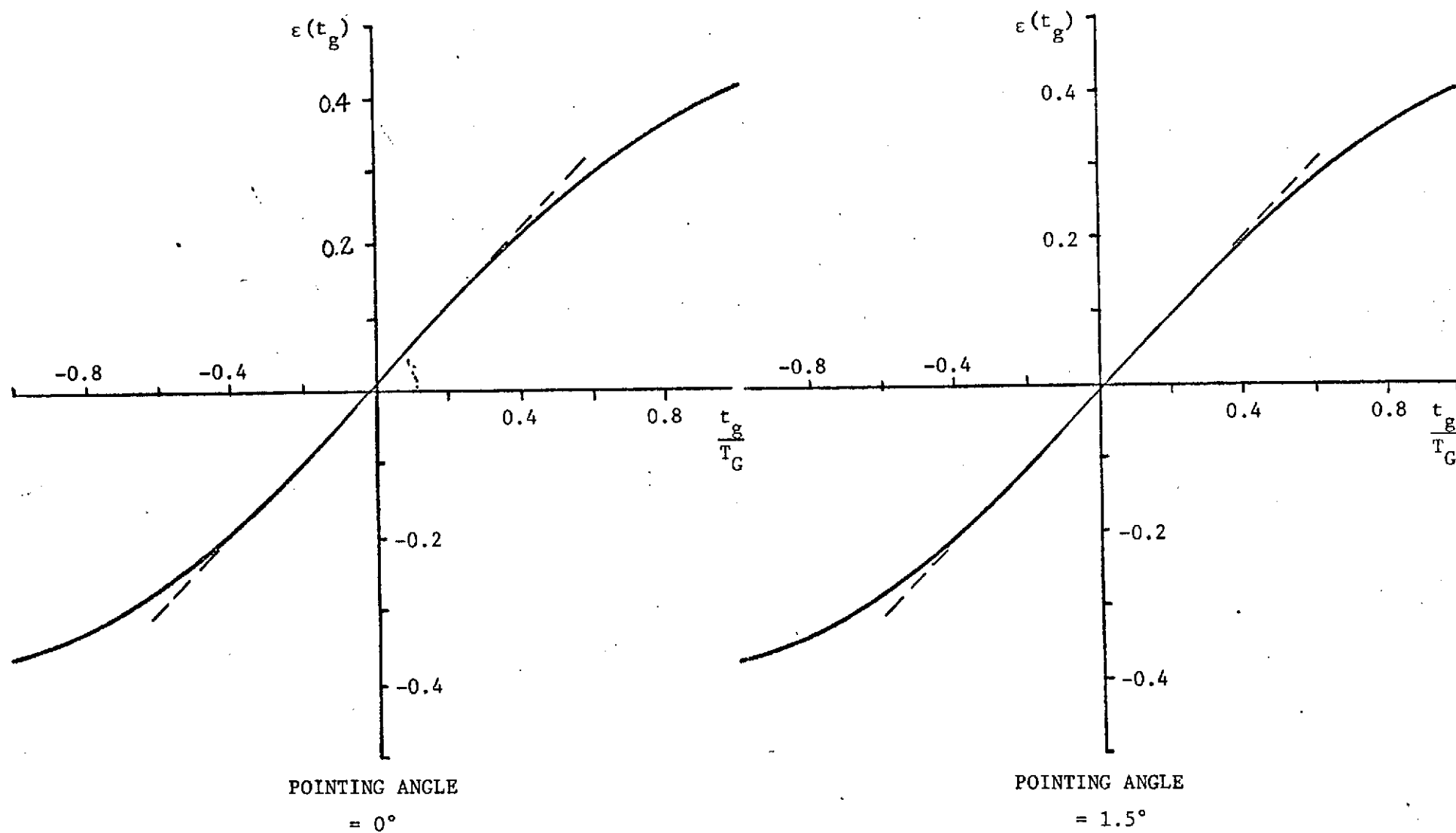


Fig. 4.8 Discriminator Curve for a Gate Separation of 12.5 ns and $\sigma_g = 1.0$ m ($H_{1.3} = 13.12$ ft.)

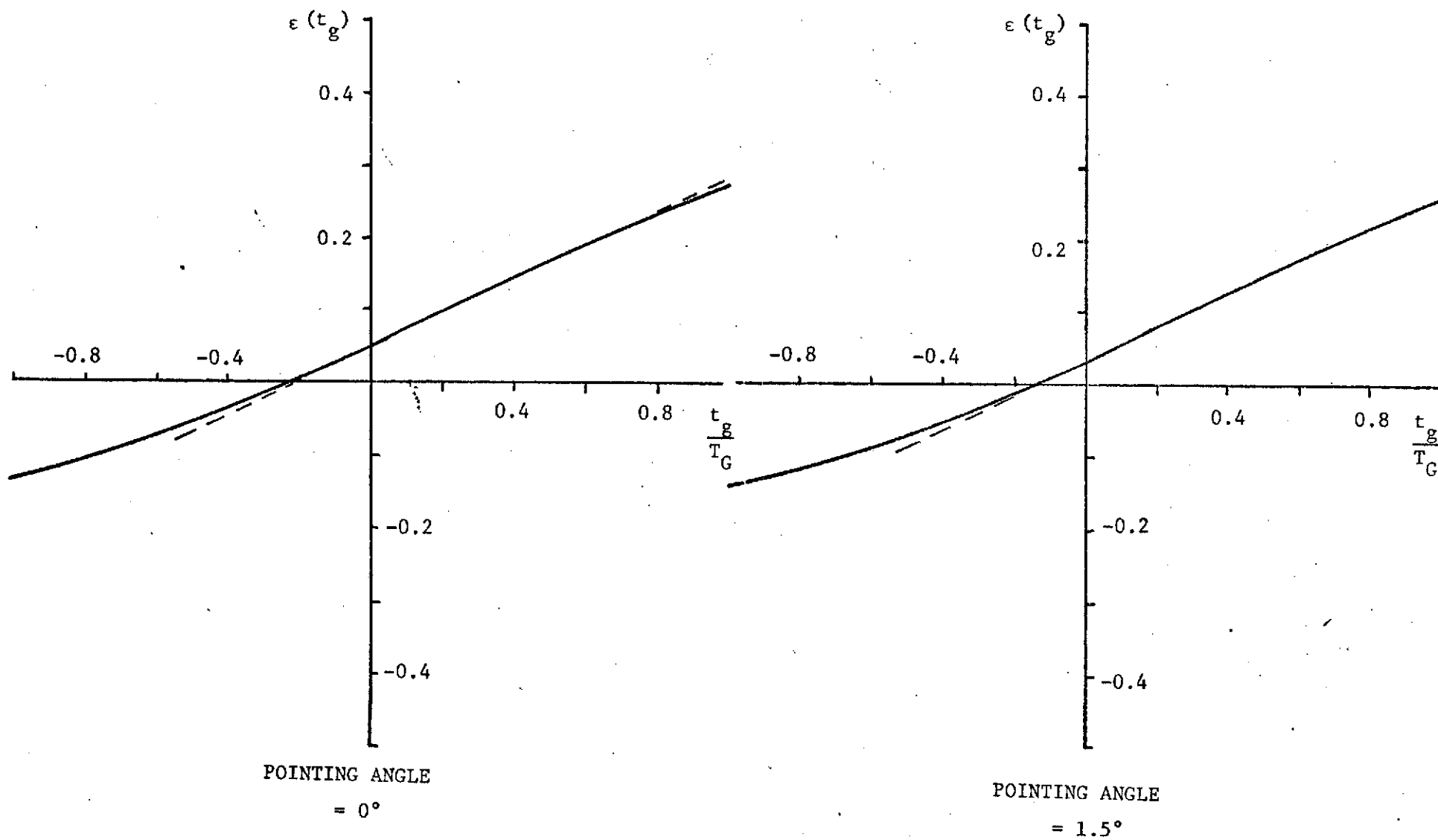


Fig. 4.9 Discriminator Curve for a Gate Separation of 12.5 ns and $\sigma_s = 2.5$ m ($H_{1/3} = 32.8$ ft.)

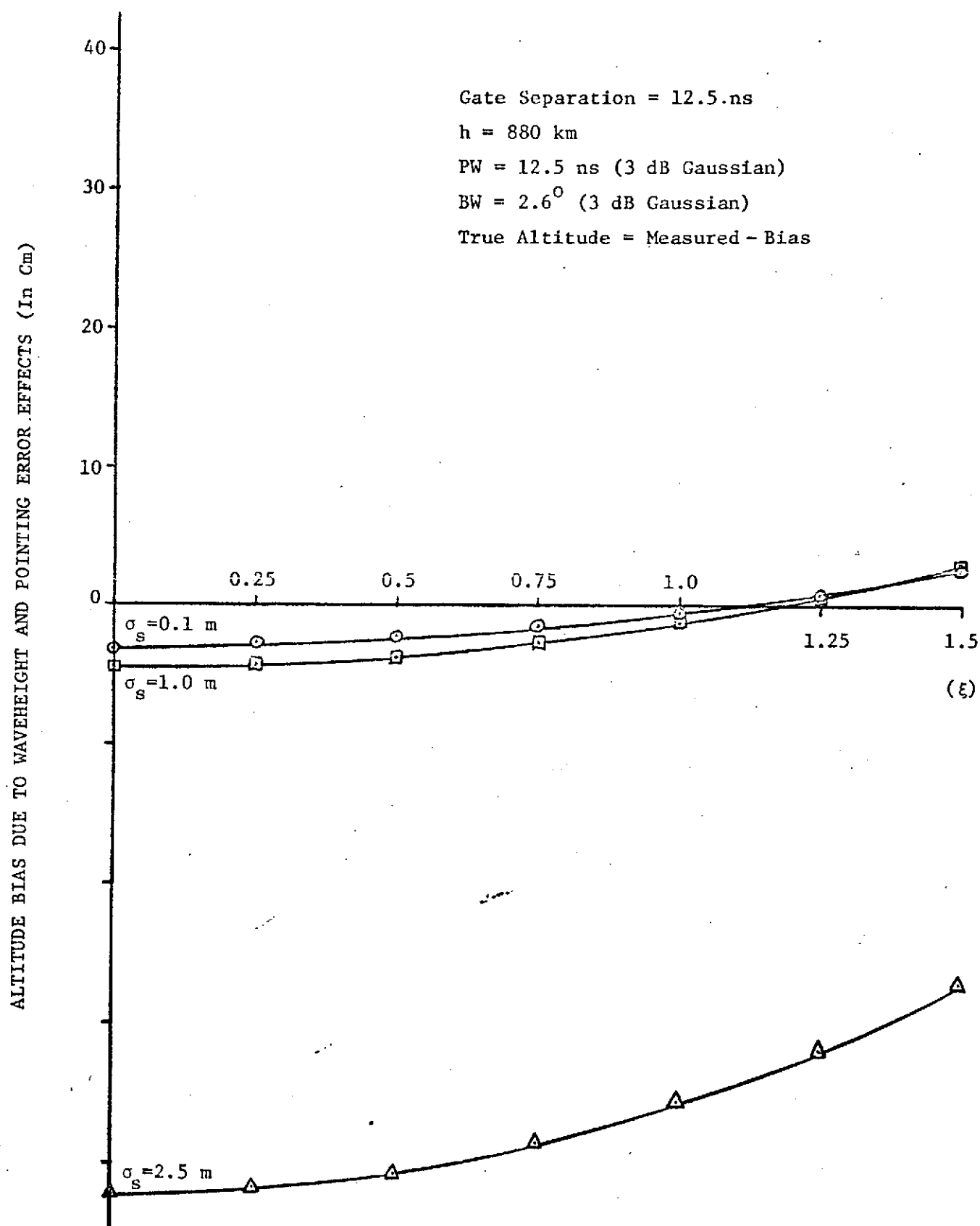


Fig. 4.10 Altitude Bias Errors due to Waveheight and Pointing Error Effects for a Gate Separation of 12.5 ns.

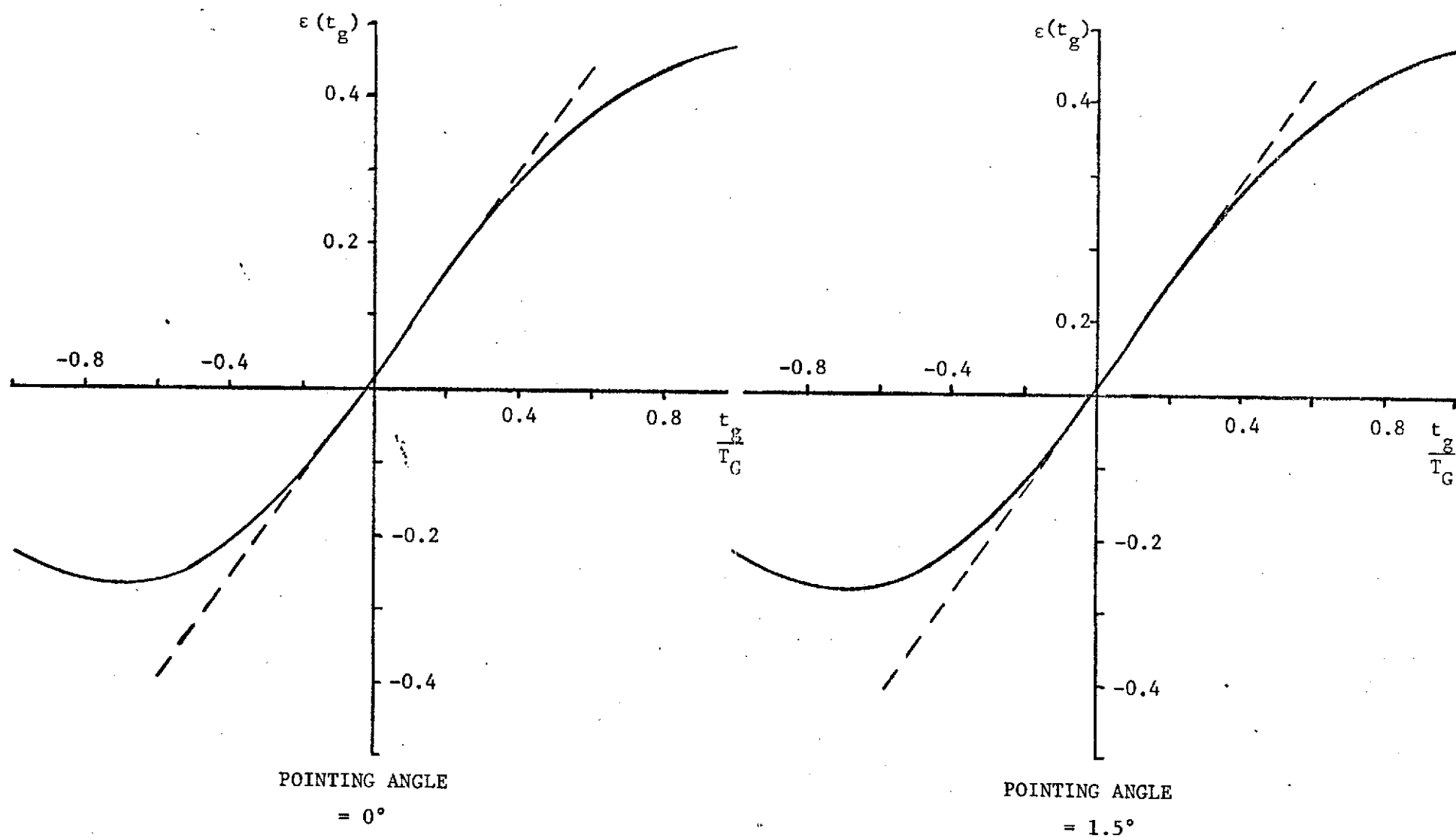


Fig. 4.11 Discriminator Curve for Contiguous Gates and $\sigma_s = 0.1$ m ($H_{1/3} = 1.31$ ft.).

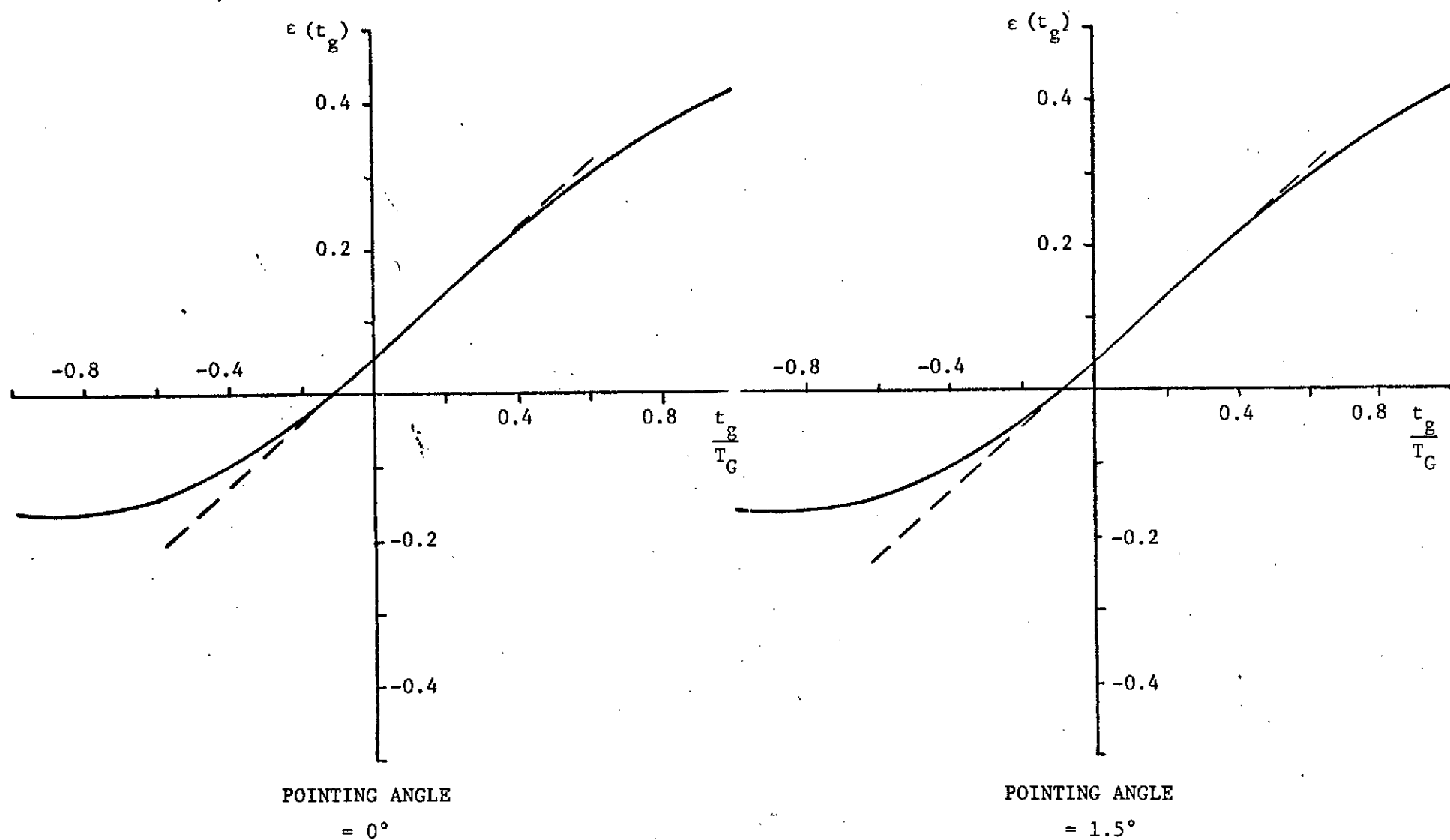


Fig. 4.12 Discriminator Curve for Contiguous Gates and $\sigma_s = 1.0$ m ($H_{1/3} = 13.12$ ft.).

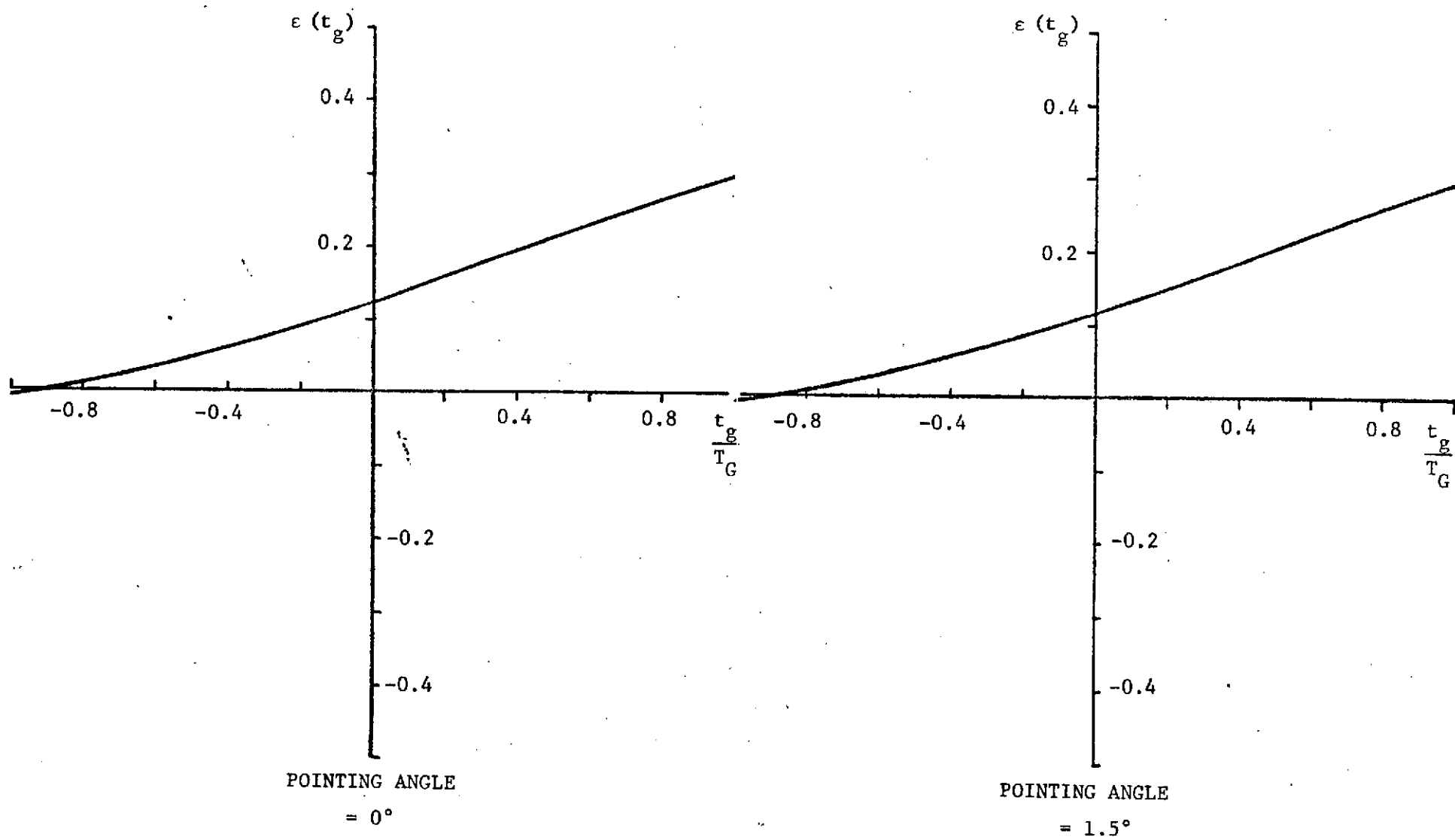


Fig. 4.13 Discriminator Curve for Contiguous Gates and $\sigma_s = 2.5$ m (rms).

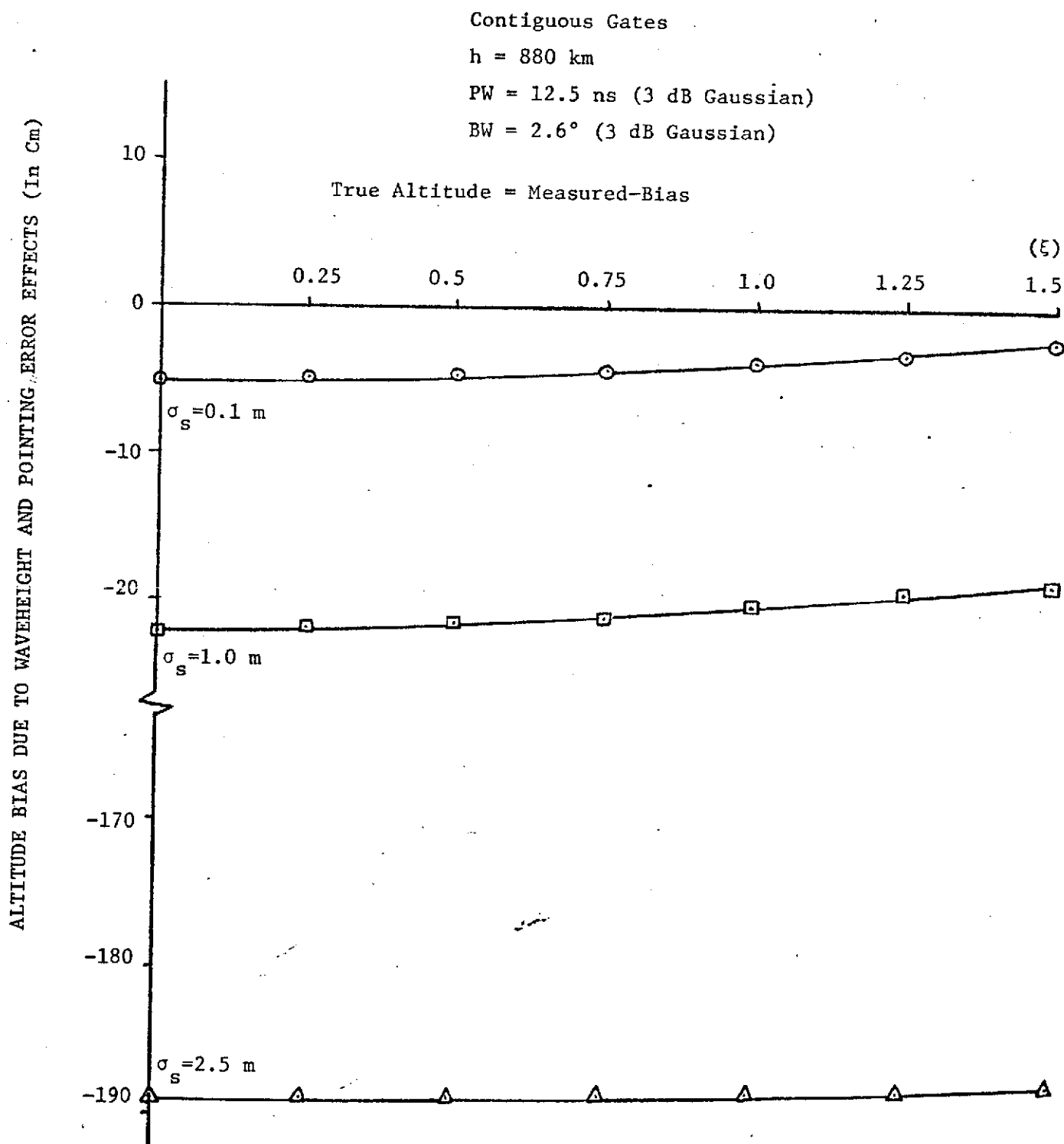


Fig. 4.14 Altitude Bias Errors due to Waveheight and Pointing Error Effects for Contiguous Tracking Gates.

order of a few centimeters for the anticipated range of pointing errors and waveheights. By reducing the gate separation to one gate width, the bias errors may be decreased by about a factor of two for small to moderate waveheights. For large waveheights the bias error resulting from the 12.5 ns gate separation increases significantly. In view of this fact; the optimum tracker in the sense of minimum bias error might well be one in which the gate spacing is variable and dependent upon the waveheight. For the extreme case of contiguous tracking gates, the altitude bias errors are much more sensitive to waveheight than the 12.5 and 50 ns gate separations.

4.2 Pointing Angle Estimation Using the Attitude/Specular Gate

In the process of analyzing Skylab S-193 radar altimeter data, it was determined that the pointing angle of the antenna (relative to nadir) could be accurately inferred from the shape of the trailing edge portion of the mean return. Although the GEOS-C altimeter does not have Sample-and-Hold gates located in the trailing edge of the return (as did Skylab), it does have a 200 ns long integrating gate located in this portion of the return. This particular gate has been termed the "Attitude/Specular" gate; by comparing the time averaged output of this gate with the output from the Plateau gate, it has been proposed that the pointing angle may be determined. The purpose of this section is to investigate how accurately the pointing angle of the antenna can be estimated using this technique.

Figure 4.1 illustrates how the tracking gates are nominally located relative to the idealized return. For both the Intensive and Global Modes, the width of the Attitude/Specular gate is 200 ns and the separation between it and the ramp-gate is 700 ns. For this study we will make the following assumptions:

- (1) tracker jitter, σ_j , is much less than a pulsewidth and can be neglected;
- (2) the tracker gate bias error due to pointing error and sea state effects is small relative to the pulsewidth and may be neglected, i.e., $t_g = 0$;
- (3) the system point target response is Gaussian with a 3 dB pulsewidth equal to 12.5 ns (IM) and 200 ns (GM);
- (4) the nominal altitude is 843 km;
- (5) the antenna half-power beamwidth is 2.6° .

Since we will be dealing with the Plateau and Attitude/Specular energies, the neglect of tracker jitter and bias is certainly justified since these effects cause relatively small changes in the location of these gates.

Let $P_r(\tau)$ be the post-video mean return power which has not been normalized by the AGC gain. Since we are neglecting jitter, the average Plateau gate energy is given by

$$\bar{e}_p = G_{AGC} \int_{T_1 - T_G/2}^{T_1 + T_G/2} P_r(\tau) d\tau \quad (18)$$

when the GEOS-C altimeter is in acquisition and tracking, the gain of the AGC is adjusted so that the average Plateau gate energy is one; thus,

$$G_{AGC} = \left\{ \int_{T_1 - T_G/2}^{T_1 + T_G/2} P_r(\tau) d\tau \right\}^{-1} \quad (19)$$

The average Attitude/Specular gate energy is similarly given by

$$\bar{e}_{a/s} = G_{AGC} \int_{T_2 - T_G/2}^{T_2 - T_G/2 + T_{a/s}} P_r(\tau) d\tau \quad (20)$$

As per GE's proposed method for determining the pointing angle, the quantity of interest is the difference, Δ , between \bar{e}_p and $\bar{e}_{a/s}$, i.e.,

$$\Delta = 1 - \bar{e}_{a/s} \quad (21)$$

For the Global Mode, $T_G = 200$ ns and $T_{a/s} = 200$ ns, so we are integrating over comparable time intervals to form \bar{e}_p and $\bar{e}_{a/s}$ and Δ will be less than or equal to one. For the Intensive Mode, $T_G = 12.5$ ns and $T_{a/s} = 200$ ns, and $\bar{e}_{a/s}$ will

be roughly 16 (200/12.5) greater than \bar{e}_p ; thus $|\Delta| \gg 1$. To make Δ (for both the Global and Intensive modes) less than or equal to one, we define Δ_{IM} as

$$\Delta_{IM} = 1 - \frac{T_G}{T_{a/s}} \bar{e}_{a/s}, \quad (22)$$

then using (20) for the Global mode and (22) for the Intensive mode, we see that Δ and Δ_{IM} will be on the same numerical scale. It should be noted that if $\bar{e}_{a/s}$ is constrained to a certain numerical range, then there must be some scaling in the hardware in switching from Global to Intensive mode since \bar{e}_p is obtained from different gate widths in the two modes.

Using the previously derived expressions for the mean return waveform, results have been obtained for Δ and Δ_{IM} as a function of pointing angle and they are shown in Figure 4.15. It is interesting to note that for both modes of operation, Δ is relatively insensitive to pointing angle. The reason that the Global mode curve is less sensitive to pointing angle than the Intensive mode curve is as follows. For the Intensive mode, the AGC gain* is relatively independent of pointing angle because the mean return waveform does not vary appreciably (over the Plateau gate) with pointing angle. Thus, Δ_{IM} is determined almost completely by the integral* over the Attitude/Specular gate. For the Global mode, the AGC gain* decreases with increasing pointing angle while the integral* over the Attitude/Specular gate increases. Thus, the product* as defined by (20) remains essentially constant.

Since Δ is the difference of the mean values of two statistical quantities, we must know the variance of Δ in order to state how accurately we can actually estimate the pointing angle. There are essentially two error sources involved in our estimation of Δ . The first is due to the noise-like nature of the return signal and this is a random error. Unfortunately, it is extremely difficult to compute $\text{Var}(\Delta)$ because such a computation requires knowledge of the autocorrelation function of the non-stationary return waveform process. The other important error is due to biases in converting \bar{e}_p and $\bar{e}_{a/s}$ to telemetry units and then back to engineering units. In other words, there is an error associated with the A/D and D/A conversion process. As per the system specification [4], this error is estimated to be $\pm 1\%$ of the recorded value. Thus, the bias error for Δ is given by ϵ_b where

*The AGC gain and integrated gate values as referred to here are equivalent to the quantities defined in (19), (18) and (20) normalized by the factor $\exp[+4\sin^2 \xi/\gamma]$, (See Sec. 4.1, equations (10) and (11)).

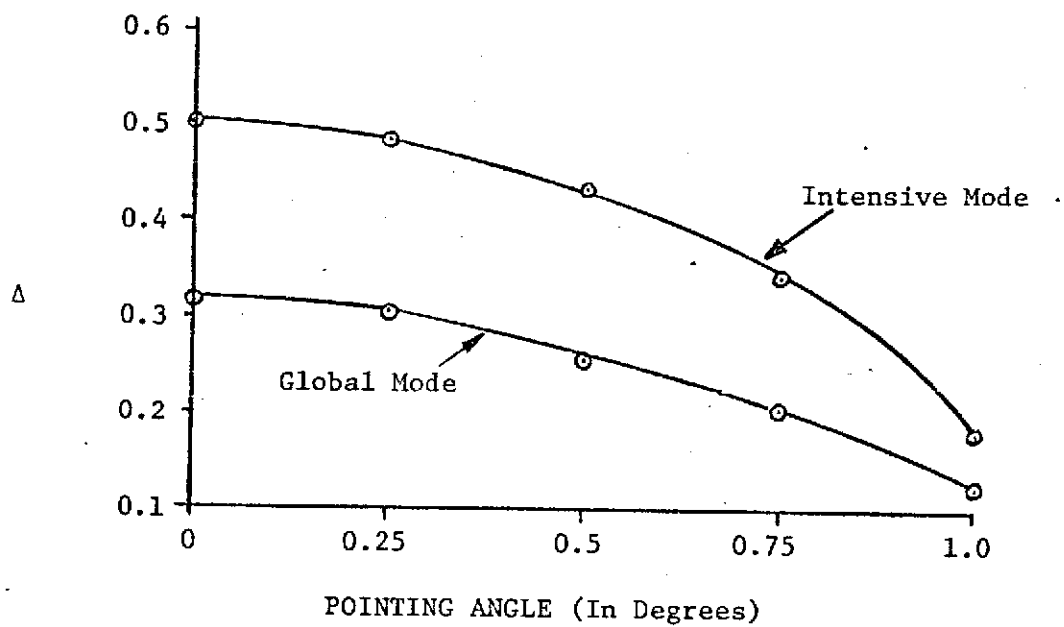


Fig. 4.15 A Plot of the Attitude Estimation Function Versus Pointing Angle for GEOS-C with $h = 843$ km.

$$\epsilon_b = \pm .01 \bar{e}_p - (\pm .01) \bar{e}_{a/s}$$

$$= \pm .01 - (\pm .01)(1-\Delta)$$

The worst case bias error is seen to be

$$\hat{\epsilon}_b = \pm .01 \pm .01(1-\Delta)$$

$$= \pm [.02 - \Delta]$$

A plot of $\Delta \pm \hat{\epsilon}_b$ is shown in Figure 4.16. We note that the basic errors involved in converting \bar{e}_p and $\bar{e}_{a/s}$ to telemetry units and back to engineering units limits the angle estimation process to about 0.5 degrees. Thus, we conclude that the use of an Attitude/Specular gate to estimate pointing angle is no more accurate than about 0.5 degrees. On the other hand, because of the relatively large antenna beamwidth, we question whether a 0.5 degree pointing error will be an important factor.

References

1. Pierson, W. J. and E. Mehr, "The Effects of Wind Waves and Swell on the Ranging Accuracy of a Radar Altimeter," Technical Report, Contract N62306-70-A-0075, New York University, School of Engr. and Science, January 1970.
2. Miller, L. S. and G. S. Hayne, "Characteristics of Ocean-Reflected Short Radar Pulses with Applications to Altimetry and Surface Roughness Determination," in Sea Surface Topography from Space, Vol. 1, ed. by J. R. Apel, NOAA Tech. Rep. ERL 228-AO M. 7, pp. 12-1 to 12-7, May 1972.
3. Miller, L. S., G. S. Brown and G. S. Hayne, "Engineering Studies Related to Geodetic and Oceanographic Remote Sensing Using Short Pulse Techniques, "Final Report (Task B & E), Contract NAS6-2135, Research Triangle Institute, Research Triangle Park, North Carolina, February 1973.
4. _____, "GEOS-C Summary Phase I Technical Report," Contract APL 372085, Vol. I, General Electric Co., Utica, New York, p. 18 (System Performance Specifications), 31 May 1972.

$\Delta \pm \text{PEAK BIAS ERROR } (\hat{\epsilon}_b)$

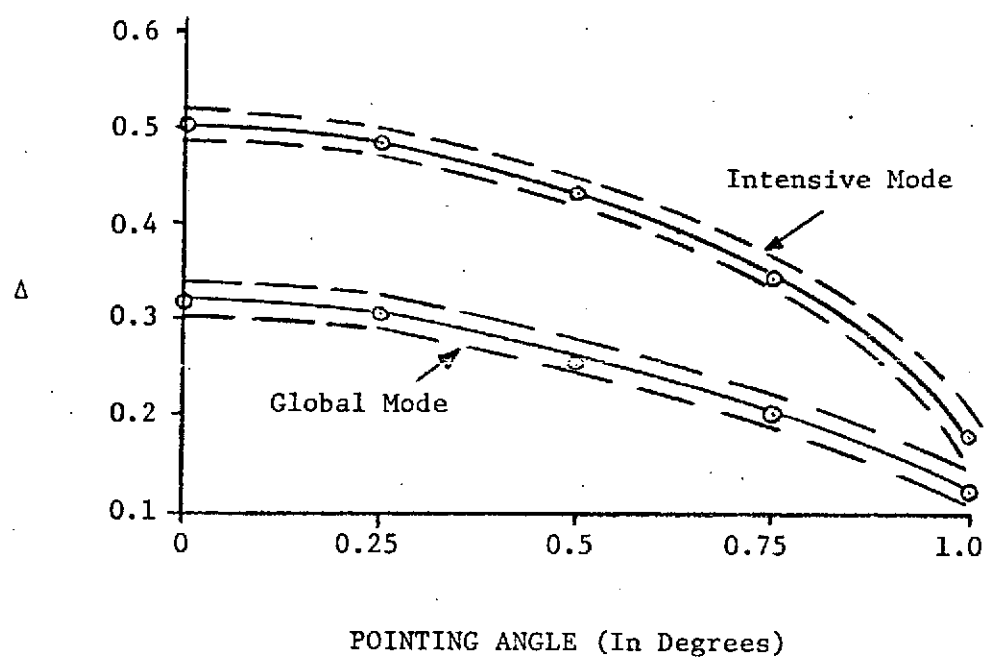


Fig. 4.16 A Plot of the Attitude Estimation Function \pm One Percent Bias Errors for GEOS-C with $h = 843$ km.